DEVELOPMENT OF A DYNAMIC ENVIRONMENTAL TRANSMISSION ELECTRON MICROSCOPE FOR THE STUDY OF LIGHT-INDUCED DYNAMICS IN NANOSCALE MATERIALS

BY

ALLAN EUGENE SYKES

DISSERTATION

Submitted in partial fulfillment of the requirements
for the degree of Doctor of Philosophy in Chemistry
in the Graduate College of the
University of Illinois Urbana-Champaign, 2021

Urbana, Illinois

Doctoral Committee:

Adjunct Assistant Professor Renske van der Veen, Chair
Professor Jian-Min Zuo
Professor Prashant Jain
Associate Professor Josh Vura-Weis

ABSTRACT

In this dissertation we present the development and characterization of a unique dynamic environmental transmission electron microscope (DETEM) which combines ultrafast laser spectroscopy with high-resolution electron microscopy. The novel instrument is capable of capturing snapshots of evolving nanostructures, such as individual nanoparticles, and soft materials undergoing temperature-, gas-, voltage-, or light-induced chemical transformations on time scales ranging from femtoseconds-milliseconds. We demonstrate the successful use of the new instrument by a comprehensive study of the picosecond-resolved dynamics of a three-dimensional electron gas in vacuum subject to a static magnetic field, as well as preliminary single-nanoparticle studies of metal-oxide and metal-organic framework materials that undergo photoinduced phase transitions between structures with different electrical and magnetic properties.

ACKNOWLEDGMENTS

There are many people that deserve my thanks over the course of my studies, both professionally and personally. Thank you to my advisor Renske van der Veen for her mentorship and guidance throughout this journey. I'll always want to do more but I am extremely happy at what we were able to accomplish with the DETEM. I owe many thanks to the various DETEM project members. Dr. Jim Mabon was an invaluable resource and I learned something from him in almost every interaction, it was a pleasure. Omid taught me a lot and I am thankful he was an addition to the DETEM team. Ryan, Eric, Frank, and Oliver all made this possible too and I appreciated their membership and contributions greatly. Thanks to the members, both past and present, of the van der Veen group I enjoyed you all and appreciate the various forms of support you've all provided.

There are so many people from the chemistry department that made this an enjoyable adventure as well. My chemistry friends Larry, Ryan, David, Wade, Patrick, Kori, Coraline, Alexander, and so many more. The IMP office was a source of happiness as well. Overall, the people I was able to interact with in the chemistry department provided support as I went through this adventure.

Importantly, for me, my wife and dog Zuko deserve many thanks in calming and soothing me during the stressful periods of this PhD adventure. My mom, dad, sister, and brother-in-law were also so supportive and it helped give me strength at times. Additionally, my friends back in Oregon provided lots of love and support as well. All these people, and more, helped me through this adventure and thank you to you all.

TABLE OF CONTENTS

CHAPTER 1: TRANSMISSION ELECTRON MICROSCOPY ON ULTRAFAST TIME SCALES 1

CHAPTER 2: DEVELOPMENT OF THE DYNAMIC ENVIRONMENTAL TRANSMISSION ELECTRON MICROSCOPE AT UIUC . 12

CHAPTER 3: TRANSIENT LENSING FROM A PHOTOEMITTED ELECTRON GAS 45

CHAPTER 4: SPIN-STATE SWITICHING IN IRON-COBALT PRUSSIAN BLUE ANALOGUE NANOPARTICLES 63

CHAPTER 5: PHOTOINDUCED PHASE TRANSITIONS IN TRITITANIUM PENTOXIDE NANOPARTICLES 77

CHAPTER 6: CONCLUSIONS AND FUTURE OUTLOOK 97

REFERENCES 99

CHAPTER 1: TRANSMISSION ELECTRON MICROSCOPY ON ULTRAFAST TIME SCALES

1.1 Transmission Electron Microscopy

The transmission electron microscope (TEM) has been an invaluable instrument for scientists and engineers since its invention by Knoll and Ruska in the 1930's with the ability to perform imaging, diffraction, and electron energy-loss spectroscopy experiments all in one instrument[1]. Engineering advances in the way of electron optics, electron detectors, cryogenic methods, and sample holders has greatly bolsters the TEMs experimental capability[2,3,4,5,6,7]. The result of these advances has allowed the TEM to span research areas across chemistry, biology, physics, and metallurgy[8,9,10,11,12,13,14]. For example in the realm of biology and medicine the TEM was utilized to identify coronavirus during the COVID-19 pandemic[15]. The previously mentioned advances in TEM sample holders have allowed the development of *in situ* TEM, spanning research topics ranging from catalysis in gas cells to liquid cell investigations of lithium ion batteries[7,12]. Direct electron detectors have rapidly demonstrated worth in the arenas of cryo-TEM, ptychography, and protein crystallography[16,17,18]. These broad examples across realms of scientific research and TEM capability attest the versatility and power of transmission electron microscopy.

The TEM is a versatile instrument due the multifaceted nature of its three data collection modes: imaging, diffraction, and electron energy-loss spectroscopy illustrated in Fig. 1.1. These modes and the subsequent modalities will be briefly described and the interested

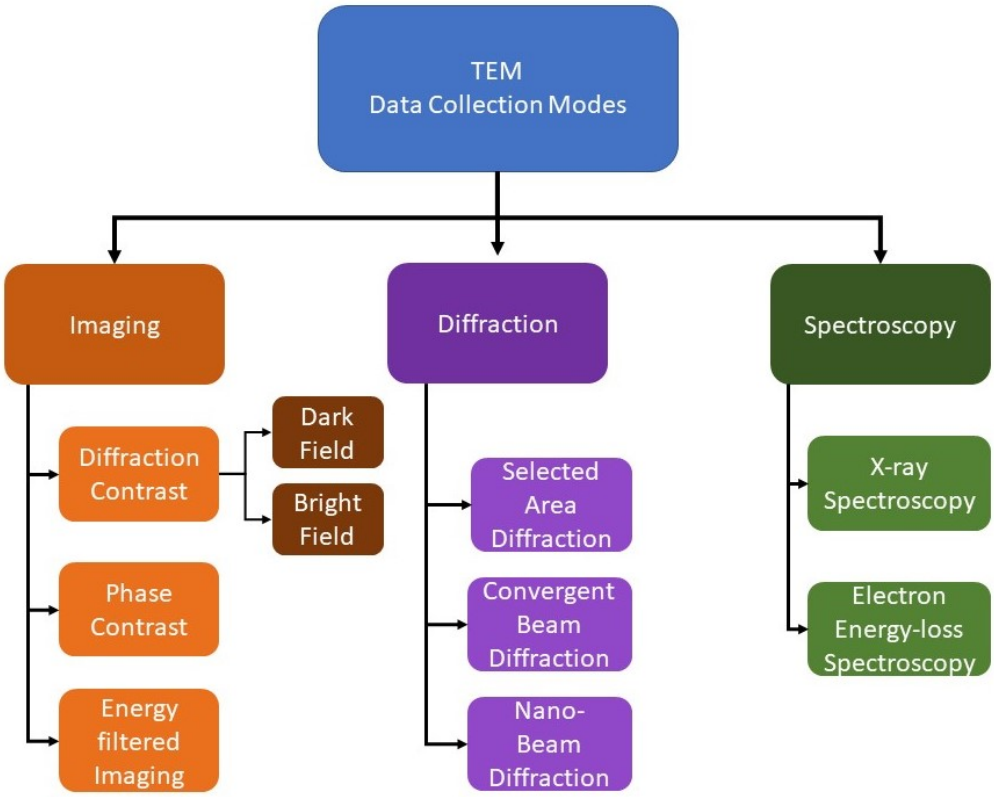

Figure 1.1: Graphical depiction of data collection modes for a transmission electron microscope.

reader is directed to TEM specific textbooks for more detail[19,20,21,22]. Imaging inside a TEM provides a wide range of magnification from one thousand to a million times magnification, with a depth of field and focus that often exceeds optical microscopy capabilities. The three imaging modalities, outlined in orange in Fig. 1.1, take advantage of the electrons wave and particle nature in unique ways to to produce image contrast. The wave-like nature of electrons means that diffraction patterns are produced from crystalline materials, first demonstrated in the Davisson–Germer experiment[23]. Utilizing this fact it is possible to select either diffracted or un-diffracted electrons in the back focal plane of the objective lens to produce dark- or bright-field images as shown in Fig. 1.2 b and a, respectively. For a dark-field image the intensity is a result of collecting only diffracted electrons. As observed in Fig. 1.2 b, the image is formed from electrons that are diffracting from the gold portion of the janus-like particle. Conversely, the image intensity in a bright-field image comes only from undiffracted electrons, meaning crystalline and thick materials will have

low intensity illustrated by Fig. 1.2 a. Phase contrast imaging, also referred to as high resolution imaging, produces images utilizing the constructive and destructive interference due to the probe electrons wave nature, which encodes for instance a crystalline materials lattice structure. Energy filtered imaging utilizes inelastic scatterings that result in the loss of energy in the probe electrons, thus image intensity is a result of electrons in a specified energy range which can be used to map the elemental compostion of a material as shown in Fig. 1.3. Electron energy loss will be discussed below when introducing electron energy-loss spectroscopy.

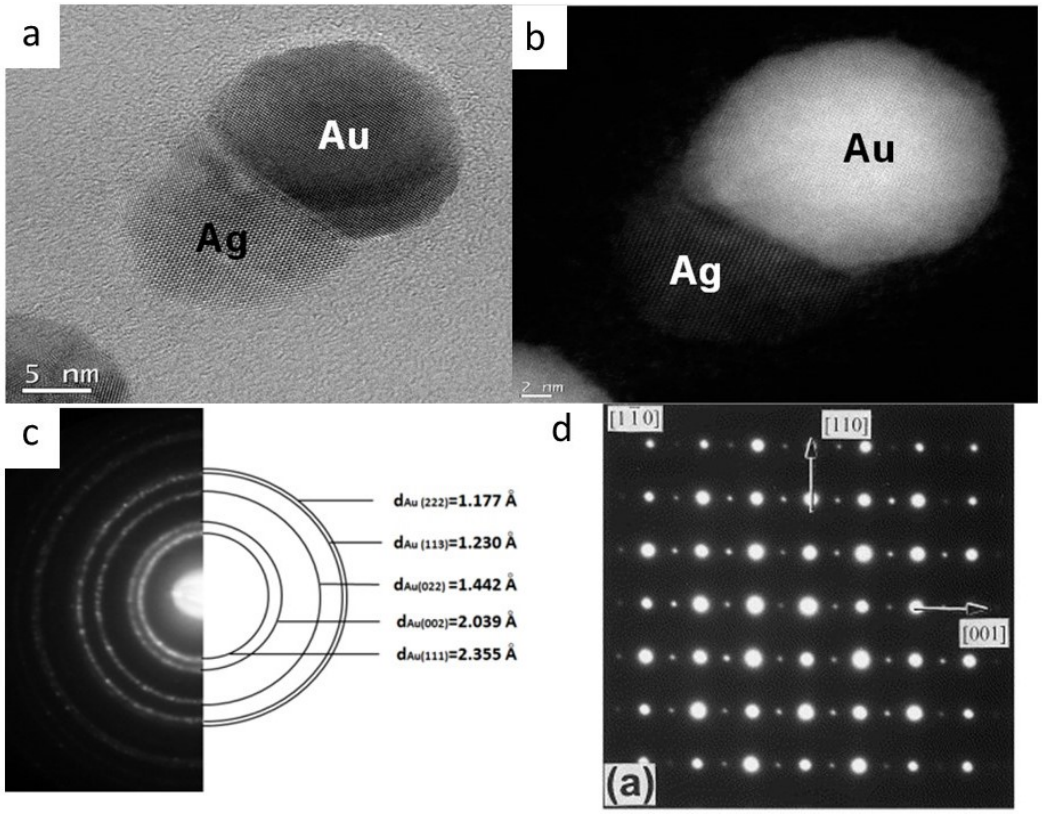

Figure 1.2: a and b) Bright field and dark field images, respectively, of gold and silver Janus-like particles. Images adapted and modified from [24]. c) Selected area diffraction of gold with half the image showing the theoretical labeled diffraction rings, taken from [25]. d) Single crystal diffraction pattern of $SrRuO_3$ thin film of the *Pbnm* space group, the diffraction pattern is reprinted from Materials Science and Engineering: B, Volume 56, J.C. Jiang, W. Tian, X. Pan, Q. Gan, and C.B. Eom,, "Effects of miscut of the SrTiO3 substrate on microstructures of the epitaxial SrRuO3 thin films",Pages 152-157, 1998, with permission from Elsevier.

The diffraction modalities, highlighted in purple in Fig. 1.1, provide crystallographic information of crystalline materials ranging from the global to local scales. Selected area

diffraction works by inserting an aperture into the image plane that selects an area from which a diffraction pattern will be collected. Depending on the selected area aperture size and the particle size this produces diffraction patterns ranging from single crystal to ensemble ring patterns, as illustrated by Fig. 1.2 c and d. The electron beam is fully spread which produces a collimated electron beam impinging upon the sample for a selected area diffraction pattern. This diffraction modality acts as a global diffraction probe of the sample. In contrast, convergent beam diffraction focuses the electron beam to a small spot resulting in a local diffraction probe of the sample. Convergent beam diffraction, however, produces diffraction disks rather than diffraction spots due to the electron beam not being collimated as it impinges on the sample. The information contained within a convergent beam electron diffraction pattern, however, provides structural information contained only in the area of the convergent beam. This diffraction modality is more common in a scanning transmission electron microscope that are designed to produce a quality convergent electron beam that can be scanned across the sample. Nano-beam diffraction utilizes a collimated beam that has a diameter on the nanoscale which provide a local probe of the sample. The combination of these diffraction techniques allows TEM users to well characterize the crystalline structure of a material.

There are two modalities of spectroscopy that can be used inside of an electron microscope, x-ray and electron energy-loss spectroscopy highlighted in green in Fig. 1.1. X-ray spectroscopy measures x-ray emissions that occur after a bound electron has been ejected from an atom in the sample and higher energy bound electron decays to fill this vacancy. The result of this decay is an x-ray with energy equivalent to the difference between energy level of the empty electron orbital and bound electron orbital that fills the vacancy. These x-rays are called characteristic x-rays because the energy difference between electron orbitals is dependent upon the atomic number of the element. In an electron microscope the ejection of these bound electrons is due to inelastic scattering, in which the probe electron looses the necessary amount of energy to eject the bound electron. X-ray spectroscopy in a TEM measures the

aforementioned emitted x-rays, while in contrast electron energy-loss spectroscopy measures the energy loss in the electron probe beam as a result of these inelastic scattering processes. As a practical note, due to detector capabilities, electron energy-loss spectroscopy has much better resolution on the order of one electron volt compared to x-ray spectroscopy which is typically on the order of 100's of electron volts. This results in x-ray spectroscopy being used to conduct elemental mapping for materials in a TEM, but cannot be used to conduct x-ray absorption near edge structure (XANES) or extended x-ray absorption fine structure (EXAFS) analysis. Instead, the analogous analysis is done for the energy loss near edge structure (ELNES) and the extended energy loss fine structure (EXELFS), which are techniques of electron energy-loss spectroscopy. In Fig. 1.3 a, there is an example of an electron energy-loss spectra, which identifies different regions of the spectra as low-loss or core-loss. The core-loss region corresponds to the aforementioned processes of ejecting a bound electron from a material. The ELNES and EXELFS analysis would then be performed on core-loss peak, such as the oxygen K-edge occurring at approximately 532 electron volts in Fig. 1.3 a. The low-loss region were the probe electron interacts and losses energy to the material but does necessary eject a bound electron. An energy filtered image is obtained by then selecting a region in the electron energy-loss spectra where only electrons of that energy form the image, illustrated in Fig. 1.3 b.

The three modes, and subsequent modalities, of data collection covered in brief above are what make this instrument so prolific for investigating materials at the nanoscale. Imaging and diffraction experiments alone provide valuable structural data in the way of particle morphology and crystal structure. The addition of spectroscopy then provides additional chemical composition and electron structure information. It is then possible to almost completely characterize a material at the nanoscale in a TEM. There are however limitations to what can be achieved with a TEM. For instance, an electron is a charged particle that interacts strongly with matter and can impart enough energy to the sample to break bonds causing radiolysis or knock an atom out of place creating a crystal defect[26]. Additionally,

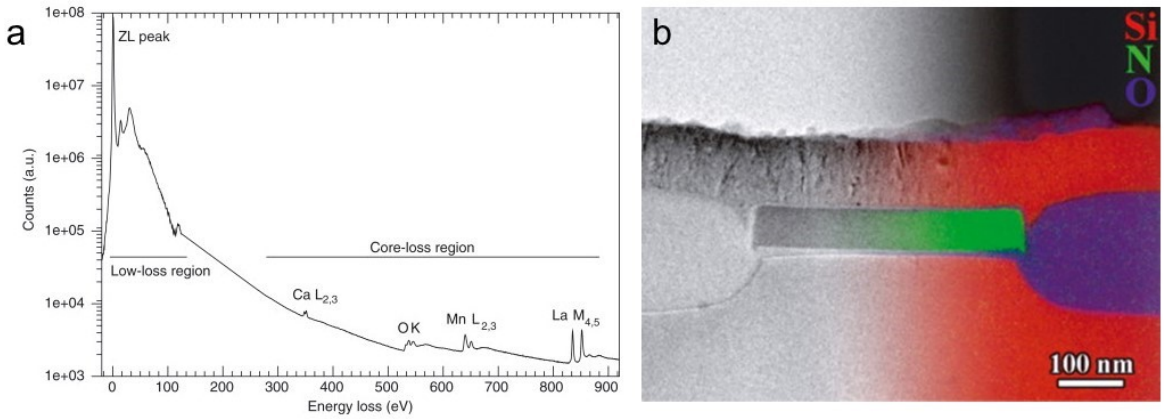

Figure 1.3: a) EEL spectra of LCMO ($La_{0\cdot 85}Ca_{0\cdot 15}MnO_3$) with the zero loss peak, low-loss, and core-loss regions highlighted. b) TEM image and an energy filtered image overlaid to show the ability of energy filtering to identify chemical composition. Reprinted from Encyclopedia of Analytical Science, J.Verbeeck, S.Hens, P.Potapov, and D.Schryvers, Electron Energy Loss Spectrometry, 324-331, 2005, with permission from Elsevier.

there are sample preparations considerations that need to be taken into account, such as sample thickness for a TEM. If a sample is too thick the probe electrons will be absorbed making it impossible to obtain anything other that amplitude contrast images. Also, while electron detector technology has improved significantly, typical temporal resolution is on the order of seconds with fast data collection on the order of a few hundred frames per second. This temporal resolution limitation and how it is overcome will be discussed followed by work done at UIUC to build an ultrafast TEM to study chemical systems.

1.2 The Development of Dynamic and Ultrafast Transmission Electron Microscopy

The above overview provides an introductory sense of how prolific a TEM is across fields of science and engineering. However, as mentioned the conventional temporal resolution of this instrument is on the order of seconds (or ms at best when state-of-the-art detectors are used), rendering the instrument blind to chemical and physical processes occurring at time scales from μs to fs. For instance, the ephemeral dynamics of photoinduced phase transitions occur on ultrafast (fs-ps) timescales[27,28,29,30,31]. The photoinduced phase transition in the

metal oxide material vanadium dioxide, VO_2 occurs on femtosecond time scales rendering the process invisible to conventional TEM. In trititanium pentoxide, Ti_3O_5, the phase transition is observed at femtosecond timescales with dynamics occurring as a result of the photoinduced phase transition out to nanosecond timescales[32]. Prussian blue analogues (PBAs) are chemical systems that have ultrafast dynamics occurring at timescales ranging from femtoseconds to tens of seconds depending on the chemical composition[33,34,35,36,37]. These materials have applications in optical memory and photomagnetism and require research to understand the underlining physics so that technology in these areas can advance. These examples highlight the need to overcome the temporal resolution limitation in a TEM which can provide wealth of data pertaining to the structure of such materials. This temporal resolution limitation can be addressed by utilizing pulsed lasers coupled to a TEM, first demonstrated by Oleg Bostanjoglo at the Technical University of Berlin[38,39,40,41,42,43,44]. The conventional TEM utilizes a thermionic electron source producing a continuous electron beam, analogous to a continuous wave laser such as a common laser pointer. In the case of a continuous probe, temporal resolution is limited by detectors capabilities. This limitation though can be overcome, as first demonstrated by Bostanjoglo, by coupling lasers to a TEM to excite a sample and/or generate electron pulses. The premise of how to utilize lasers coupled to a TEM to increase temporal resolution will be generalized after which real world examples will be provided showing its usefulness.

The premise of using one or more lasers coupled to a TEM to increase the instruments temporal resolution requires accurate and controllable synchronization between sample excitation and sample probing. Controllable synchronization is important because this allows the user to excite, also called pump, the sample and probe at known times after this excitation. The best use for a laser setup coupled to a TEM is to use two laser pulses, one to excite the sample and a second to generate an electron pulse from the electron source called a cathode. Lasers are advantageous because they allow for control and synchronization down to femtosecond timescales. The temporal resolution is then determined by the convolution

of the pump pulse that excites the sample and the electron probe pulse. There are currently two implementations of this generalized data collection scheme which are used to investigate irreversible and reversible processes. A reversible process can be generalized as one that returns to its original state some time after excitation, while an irreversible process is one that transforms into a different state upon excitation and does not return to the ground state within a certain (long) time period (which can be infinite).

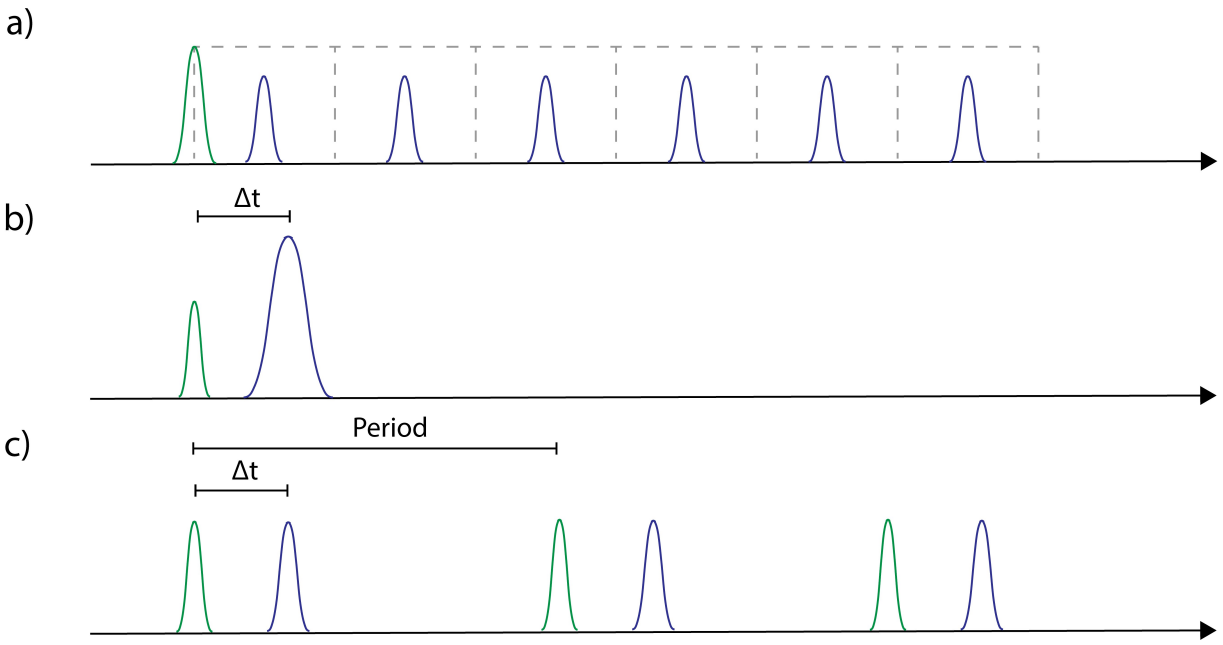

Figure 1.4: Generalized data collection schemes implemented for dynamic and ultrafast TEM instruments. a) The movie mode data collection scheme first implemented with the DTEM at LLNL to probe irreversible dynamics of the sample, in which the sample is excited by a single laser pump pulse depicted in green, then subsequently probed by a train of electron pulses. The dashed gray boxes represent the electron probe pulses being deflected to different locations on the detector by a high speed electrostatic deflector as was first implemented in the DTEM instrument at LLNL. b) The single shot data collection scheme for irreversible dynamics where the sample is excited by a single laser pump pulse and probed by a single electron probe pulse. c) The stroboscopic pump-probe data collection scheme used to investigate reversible processes that return to the original state withing the experimental period used for both the pump and probe pulses.

The Dynamic Transmission Electron Microscope (DTEM) developed at the Lawrence Livermore National Laboratory (LLNL) was built using the groundwork laid out by Bostanjoglo to investigate irreversible processes using nanosecond lasers[45]. This was achieved by using single laser pulse to pump the sample initiating irreversible processes, that were then probed by a series of nanosecond electron probe pulses to collect data, illustrated in Fig. 1.4a.

Using a high speed deflector the electron probe pulses could be directed to different sectors a detector thus allowing nanosecond temporal resolution with respect to the pump pulses[46]. Researchers at LLNL used this instrument to study irreversible phase transitions in titanium films and dynamics in a reactive metal foil[47,48,49]. Not only did the researchers who developed the DTEM at LLNL introduce the movie mode data collection scheme to investigate irreversible dynamics at nanosecond time scales but also demonstrated the usefulness of single shot experiments, Fig. 1.4b, on gold/carbon multilayered foils[50]. Lastly, the pump-probe data collection scheme, Fig. 1.4c, for dark field imaging for demonstrating the ability to study reversible dynamics at nanosecond time scales[51].

Ultrafast TEM (UTEM) was developed by Ahmed Zewail at the California Institute of Technology (Caltech) in parallel to the development of the DTEM at LLNL[52]. Employing his background in ultrafast spectroscopy, Zewail coupled a femtosecond laser to employ the pump-probe data collection scheme[53]. Unlike the DTEM at LLNL, the ultrafast TEMs at Caltech were used to study primarily reversible processes. This is because the number of electrons in a fs pulse is much less than is achievable in a ns pulse due to electron-electron interactions. In brief, these electron-electron interactions place a limitation on the number of electrons in a single pulse before the interaction become deleterious to the temporal, spatial, and energy experimental resolution. One of the most notable discoveries of ultrafast TEM at Caltech was that of a non-linear interaction between the electron probe pulses and the evanescent electric field in the vicinity of nanostructures, dubbed photon-induced near-field electron microscopy (PINEM)[54]. A UTEM was shown to be an advantageous instrument bringing needed temporal resolution to the data collection modes covered above, Fig. 1.1, such as nanodiffraction, convergent beam diffraction, and electron-energy loss spectroscopy[55,56,57,58,59,60,61,62]. An interesting example is the analysis of Kikuchi lines that are present in convergent beam diffraction as a means of analyzing ultrafast structural dynamics effecting strain in a material after photo-excitation[63]. Additionally, some of the first studies chemical systems were conducted investigating the photo-induced spin crossover in individual

$Fe(pyrazine)Pt(CN)_4$ nanoparticles[64].

Since the development of the first UTEM at Caltech, researchers have been building these instruments at many other research facilities[65,66,52,67,68,69]. The combination of (ultra)fast temporal resolution and laser excitation with other *in situ* triggers inside the TEM (*e.g.* heat, liquids, gases, *etc.*), however, is underexplored. This is the focus of the Dynamic Environmental TEM developed at the University of Illinois at Urbana-Champaign (UIUC), as described below.

1.3 Goal of this Dissertation and Outline

The goal of this dissertation work is to develop a unique time-resolved TEM instrument that can be used to study light-induced dynamics in a variety of nanoscale materials and on a broad range of time scales. The system is based on an environmental high-resolution commercial TEM. The unique features of this system compared to others around the world consist of the combination of tunable pulsed light excitation from the UV to the IR, with a large variety of *in situ* conditions such as liquid phases, gas exposure, electrical bias, heating and cooling. Furthermore, the system combines an electron-energy loss spectrometer and image filter with a state-of-the-art and fast direct electron detector, which enables unprecedented sensitivity and temporal resolution for chemically sensitive imaging under reactive conditions. These capabilities enable discoveries in heterogeneous catalysis, polymer physics, electrochemical charge transport, biofunctional interfaces, and ultrafast materials switching, which are critical for, *e.g.*, clean energy generation, biomedical imaging, flexible electronics, and information storage.

In Chapter 2 of this dissertation we describe the development of the dynamic environmental TEM (DETEM) in the Materials Research Laboratory (MRL) at UIUC. In the framework of this dissertation we have used the DETEM for the study of transient lensing dynamics from photoemitted electron clouds (Chapter 3) and photoinduced phase transitions in Prussian blue analogue (Chapter 4) and metal-oxide (Chapter 5) nanoparticles. The emphasis for

the latter lies on the study of individual nanoparticles, rather than nanoparticle ensembles, which enables insights into effects of particle size and surface on the efficiency and time scales of phase propagation after photoexcitation. Such studies of individual nanoparticles are of fundamental interest and have relevance to technological applications of functional miniaturized materials, such as optoelectronics and data storage.

CHAPTER 2 : DEVELOPMENT OF THE DYNAMIC ENVIRONMENTAL TRANSMISSION ELECTRON MICROSCOPE AT UIUC

This chapter outlines the development of the dynamic environmental transmission electron microscope (DETEM) housed in the Materials Research Laboratory at the University of Illinois at Urbana-Champaign (UIUC). This instrument is one of the few ultrafast TEMs based on a Hitachi TEM, and the only ultrafast *environmental* TEM to date. This chapter will first detail the H9500 TEM platform, before we discuss the modifications made to turn the commercial system into an ultrafast microscope. The chapter concludes with the characterization of the new instrument.

2.1 The Hitachi H9500

The DETEM at UIUC was built using a Hitachi H9500 TEM, graphically represented in Fig. 2.1. This electron microscope with a thermionic LaB_6 cathode is capable of operating at accelerating voltages of 80, 100, 200, and 300 kilovolts (kV), depending on experimental requirements. For example, a 80 kV accelerating voltage is common for researchers working with graphene[70,71,72,73], and 200 kV is common for researchers conducting liquid cell experiments[74,75,76,77]. The microscope also provides a wide range of imaging magnifications from 200× to 1.5 million×, providing point-to-point and lattice resolutions of 1.8 and 1 Å, respectively. This instrument has differential pumping apertures and a home-made gas handling system, depicted in Fig. 2.1, allowing for *in situ* experiments at pressures up

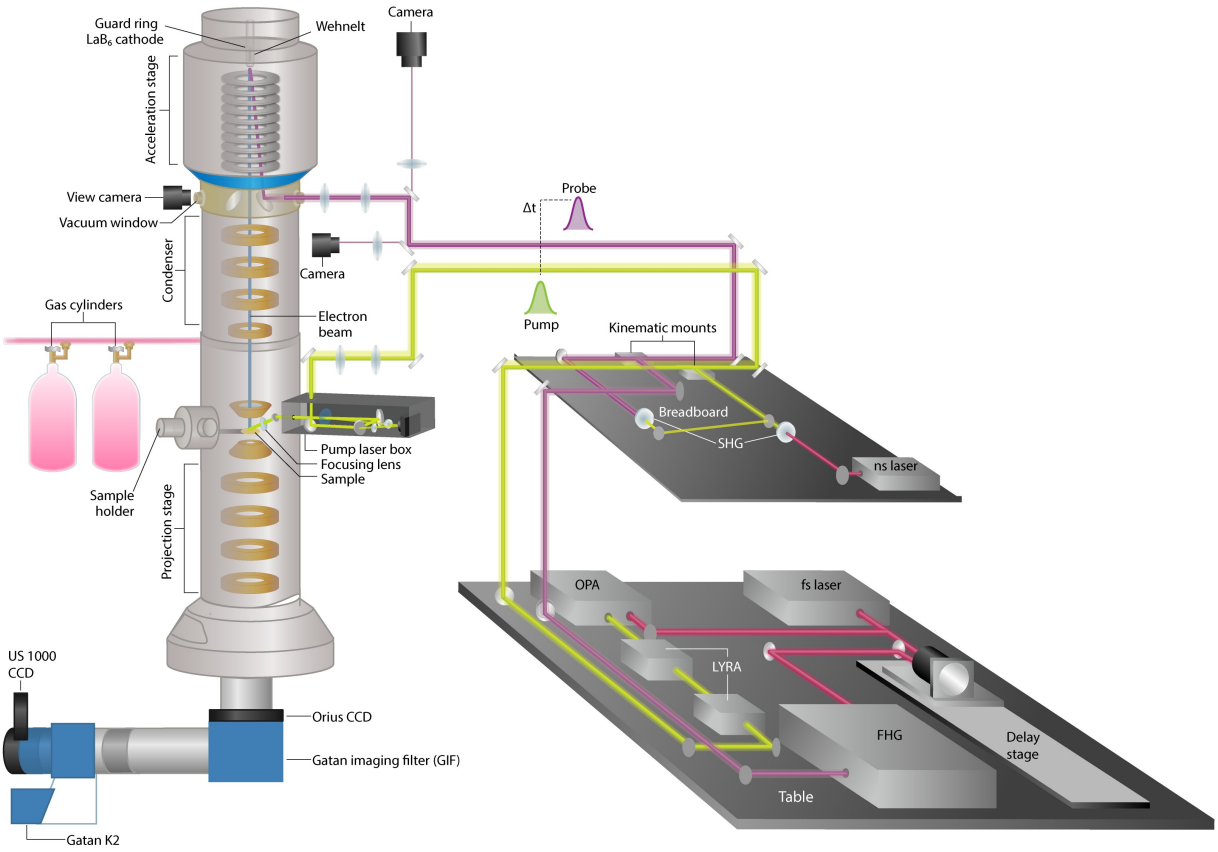

Figure 2.1: Graphical depiction of the DETEM at UIUC. The commercial Hitachi H500 TEM is interfaced with a fs laser and ns laser.

to 10^{-1} Pascals in the specimen area with. Currently, the gas handling system is set up for oxygen, hydrogen, nitrogen, and carbon monoxide with the ability to add other gases with proper calibration. Additionally, a Hitachi MEMS-based heating holder with maximum temperature of approximtely 1200 degrees Celsius, a Hummingbird liquid cell holder, and a Gatan liquid-nitrogen (LN) cooling holder capable of temperature down to approximately -195 degrees Celsius were purchased for the H9500, expanding on the *in situ* capabilities of the instrument. The system has two charge-coupled device (CCD) cameras and one direct-electron complementary metal-oxide semiconductor (CMOS) detector. The Gatan K2 CMOS detector and the UltraScan 1000 CCD are installed at the end of a Gatan imaging filter (GIF) providing the instrument with energy filtered imaging and electron spectroscopy capabilities,

while the Orius CCD detector is positioned before the GIF for low-magnification imaging and diffraction. All these features render this instrument a high-resolution workhorse capable of *in situ* experiments with a range of data collection modalities.

The Gatan K2 Summit/IS direct electron detector that was purchases for the H9500 is a state of the art detector that enables an instrument to operate at low electron dose rates and collect images as fast as 400 frames per second. Direct electron detectors, such as the K2, are highly valuable additions to an electron microscope because of there improved detector quantum efficiency compared CCD detectors. The Summit package purchased for the K2 detector provides the user 3 different modes for collecting data called Linear, Counting, and Super-resolution mode. The linear mode for the K2 collects data in which there is an assumed linear relation between pixel intensity and electron detected on the camera, which is similar to any CCD detector for a TEM. The counting and super-resolution modes are unique in that modes can provide a count of the electrons on the detector. These two modes however require lower electron dose rates so that the counting works and also so that the detector is not damaged. The difference between the counting and super-resolution mode is that it can resolve where an electron landed on the detector with sub-pixel accuracy resulting in very high resolution images. This mode requires the lowest electron dose rate of the three modes to ensure the algorithm implemented by Gatan can resolve single electron pixel locations. The K2 IS package was also purchased which provides users the ability to record movies at 400 frames per second at conventional electron dose rates. The IS mode for the K2 combined with one of the holders mentioned above would provide significant *in situ* capability with a fast 2.5 millisecond temporal resolution for conventional TEM.

2.2 DETEM Modifications

At the heart of the DETEM development is the interfacing of the electron column with various laser systems. This interfacing allows for the generation of electron pulses via the photoelectric effect for which unique data collection schemes for time can be implemented,

illustrated in Fig. 2.2. The photoelectric effect states that there is an specific amount of energy to eject an electron from a material, known as the work function, and any excess energy to the work function will be transferred to the photo-emitted electron. The first data collection scheme presented in Fig. 2.2a is unique to the DETEM due to the K2 detector's ability to operate at 400 Hz with a synchronized ns probe. This scheme is only possible with a ns probe due to the inability to generate a significant amount of electrons in a fs pulse necessary to produce enough signal on the detector. The movie mode scheme, Fig. 2.2b, is a scheme first employed with the DTEM at LLNL where a single pump laser pulse stimulated irreversible processes and a series of nanosecond probe pulses are used to investigate subsequent dynamics[46]. For the DTEM at LLNL the gray dashed lines would represent the high speed electrostatic deflector used to change where the on the detector the electron beam is positioned, while for the DETEM at UIUC this represents the frame rate of the K2 detector. The single shot mode, Fig. 2.2c, utilizes a single pulse for both the pump and probe, where the single pump pulse initiates an irreversible process that is probed by the single probe pulse at a known delay with respect to the pump pulse. The pump/probe scheme, Fig. 2.2d, allows collect data on reversible processes by synchronizing a pump and probe pulses with a known temporal delay. For a TEM experiment this means that for a 10 kHz experimental repetition rate the data collected from a one second exposure would be the accumulation of 10 thousand probe pulse with a known delay with respect to the pump pulse. Without a laser system coupled to a TEM these data collection schemes and the subsequent temporal resolution that comes with using a pulsed electron probe would be impossible.

To transform the H9500 TEM into the DETEM, it was necessary to modify the microscope from its installation settings. As a first step, the TEM and the optical laser table were taken off their respective dampening/spring systems such that they are both steady on the ground. This avoids large relative vibrations between the TEM and the laser, and assures an adequate pointing stability of the laser beams onto the cathode and the sample. In addition, a laser

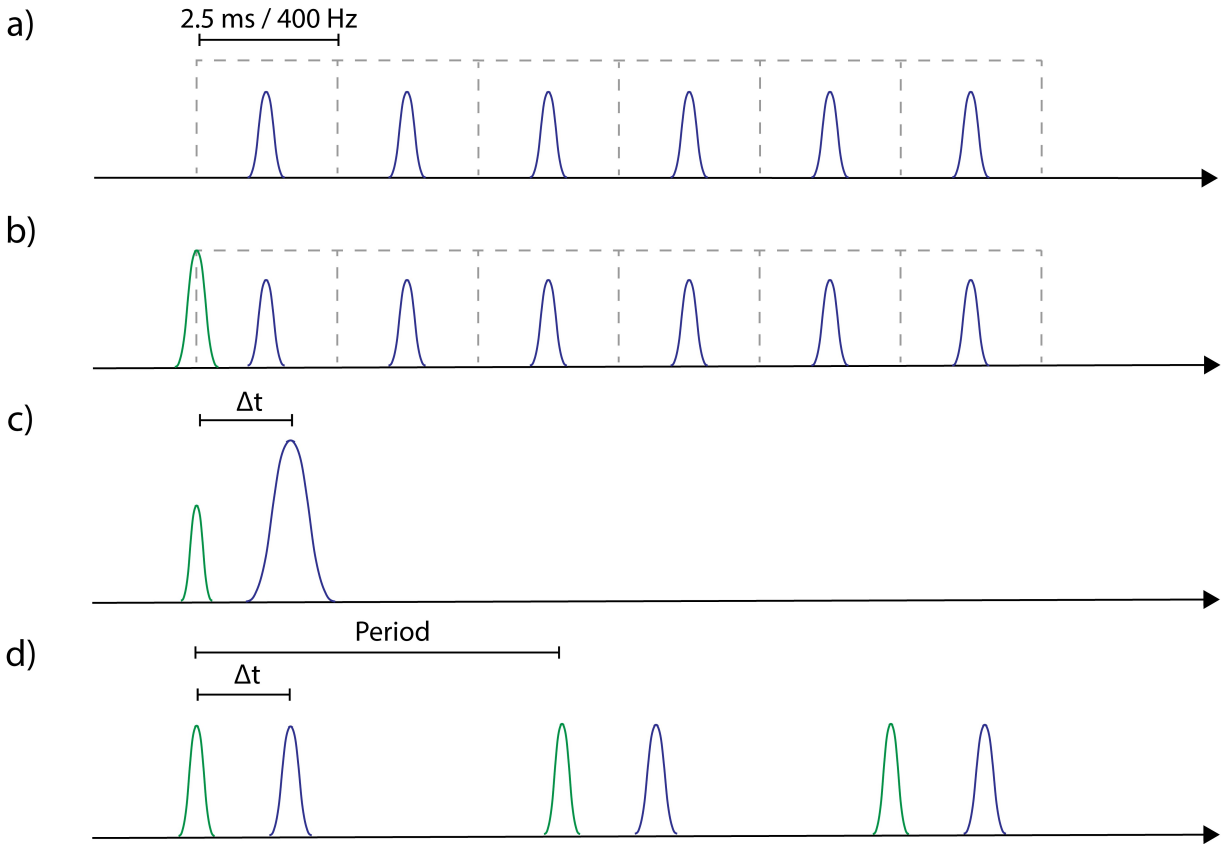

Figure 2.2: Data collection schemes for time-resolved TEM. a) Fast-camera probe with synchronized ns probe pulses. b) Movie-mode TEM. A short laser pulse triggers the dynamics which is probed by deflecting short (ns) pulses of electrons onto different parts of the detector. c) Single-shot mode in which a short pulse triggers the (irreversible) dynamics and an intense short pulse takes a snapshot at a later time. d) Stroboscopic pump-probe mode to study reversible light-induced dynamics. This mode is implemented in the Illinois DETEM in two ways: using fs pump and probe pulses derived from the same laser, and using the fs laser to pump/excite and the ns laser to probe the dynamics.

beam stabilization setup was implemented to correct for small drifts over time, as described in Section 2.2.2. Disengaging the vibrational dampening of the TEM could cause a loss of imaging resolution. We therefore carefully compared the imaging of gold particles before and after modifying the microscope. Fig. 2.3 a-d shows the data with the dampening system *disengaged*; Fig. 2.3 e-h shows the data for the TEM with the dampening spring system *engaged*. Quantitative analysis of the image fast Fourier transform (FFT) reveals no significant change in FFT peak widths, as evidenced by the Gaussian fits of the FFT peaks (Fig. 2.3c and d for engaged vibrational dampening system and Fig. 2.3g and h while

disengaged). The imaging resolution is thus not impacted by the modification.

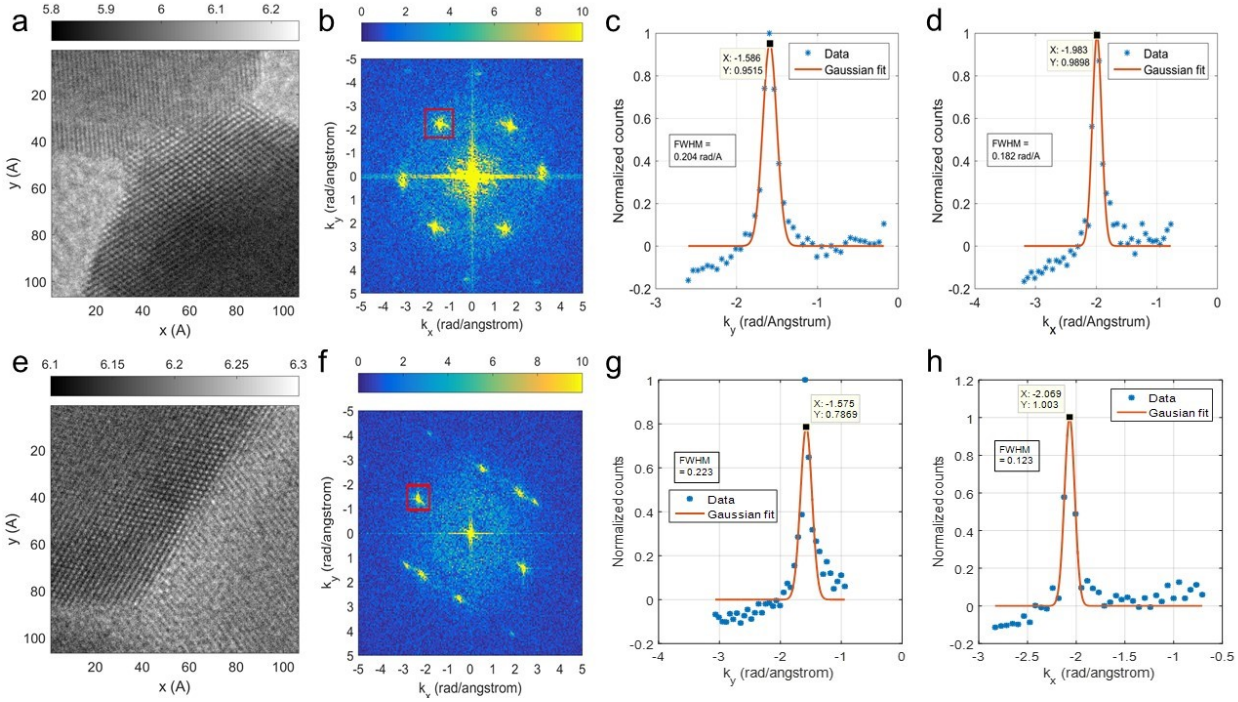

Figure 2.3: Analysis of the effect the vibrational dampening system on high resolution imaging for the system engaged (top row) and disengaged (bottom row). a and e) High resolution images of gold nanoparticles with the TEM vibrational dampening system engaged and disengaged, respectively. For both images, lattice fringes for the gold nanoparticles are clearly visible. b and f) Fast Fourier transforms (FFT) of the high resolution images revealing clear peaks representing the lattice structure in the high resolution images. c and d) Gaussian fits for the peaks highlighted by the red region of interest box where the peak has been summed to be fitted for the x- and y-axes, respectively. g and h) Similar Gaussian fits for the peak in the red region of interest box for the vibration dampening system disengaged. The highlighted peaks were selected in each FFT image due to their similar spacing. The full width at half maximum for the Gaussian fits demonstrate that there is very little difference for imaging with or without the vibrational dampening system engaged.

The second step in the TEM modifications involved the design and implementation of the infrastructure necessary to couple the lasers to the TEM. Here, we distinguish between the pump laser modifications, to guide the laser onto the sample, and the probe laser modifications, to generate short pulses of electrons at the photocathode. These are outlined in more detail in the following, after describing the laser setup and alignment procedures on the optical table. We also emphasize the fact that the modifications conducted to convert the system from a static to a time-resolved/ultrafast TEM are entirely "non-invasive", meaning that no holes need to be drilled in the TEM column. The system could therefore inspire the development of future systems of this kind in small research settings, such as individual

university groups as opposed to national lab facilities.

2.2.1 Laser Setup and Alignment Procedures

The laser setup of for the DETEM consist of a Light Conversion Pharos fs laser in combination with a Light Conversion Orpheus optical parametric amplifier (OPA) and a Bright Solutions Wedge ns laser. The 1030 nm fs laser, capable of operating at repetition rates from single shot to 1 MHz, is housed on a Newport RP Reliance optical table with Newport SLT-3696-OPT legs. The 1060 nm ns laser capable of operating at repetition rates of single shot to 100 kHz is housed on an optical breadboard that is mounted on the optical table at a height of approximately two feet above the table.

The schematic for the fs laser on the optical table is depicted in Fig. 2.4. The 20 W output of the Pharos laser is split with 10% of the power going to the fs probe path and the other 90% into the OPA before being split into the appropriate fs pump path. The fs probe path is directed into an Aerotech PRO165LM one meter long delay line with a Newport Optics UBBR2.5-1S retro reflector mounted on the delay line stage with a Thorlabs model HR1015-AG rooftop mirror to achieve a second pass through the delay line. This enables relative pump/probe delays of up to approximately 13 nanoseconds. The fs probe path is then focused into the enclosed fourth harmonic generation (4HG) apparatus consisting of two beta barium borate (BBO) crystals cut specifically for second harmonic generation (2HG) of 1030 nm and 515 nm light, respectively. In this manner 257 nm light is generated and can be attenuated by a custom half-wave plate and polarizer combination from Eksma Optics directly after the 4HG apparatus. The attenuated fs probe is then directed up to the optical breadboard with a periscope. The fs pump path is directed into the Orpheus OPA with Lyra harmonic separator attachments providing pump wavelengths from 260 to 2600 nm. However, the fs pump path is designed to cover the wavelength range 260 to 750 nm. The visible (400-750 nm) fs pump path is routed with mirrors M9 through M13 and the UV (260-400 nm) pump path is routed mirrors M9 and M14-15. The optics for M9 are swapped

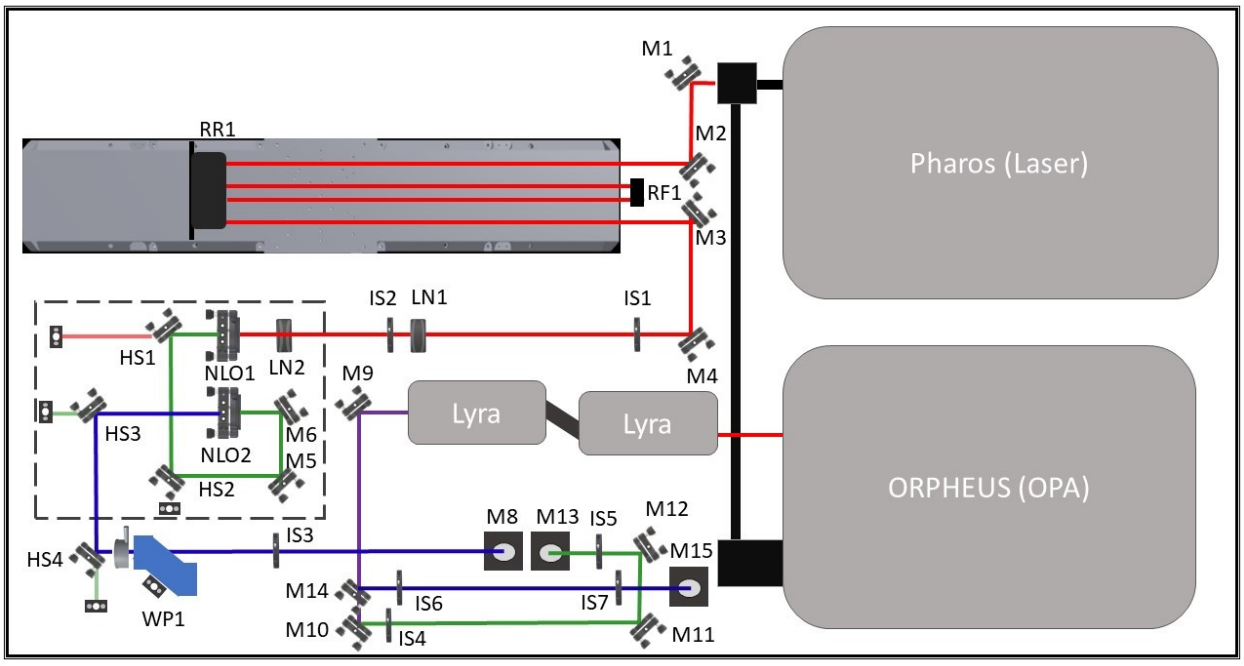

Figure 2.4: Schematic drawing of the fs laser layout on the optical table. The 1030 nm output of the Pharos laser is split with 10% going to the probe path that is aligned into an optical delay stage that it passed through twice. The probe beam undergoes fourth harmonic generation (4HG) to produce a 257 nm beam before being directed to the optical breadboard via a periscope. The remaining 90% of the Pharos output is directed to the Orpheus OPA, which has an output range of 260 to 2600 nm. UV and visible pump paths were built to accommodate 260-400 nm and 400-750 nm light in purple and green, respectively, before being directed via periscopes to the optical breadboard mounted above the optical table.

depending on the pump wavelength chosen for the experiment.

Alignment procedures - fs laser beam

Alignment procedures are conducted for the fs laser only after the laser has been allowed to run for 30 minutes ensuring laser output and optics have stabilized. The alignment of the fs probe path is the most critical because of the optical delay line and 4HG apparatus. First, the fs probe path is aligned into the retroreflector using a removable iris mounted on the right side of the retroreflector. The stage is then moved closest to the M2 mirror and the laser is aligned to the iris using M1, see Fig. 2.4 for mirror assignments. The stage is then moved away from M2, and aligned to the iris using M2. Iteration of this processes is done until the probe laser path remains aligned to the iris at all points of the delay line which produces a path that is collinear to the axis of the delay line. The retroreflector

and rooftop optics produce a collinear output and input path by design. Adjustment of the rooftop mirror is rare, but it may become necessary to adjust the y-axis of the rooftop mirror to ensure the input beam is orthogonal to the dihedral line of the optic. Next, the fs probe is aligned to several irises between the optical delay line and the 4HG apparatus labeled IS1 and IS2 with mirrors M3 and M4, respectively. The fs probe laser is then focused into the series of BBO crystals. 515 nm light is generated from the first BBO crystal and the remaining 1030 nm light is filtered out with two harmonic separators before the next BBO crystal that generates 257 nm light from the 515 nm light. Two additional harmonic separators filter out the remaining 515 nm light before the laser is passed through a half wave plate and polarizer combination for attenuation. The last iris in the fs probe path, IS3, was placed after the fs probe path had been aligned into the periscope directing the path onto the optical breadboard.

Alignment of the pump path depends on the choice of pump wavelength for the experiment. First, the user must configure the Lyra output based on the diagram provided by the Light Conversions TOPAS software that controls the OPA. The M9 optics must be switched either to the visible or UV optics depending experimental needs. There are two outputs, each with two possible beam heights. The M9 mirror must thus be moved and adjusted as necessary. Once the M9 mirror has been adjusted to the Lyra output the user will use either the M9 and M10 mirrors with the IS4 and IS5 irises to align the fs visible pump path, or M9 and M14 mirrors with the IS6 and IS7 irises to align the fs UV pump path into the respective periscope mirrors to be directed to the optical breadboard.

Optical breadboard setup

The laser optics on the optical breadboard are schematically depicted in Fig. 2.5. First, the fs pump and probe paths are directed to the optical breadboard via periscopes with the top periscope mirrors depicted by M1,M11, and M5 for the fs probe, fs visible pump, and fs UV pumps, respectively. The fs probe beam is directed from M1 to the periscope

mirror M4, which elevates the beam to 6 feet above the ground, and is transmitted via safety tubes to the probe insert assembly on the TEM. The fs UV pump path is directed into periscope mirror M15 with mirrors M5-M10 and the fs visible pump path is directed into periscope mirror M15 with mirrors M11-M14. The pump beam is then directed into the pump insert assembly via safety tubes connecting the laser table with the TEM. Three removable kinematic magnetic mounts are used for mirrors M3, M10, and M12 depending on the optical requirements of the experiment. The removal of M3 opens the probe path to the ns probe laser. The removal of both M12 and M10 opens the pump path to the ns pump beam. The removal of the M10 with the M12 mirror in place opens the pump path to the fs visible pump path, and M10 is necessary for the fs UV pump to be directed to the pump path.

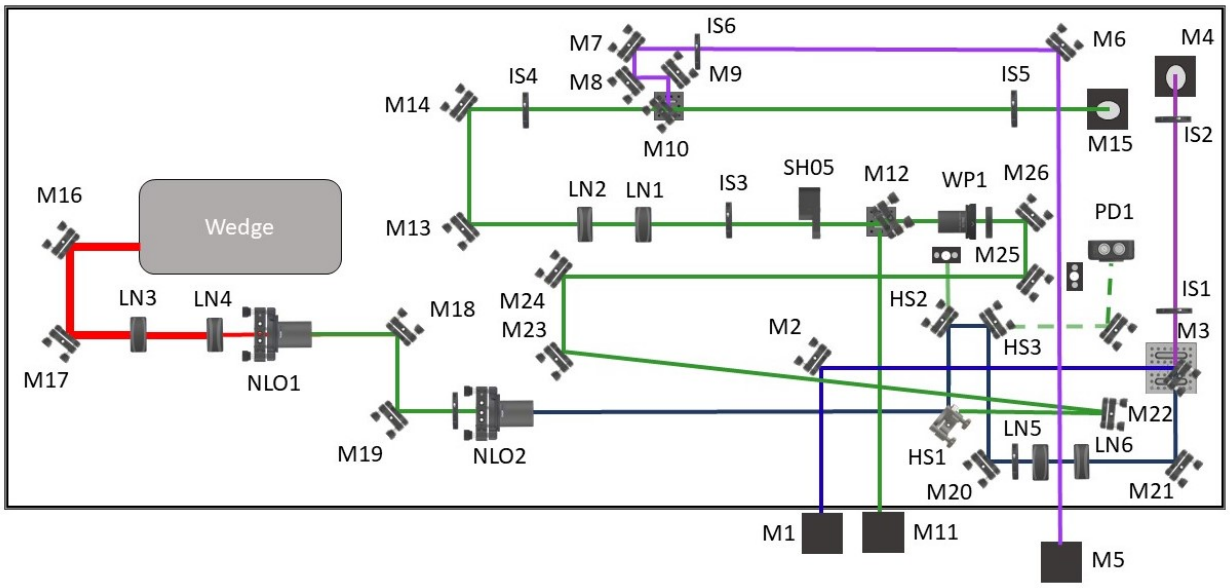

Figure 2.5: Drawing of the optical breadboard mounted above the optical table. The 1064 nm output of the Bright Solutions Wedge ns laser first undergoes fourth harmonic generation (4HG) to acquire 266 nm light to be directed into the probe path. The 532 nm light that passes through the first harmonic separator (HS1) after the BBO crystal (NLO2) is directed into the pump path for the instrument with M12 and M10 mirrors removed. The fs probe, fs visible pump, and fs UV pump paths are directed onto the optical breadboard via top periscope mirrors labeled M1, M11, and M5, respectively. M4 and M15 are the probe and pump periscope mirrors that elevate the beams to 6 feet above the ground and transmit the paths to the probe and pump insert assemblies at the TEM, respectively.

The 6 W output from the ns laser is directed into a 4HG setup consisting of a lithium triborate (LBO) crystal to generate 532 nm light from the Wedge fundamental wavelength

and a BBO crystal to generate 266 nm light from the 532 nm beam. These crystals are labeled NLO1 and NLO2 in Fig. 2.4, respectively. The 266 nm beam generated from the BBO crystal is directed to periscope mirror M4 with three harmonic separators (HS1-HS3) and two UV mirrors (M20 and M21). There is a 2× telescope to reduce the ns probe beam size before being sent to the probe insert assembly via the periscope depicted by M4. The unconverted 532 nm light passing through HS1 is directed to periscope mirror M15 by M22-M26 and M13 and M14. The ns pump can be attenuated using a rotatable half wave plate and fixed polarizer combination just before M12.

Alignment procedures - ns laser beam

Alignment for the optical breadboard depicted in Fig. 2.5 is broken down into the pump and probe path. The fs probe path is aligned through irises IS1 and IS2 using mirrors M1 and M3. The ns probe beam is aligned through the same irises using M20 and M21 with M3 removed from the kinematic magnetic mount. Initial alignment for M16 and M17 for the ns pump path was conducted without any optics after M17 and was carried out through irises IS4 and IS5. The 6× telescope (LN3 and LN4) to shrink the beam was aligned through same irises used for M16 and M17 before placing the LBO crystal (NLO1) in the ns path. Likewise, the M18 and M19 mirrors were aligned in the absence of the BBO crystal (NLO2) again using mounts that were equivalent to the heights of IS4 and IS5, after which the BBO crystal was placed and aligned. Alignment for HS1 to HS3 was coarsely carried out with actual alignment through irises IS1 and IS2 done by M20 and M21. Alignment of the unconverted 532 nm light for the pump path is conducted by M24 and M26 through IS4 and IS5, respectively. The 2× telescope, LN1 and LN2, is removed when the ns pump is used. The fs visible pump is aligned through irises IS4 and IS5 using mirrors M11 and M12. The M13 and M14 mirrors should not be adjusted in order to maintain best alignment for both the fs visible and ns pumps. The fs UV pump is aligned through irises IS6 and IS5 using mirror M5 and M6 to the M15 periscope mirror.

2.2.2 Pump Laser Insert and Alignment Procedures

The pump laser beam is guided onto the sample using a pre-existing port in the TEM that can be used for energy-dispersive X-ray (EDX) spectroscopy. The use of this port implies that no holes needed to be drilled in the TEM and it allows us to get particularly close to the sample and achieve small laser spot sizes. The pump laser insert that goes inside the EDX port was designed and built by Dr. Hyuk Park. An Inventor schematic of the pump insert with the pump path in green is shown in Fig. 2.6a. It includes two 5 mm square prism mirrors (Thorlabs product MRA05-G01) and a $f = 15$ mm convex focusing lens (Thorlabs product LA1222-A) just before the sample. A lead-lined pump insert box (Fig. 2.6 b), designed and constructed by Dr. Omid Zandi, is attached to the pump insert in order to receive the pump path from the optical table and align the laser into the insert (Fig. 2.6 c). The pump insert box also houses a CMOS camera that is connected with a LabVIEW program to stabilize the pump laser beam onto the sample position using piezoelectric motorized mirrors. The geometry of the EDX port results in an elliptical profile for the pump laser on the sample at it impinges at a 22 degrees angle from the samples surface, visualized in Fig. 2.6d. The major axis of the elliptical profile aligns to the y-axis of the sample stage.

The alignment of the pump insert box will be covered here in brief. In order to ensure best possible alignment of the complete pump insert assembly, a pre-alignment is conducted before insertion into the EDX port. This pre-alignment is necessary because the 5 mm focusing lens and 5 mm prism mirrors in the pump insert do not allow for large movements without resulting in clipping on these optics, which is hard to assess once the insert is inside the TEM. The pump insert assembly is secured into a mock construction of the H9500 pole piece and an alignment plate is attached to the end of the pump insert representing the sample plane, Fig. 2.7a and b, respectively. The attached alignment plate has a 1.5 mm hole representing the center of the TEM sample grid. The sides and top of the box can be removed with the top motorized periscope mirror for the box attached to an optical mount holding the mirrors relative position with respect to the remaining optics in the pump insert

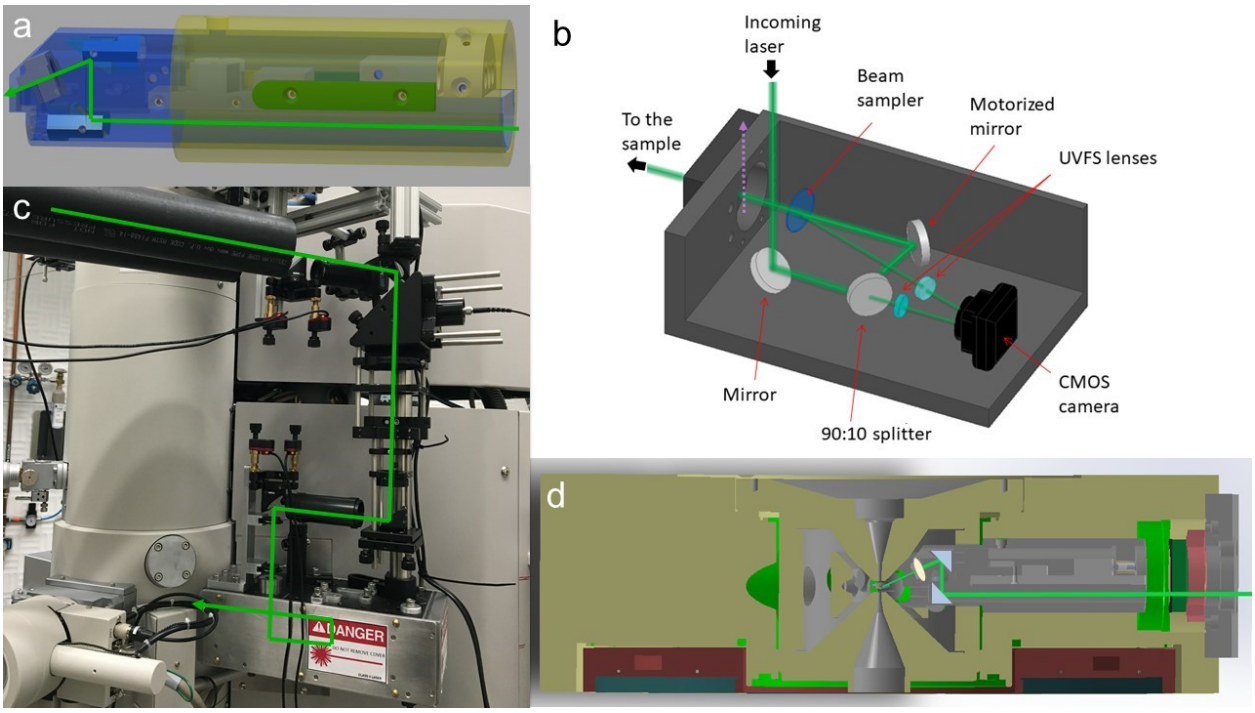

Figure 2.6: a) Inventor schematic of the pump insert to couple the pump laser to the sample through the EDX port. b) The pump assembly optics box attached to the pump insert, housing the optics directing the pump laser path into the TEM onto the sample. c) Picture of the pump insert assembly with the pump path highlighted in green. d) Cross section of the H9500 pole piece with the pump insert in the EDX port; laser beam highlighted in green. The beam impinges with an angle of 22 degrees onto the sample.

box. This top periscope mirror is seen in Fig. 2.6c and Fig. 2.7a, as the mount with piezo electric motors before the two irises above the entrance to the pump box. This motorized mirror and the first mirror in the pump insert box, labeled 'Mirror' in Fig. 2.6b, are aligned so that 10% of the transmitted beam from the 90:10 splitter is observed on the CMOS camera. The 90:10 splitter and motorized mirror are then used to align the pump path down the attached pump insert (Fig. 2.6a) to the attached alignment plate at the end of the insert (Fig. 2.7b). Once a sufficient alignment is obtained, the beam sampler (Fig. 2.6b) is aligned to the CMOS camera. The box is then completely reassembled and safe zones are determined using the LabVIEW beam stabilization code written by Dr. Zandi, to be described below. The safety zones are determined by moving the beam with the motorized mirrors until clipping is observed in the output of the pump assembly, as described in Mr Cornelius' thesis[78].

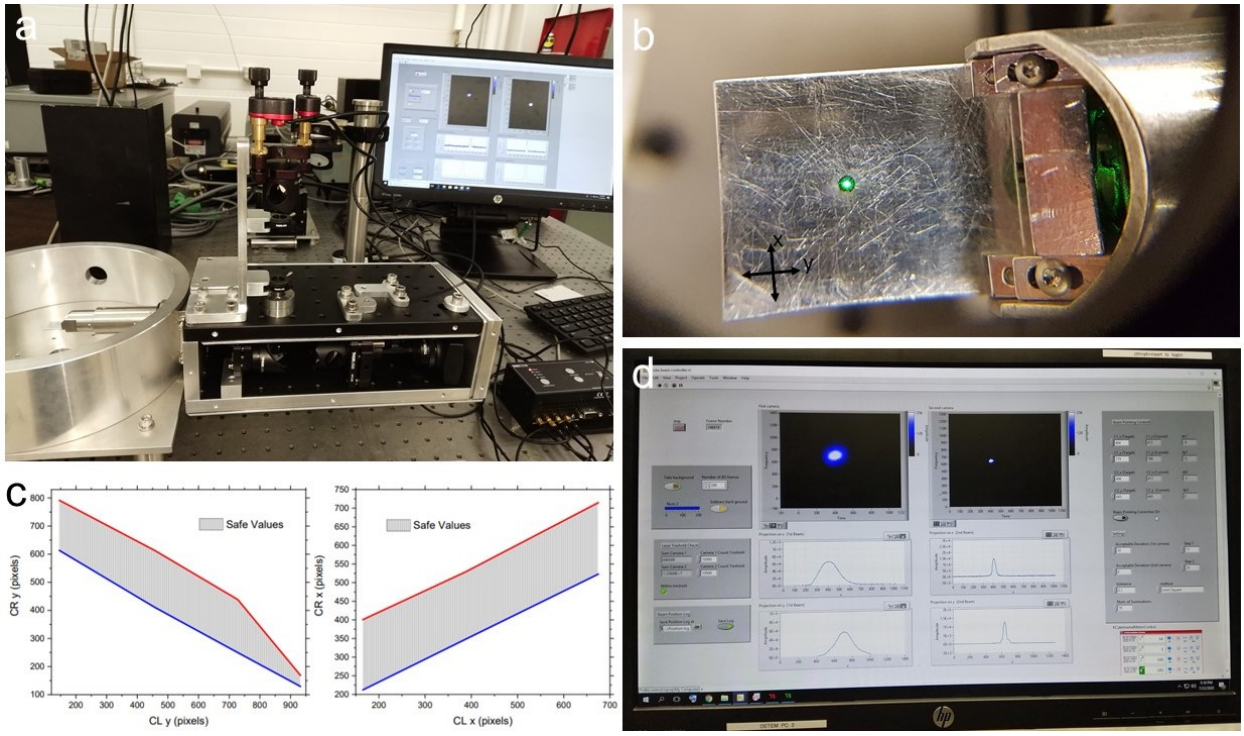

Figure 2.7: a) Picture of the pre-alignment setup for the pump insert assembly. b) Pump laser visualized on the alignment plate attached to the end of the pump insert. c) Safe zones for the pump insert assembly which is observed for the pump beam going through the alignment plate (courtesy of Ryan Cornelius). d) Picture of the beam pointing stabilization program in LabVIEW (coutesy of Omid Zandi).

Here, the pump laser feedback program will be described, as both the pump and probe LabVIEW stabilization programs utilize the same algorithm. This program allows for easily regaining pump and probe alignment at the beginning of an experiment and also accurately maintains alignment during the course of the experiment. The program works by first summing the camera input along the x- and y-axes creating column and row vectors, respectively, that are then fitted to a one dimensional Gaussian which provides the center position for the laser beam on the camera. The program will then compare the fitted peak position centers to the desired peak position within acceptable pixel deviations provided by the user. The LabVIEW program then commands the appropriate motorized mirror axis to correct the beam position to within the pixel deviations provided. The program will then iterate this process for subsequent axes until all position are within the provided pixel deviations.

The interface for the LabVIEW program is shown in Fig. 2.7d. In the middle of the program are the left and right cameras that are continuously updated from the CMOS camera. The summation vectors for the x- and y-axes are then plotted below the images, respectively. On the left hand side of the program is the stop button for the program and dialog interfaces for background correction, intensity thresholds, and saving the output. The background dialog allows the user to take a background of a specified number of camera frames and then subtract the background from all subsequent images before processing and fitting is done. Below is the dialog for intensity thresholds under which the program shut down until the user restarts the program. The intensity thresholds ensure the program is fitting a signal rather than noise. The bottom dialog on the left hand side allows the user to decide to save the program output, which consists of fitted peak center values as a function of time. On the right hand side is the beam control interface and the LabVIEW application interface (API) for the Thorlabs piezo-electric motors on the motorized mounts. The beam control dialog is where the user enables and disables the program as well as defines the peak position centers for the two cameras. Additionally, in this interface the user defines the acceptable deviations for the peak centers, the step size for each piezoelectric motor, and how many frames are summed before each fitting. Below this dialog is the API for the program that controls the Thorlabs piezo-electric motors.

2.2.3 Probe Laser Insert and Alignment Procedures

The UV probe beam was guided onto the LaB_6 (Kimball Physics, 50 μm) cathode by adding a 3-inch piece of column between the gun and the main TEM column in a free drift area. We call this piece of column the "probe laser insert" (Fig. 2.8e), which was designed and manufactured by Dr. Hyuk Park. To accommodate the increased length of the TEM and continue support the gun, a 3-inch aluminum block was installed underneath the gun lift at the back of the column. Two 1-inch diameter window ports with 10 mm silver prism mirrors (Thorlabs product MRA10-F01) with a custom indium-tin oxide (ITO) coating are part of

the probe laser insert, one of which is used as for the UV probe beam and the other as a viewport for the cathode, pictorially presented in Fig. 2.8a and b, respectively. The 10 mm silver prism mirrors require the ITO coating to prevent charge which negatively effects the electron probe path. The viewport provides the ability to image the Wehnelt and cathode tip onto a CMOS camera with $f = 35$ cm convex lens (Fig. 2.8c). This assists with alignment as it provides a means of visualizing fluorescence from the cathode when the UV beam hits the graphite surrounding the LaB_6 tip, which is visualized in Fig. 2.8f and g for the UV probe laser off and on, respectively. A schematic of the UV probe laser beam path is shown in Fig. 2.8d. Before coupling into the TEM, the UV beam size is reduced by a factor of two by a periscope, as shown schematically in Fig. 2.8d and as a photo in Fig. 2.8a. The two mirrors depicted in this schematic are back polished mirrors allowing remaining unfiltered lower harmonics from the 4HG to be transmitted to CMOS cameras to be used for the probe stabilization LabVIEW program. The second CMOS camera is not shown as it is mounted at a similar distance as the cathode acting as a virtual cathode.

Instead of using a conventional LaB_6 cathode, we installed a so-called guarded-ring cathode with a LaB_6 tip that is encased in a carbon ferule with a carbon based glue (Kimball Physics, 50 μm), Fig. 2.8c. The LaB_6 cathode is the pink center of the confocal microscope image in Fig. 2.8c. This type of cathode has been shown to improve the properties of the photoelectron pulses by eliminating electrons emitted from the shank of the LaB_6 crystal[79,80,81]. In particular, the use of a flat tip and the elimination of shank emission significantly improve the temporal resolution, since all electrons are emitted from the same plane (as opposed to different planes in the case of shank emission). This elimination results in an order of magnitude reduction in electron yield when compared to photo-emission from a conventional or truncated LaB_6 cathode. However, coherence of the pulsed electron beam increases resulting in improved spatial resolution for imaging and the energy distribution decreased for the electron pulse improving energy resolution[79,81]. It has recently been shown that tuning the UV wavelength to the exact work function of the LaB_6 cathode a full width

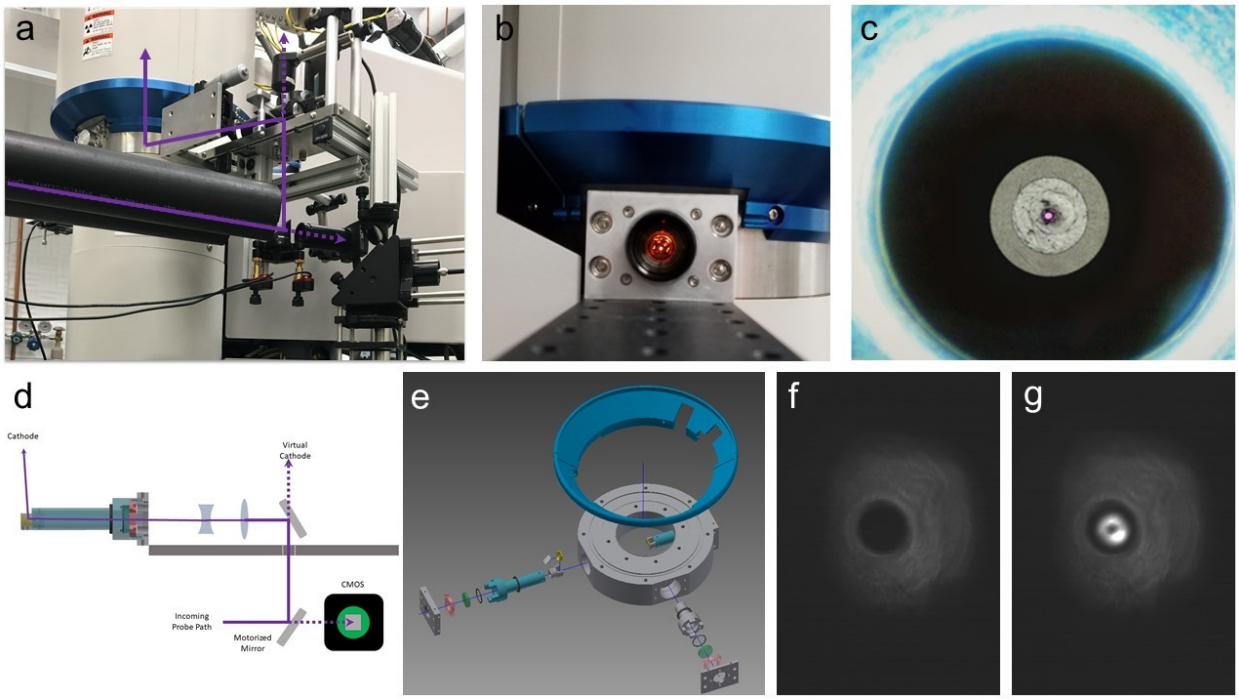

Figure 2.8: a) Picture of the probe insert assembly with the UV probe path (in purple) towards the guarded ring LaB_6 cathode. The dashed lines depict residual lower harmonic that is transmitted through back polished mirrors onto CMOS cameras used by the probe beam pointing stabilization LabVIEW program. b) Picture into the viewport opposite of the probe insert port showing the orange glow of a hot guarded ring LaB_6 cathode in thermionic mode. c) Optical microscope image of a Kimball Physics guarded-ring LaB_6 cathode in the Wehnelt assembly (light ring close to the picture rim). d) Schematic of the probe insert assembly depicting the UV path on the last two back-polished mirrors in the path before the beam is shrunk by a factor of 2 by a telescope. e) Inventor schematic of the probe laser insert modification with an exploded view of the ports and optics. f and g) Viewport images with diffuse white light illumination of the guarded-ring LaB_6 cathode with and without the UV probe on, respectively.

half maximum for the zero loss peak from the electron energy loss spectrum can be reduce to 0.45 electron volts[81]. Importantly, guarded ring cathodes can also be used in conventional thermionic emission mode of the TEM, without compromising the imaging resolution.

There is no pre-alignment procedure for the probe insert assembly as there is with the pump insert assembly. The gun is imaged through the view port as previously stated which allows for the UV probe beam to be raster scanned until florescence is detected by the CMOS camera imaging the cathode. Once fluorescence is detected the user will then switch to using the piezoelectric motorized mirror closest to the gun to fine tune alignment. This fine tuning is assessed by imaging the cathode at crossover on a detector. The fine tuning alignment is finished once the electron counts cannot increase any further and the image of the gun

reflects the shape of the LaB_6 cathode. Once alignment is optimized the user should then engage the LabVIEW program in order to maintain stability of the probe UV alignment onto the cathode.

Switching between thermionic and photo-electrons requires manually tuning cathode voltage and Wehnelt bias voltage. A critical note is to not expose the cathode operating at thermionic temperatures to the UV probe. To switch from thermionic to photo-electrons the user first reduces the cathode voltage from normal operating voltages of 19 volts to approximately 13 volts. This will significantly reduce thermionic emission allowing the user to center the focused electron beam on the detector at crossover without causing damage. The cathode voltage is then reduced to 9 volts after which the user will unblock the UV probe laser allowing the photo-electron beam to be imaged on the detector at crossover. If the pulsed electron beam is not detected the user will have to perform coarse or fine alignment procedures. Coarse alignment is necessary if the user does not observe any florescence from the CMOS camera imaging the cathode through the cathode view port. In Fig. 2.8f and g the absence and presence for florescence is observed, respectively. Coarse alignment is performed by a raster scan of the UV probe beam by hand using the motorized mirror that received the UV probe beam, Fig. 2.8a and d. Once florescence from the carbon of the carbon portion of the cathode the user will switch to a fine alignment. Fine alignment is achieved using the piezoelectric control box to finely move channels 3 and 4 until photo-emission is imaged on the detector. Fine alignment is finished when the user has maximized intensity of the electron beam at crossover. Coarse alignment time for the fs UV probe can be improved by utilizing LabVIEW stabilization program. The user should engage the program and by hand move the beam such that it is within 100 pixel of the last used center positions noted in the DETEM laboratory log. This program can not be used for the ns UV probe however due to complete removal lower harmonics after fourth harmonic generation. When switching back to a thermionic beam the user must first block the laser from the cathode, then slowly reheat the cathode by slowly returning the cathode voltage back to about 19 volts.

2.2.4 Data Acquisition System

The data acquisition and software for the DETEM was contracted through the company Integrated Dynamic Electron Solutions (IDES). IDES delivered a software package and scripts that work within the Gatan Digital Micrograph® (DM) software suite. Additionally, IDES designed and built the hardware architecture for the data acquisition (DAQ) set up. This section will detail use of the software and describe the DAQ hardware setup, however it is noted that this is a summary of documentation and in-person training provided by IDES.

Figure 2.9: The IDES data acquisition software components in Gatan's Digital Micrograph® software suite. a) IDES Mode Selector interface where the user first selects the experimental modality, such as a fs pump/fs probe or fs pump/ns probe experiment. b-c) IDES Timeless Acquisition interface for the user to select the experimental parameters and start data acquisition. d) IDES Device Debugger interface for the user to monitor and debug any issue with the device controlling the temporal delay between pump and probe.

The front end of the IDES DAQ software used for running experiments are the three DM interfaces shown in Fig. 2.9. The Mode Selector interface, Fig. 2.9a, depicts the six modalities implemented for the DETEM by IDES, introduced in Fig. 2.2. Three stroboscopic modes - fs pump/fs probe, fs pump/ns probe, and ns pump/ns probe - were implemented and tested. The single-shot modes describe experiments where the sample is photoexcited by a single pump pulse with various ns or fast-camera probe options. However, due to only one ns laser being currently employed for the DETEM only the fs/fs and fs/ns modes are available.

In the latter mode, both lasers are electronically triggered with a set variable time delay using a digital delay generator (DDG). By pressing either the fs/fs or fs/ns button, scripts are ran in the background that initialize the proper parameters for the selected experimental setup. The fs/ns mode requires that the user matches the pulse picker (pp) value to the value used in the Pharos user application, which then properly initializes the DDGs.

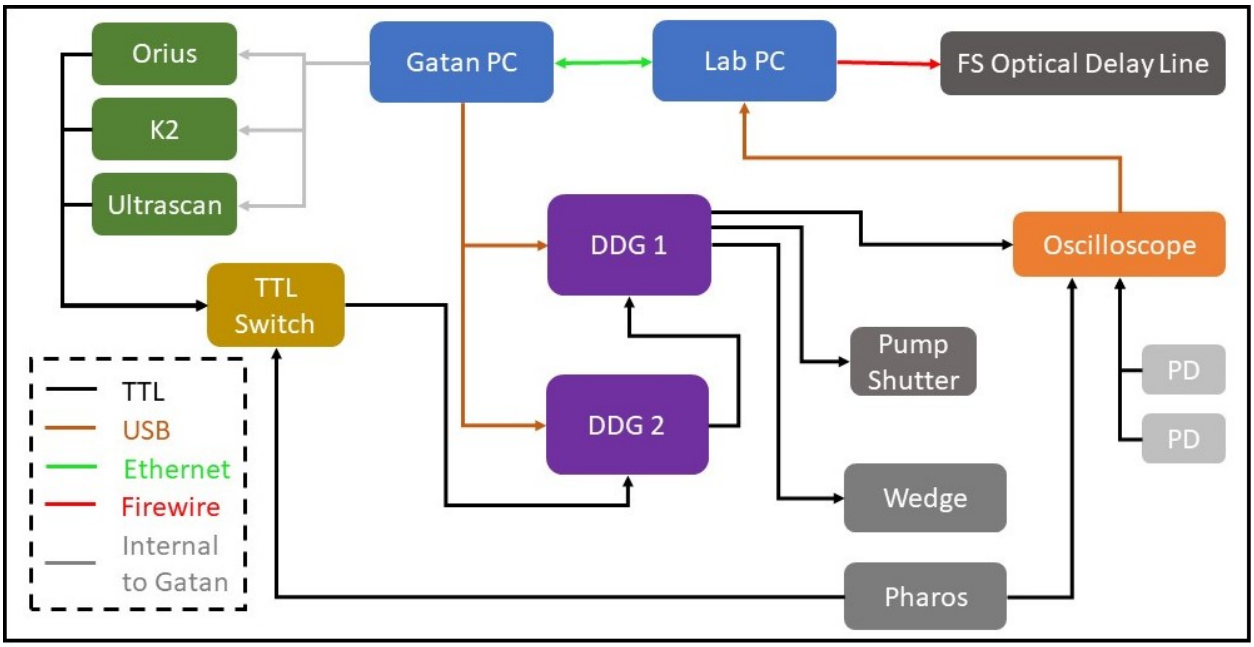

Figure 2.10: Schematic of the hardware set up and connections for the IDES timing. Color scheme for call outs is as follows: blue for computers, green for electron detector, purple for digital delay generators, mustard for custom IDES TTL switch, orange for oscilloscope, and grays for laser related items.

The IDES Timeless Acquisition interface, Fig. 2.9b and c, is where the user selects a device to use for scanning and to start that scan. Typically, the devices produce a temporal delay between pump and probe lasers, however it is possible to scan through, for example, sample tilt with the 'TEM;A' and 'TEM;B' devices for alpha and beta tilt. For the current DETEM setup, two devices are selected in the Timeless interface for fs/fs and fs/ns modes previously mentioned. For the fs/fs mode the 'TS' device must be selected from the drop down menu, and for the fs/ns mode the 'DGB;A' device must be selected. TS stands for translation stage resulting in the DAQ software to control the position of the delay line. The 'DGB;A' selects channel A of the digital delay generator labeled DDG1 in Fig. 2.10

producing a delay between the fs pump and ns probe lasers. After ensuring the proper device selection from the drop down menu, the user must then decide to do either a linear or custom scan on that axis. A linear scan has five input options and one drop down menu option. The 'Offset' value, not often used, allows the user to shift the time zero value for the scan. For a linear scan it is important to state how many steps you want between the starting and ending values which correspond to the 'Step', 'Initial', and 'Final' inputs seen in Fig. 2.9b, respectively. Additionally, the user can control how many scans are conducted and the directionality of the scans by modifying the 'Loops' input and selecting from the drop down menu to the right of this input reading 'Forward/backward' in Fig. 2.9b. The directionality options for the scan are 'Forward/backward', 'Forward only', and 'Backward only'. The user can instead run a custom scan by creating a text file that is a column vector of time values, with the example showing the 'D:\Data\Delays.txt' next to the button for selecting the custom file in Fig. 2.9c.

The IDES Device Debugger interface, Fig. 2.9d, is accessed by pressing the control button and clicking on the 'Device' button in the top left hand side of the Timeless interface. This interface allows users to conduct basic troubleshooting and testing procedures. For instance, if a device appears to not be working it is possible for the user to select the device from the drop down menu titled 'Name'. The user will be able to read the type of port the device uses, what device type is and what the axis of movement for the device is. In Fig. 2.9d the device named 'DG;A' is channel A of a Berkeley Nucleonics digital delay generator (DDG) model BNC 577 on the fourth RS 232 port. Additionally, the user has the ability to read and change the time zero position, currently displaying 236.7 ns in Fig. 2.9d. The last input is labeled 'Target', which can move the device to the desired delay by pressing the 'Move' button at the bottom of the interface. In this example however the device has not been opened as indicated by five of the bottom six buttons being grayed out in Fig. 2.9d. Once the device has been opened to the device debugger interface the user has the ability to then close the device, initialize the device, enable the device, disable the device, or move

the devices position as discussed above. The initialize function is used for the optical delay line as this command homes the stage, however for the DDGs this action does nothing as the DDGs are initialized when opened.

The IDES DAQ system hardware architecture is graphically detailed in Fig. 2.10. The backbone of this setup is the Gatan computer, which acts as the command and control unit for data collection. The Gatan PC controls the electron detectors (green) and DDGs (purple), as well as it sends commands to the lab computer which controls the optical delay line for fs/fs experiments. The procedure for collecting a fs/fs scan is for the Gatan computer to first command then query the position change for the optical delay line through the lab PC. Then the Gatan PC commands the active electron detector to capture an image. A fs/fs scan is then collected by repeating this process. A fs/ns scan is done by a similar iterative process, but instead the Gatan PC updates both DDG settings which are responsible for synchronizing the ns Wedge laser to the fs Pharos laser. This is achieved by passing the internal photodiode (PD) signal of the Pharos to DDG 2 through the TTL switch. The signal will be delayed by almost a full period of the experimental repetition rate before being passed to the DDG 1 as a trigger. At DDG 1 the signal delay to the Wedge laser is varied depending on the scan delays used in the Timeless interface. In this way, the Gatan PC controls the delay between the fs pump and ns probe. There is also an oscilloscope two-channel PicoScope 3206D) that is used to test timing for the fs/ns or ns/ns data collection modes. For the fs/ns modes the two input channels are the output of the Pharos laser and the photodiode in the ns probe path. There is an additional PD meant for when a second ns laser is added to the build, which will provide feedback on the timing between the two ns pump and probe pulses.

2.3 Spatial and Temporal Overlap

2.3.1 Spatial Overlap

Spatial overlap between the pump laser and the pulsed electron beam at the sample inside the TEM is achieved with a single or few shots from the pump laser onto a gold coated Quantifoil® TEM grid. The Quantifoil® grids are advantageous due to the ability to not only visualize the thermal footprint of the pump laser inside the microscope but also with an optical microscope, as observed in Fig. 2.11b and a, respectively. In the optical microscope image, Fig. 2.11a, there are four pump pulse footprints highlighted by an orange ellipse. As mentioned in Section 2.2.2, the footprint is elliptical due to the 22 degrees angle between the sample plane and the optical path for the pump beam. A clear demonstration of the spatial overlap is observed in the before and after TEM images in Fig. 2.11c and d. Additionally, sputter coating a thin 1-2 nanometer film of gold enhances the contrast inside of the TEM and makes the thermal footprint of the pump laser smaller. This improves the repeatability and accuracy of spatial overlap at the eucentric height of the sample inside the TEM.

Aligning the laser pump to the electron probe requires two different actions depending on the axis that is misaligned. First, in addition to standard microscope alignment procedures it is necessary to ensure that the image alignment of the TEM is correct. This is a non-standard daily alignment procedure but it is critical as it ensures that there is no lateral shift of the image as magnification is changed. Additionally, it is necessary to return the objective lens current back to the previously recorded value in the H9500 Lab notebook for a specific magnification, which is done by reading the objective lens current from the "Lens" tab in the "Column control" window. However, this change in objective lens current requires repeating the daily alignment procedures as this changes the image plane. Once this is done, the pump laser can be sent to the sample using the laser feedback system entering the last-used coordinates. The H9500 allows the sample to be pulled back into a retracted position which keeps the sample from being damaged, and it is standard procedure to use

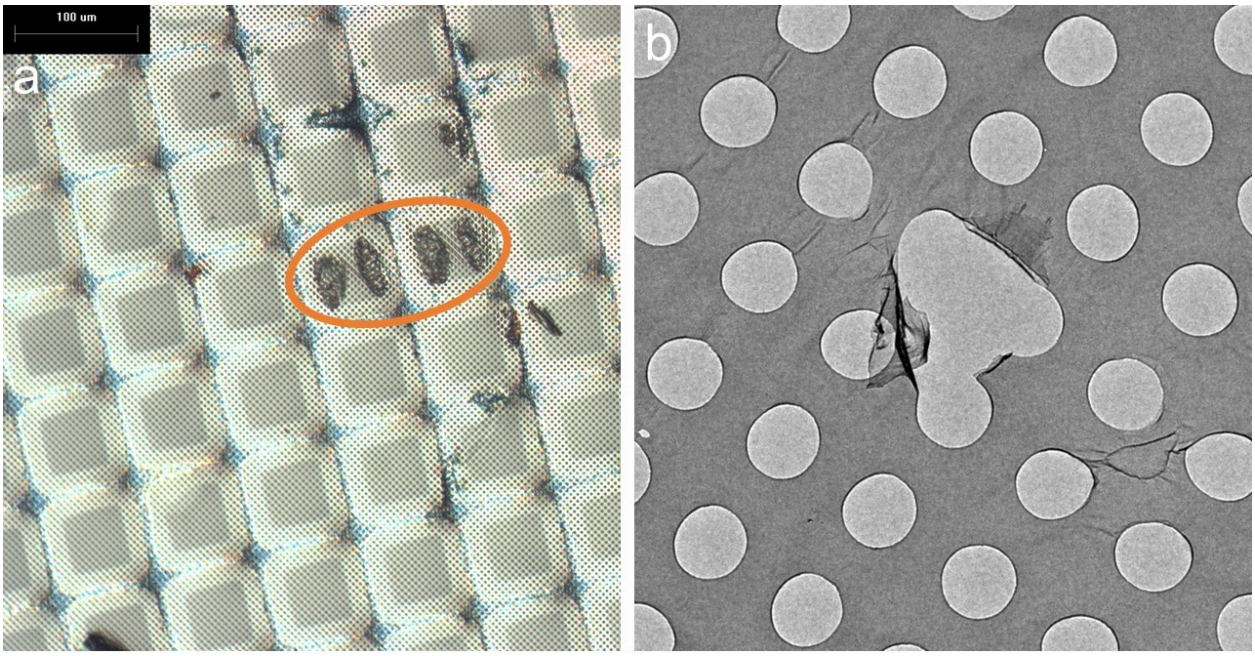

Figure 2.11: a) Optical microscope image of a Quantifoil® showing four thermal footprints from single shots of the pump laser (encircled in orange). b)TEM image of a Quantifoil® exhibiting the thermal damaged caused from a single pump pulse.

this sample position while letting the pump laser stabilize. Once the pump laser feedback system stabilizes, the pump/probe overlap can be checked by sending one or a few laser pulses to an undamaged region of the Quantifoil® grid. To correct misalignment in the x-axis of the sample it is necessary to move the laser beam in the inverse x-direction on the right camera for the feedback LabVIEW program using the motorized piezo mirrors. To maintain the probe beam path in the safe regions avoiding beam clipping it is necessary to also move the x-axis position of the left camera to keep the beam in the center of the safe region, Fig. 2.7c. Alignment for the x-axis is then refined using this procedure taking a single shot at a new Quantifoil® grid position, and then refining the position in the x-axis with the feedback program. Correcting the y-axis requires a different procedure of moving the sample rather than the pump laser. This is because the square 5 mm prism mirrors of the pump insert do not allow for much movement along the y-axis before clipping occurs. Thus, by decreasing the z-axis position of the sample the pump laser position is decreased along the sample y-axis. This then requires that the user re-focuses the objective lens focus. In

this way, both the sample and image planes are moved to achieve pump/probe overlap along the sample y-axis. Note, that each time the objective lens current is changed the microscope alignment must be repeated.

2.3.2 Temporal Overlap

After spatial overlap of the laser pump and electron probe beams is achieved, the pulses need to be overlapped in time at the sample position. Depending on the temporal width of the probe pulse, fs or ns, different methods for determining temporal overlap are used. Photon-induced near-field electron microscopy (PINEM)[82,83,84,85] is the method used in fs-ps stroboscopic mode. For the ns time scales, PINEM cannot be used since the laser peak powers are too low and instead time-resolved convergent beam electron diffraction (CBED) on a silicon lamella is used.

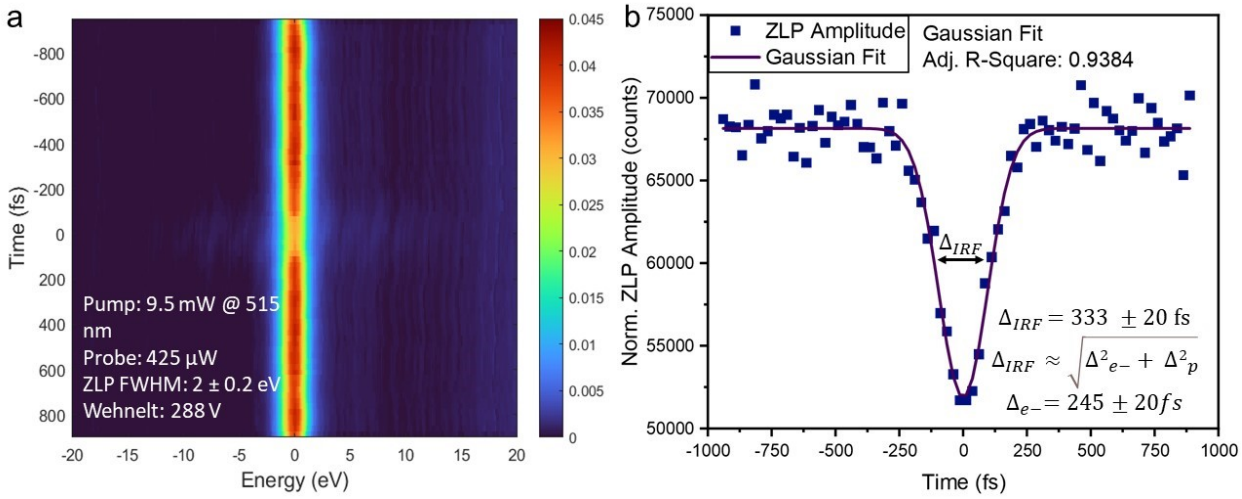

Figure 2.12: a) PINEM spectra that have been drift-corrected based on the zero loss peak (ZLP) and each normalized to the total intensity of the spectra, showing a decrease in ZLP amplitude around 931.85 mm on the delay stage. b) Plot of unnormalized ZLP amplitudes and a Gaussian fit used to determine an electron pulse width of ~227 fs demonstrating the instrument is capable of operating in the single electron per pulse regime.

Photon-induced near-field electron microscopy (PINEM) is a technique discovered in the group of Prof. Zewail at the California Institute of Technology. Besides interesting scientific applications, it is a useful technique to determine temporal overlap between fs laser and electron pulses[82,83,84,85]. PINEM is a result of light-matter interactions between the

pump laser and the sample that produces an evanescent field that in turn interacts with the electron probe pulse. The interaction between the evanescent field and electron probe pulse produces quantized energy gains and losses at multiples of the pump laser energy that are observable around the zero loss peak (ZLP) with electron energy loss spectroscopy (EELS). Fig. 2.12a shows such EEL spectra as a function of delay stage position. A depletion of the ZLP intensity at 0 eV is seen, with concurring faint lobes to the red and blue sides of the ZLP. The effect is only observed when there is spatial and temporal overlap between the laser pump pulse and electron probe pulse, which provides a direct measure of the instrument response function[85]. PINEM experiments were conducted to precisely determine the position on the delay stage that corresponds to temporal overlap between the pump and probe pulses for the DETEM, with data shown in Fig. 2.12. The combined normalized spectra, Fig. 2.12a, reveals a decrease in the amplitude for the ZLP around 931.85 mm due to the PINEM effect. The amplitude of the ZLP, plotted in Fig. 2.12b, clearly displays a decrease in amplitude that can be fitted to an inverted Gaussian fit (note that the time range was cut off towards negative time delays). Temporal overlap is then found to be at 931.8423 mm on the delay stage. Additionally, as shown previously in the literature the full width half maximum (FWHM) of the Gaussian is a convolution of the laser pump and electron probe pulse widths[85]. This yields an IRF with a $\sim$320 ps FWHM for the experimental conditions indicated in Fig. 2.12a.

CBED is an attractive method for determining temporal overlap for a ns probe due to its sensitivity to sample motion and vibrational modes[86,87,88,89]. Specifically, the Kikuchi lines are sensitive to crystal vibrations perpendicular to the electron beam path which are excited due the the photoexcited electrons of the material dissipating energy to the lattice as the electrons decay back to the ground state following this photoexcitation[86,89]. This transfer of energy to the lattice not only actives vibrational modes but can additionally active mechanical motion of the sample due to the dissipating energy. These motions occur on the order of tens to hundreds of ps after photoexcitation allowing the assumption that

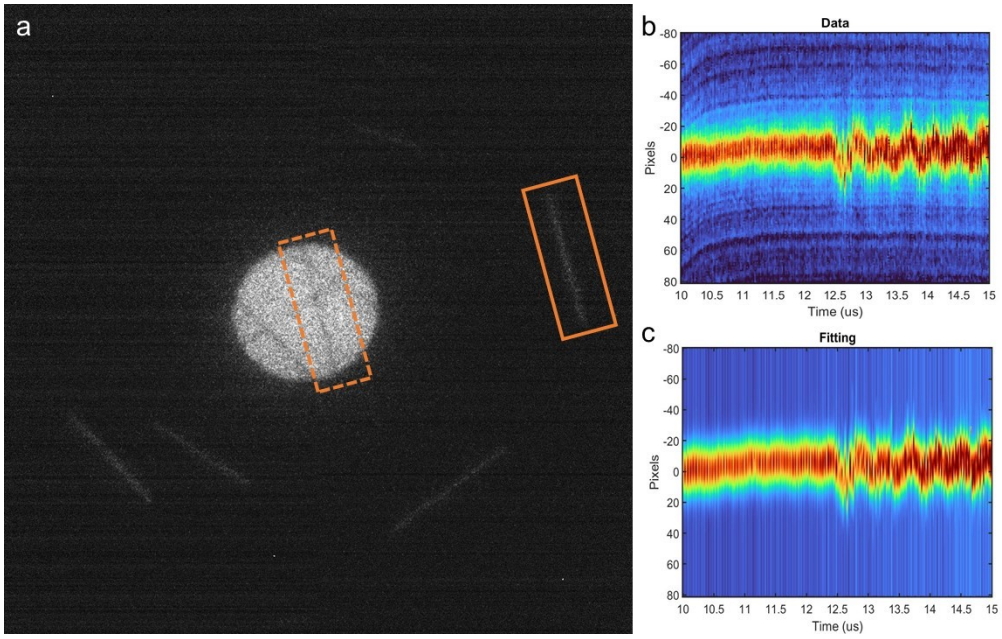

Figure 2.13: a) Single-crystal CBED pattern from a silicon lamella with excess and deficit Kikuchi lines highlighted by solid and dashed rectangles, respectively. The position of the Kikuchi lines are sensitive to vibrational modes perpendicular to optical axis of the TEM, as well as sample motions along the optical axis. b and c) Fit results for the excess Kikuchi line highlighted in a, showing that temporal overlap for the fs pump and ns probe pulses occurs at a delay of 12.45 μs.

the signal is instantaneous with respect to the ns probe[89]. We thus determined the temporal overlap between the fs laser pump pulse and the ns electron probe pulse in the DETEM by analyzing the Kikuchi line oscillations for a single-crystal CBED pattern of a silicon lamella. The obtained pattern, Fig. 2.13a, has the excess and deficit Kikuchi line pairs highlighted by solid and dashed rectangles, respectively. Analysis for this data consists of selecting a region of interest, such as the solid rectangle in Fig. 2.13a, and summing the intensities along the Kikuchi line. A Gaussian fit of the resulting profile can then be used to obtain the oscillations of the Kikuchi line position. The data and fitting results are best visualized by concatenating the summations as a function of time delay, as seen for the data in Fig. 2.13b and c. The delay of 12.45 μs for DDG 1, where the Kikuchi line starts oscillating Fig. 2.10) was determined to be the position of temporal overlap for the fs pump and ns probe beams.

2.4 Characterization of the DETEM

2.4.1 Pump Laser Spot Size Calibration

An important experimental parameter to know in a pump/probe experiment is the laser pump fluence. The laser fluence (often expressed in units of mJ/cm^2) determines the yield of excitation of the material, such as the carrier density in semiconductors or the percentage of excited molecules. In particular, in the field of photoinduced phase transitions, a non-linear dependence on laser fluence and fluence threshold effects are often observed, which relate to the inherent (cooperative) interactions between the consituents (atoms, molecules) in the material. For an all optical pump/probe instrument laser spot sizes are often determined using knife edge scans in the sample plane measuring the power of the transmitted light as the edge is moved across the beam. This is not possible in the DETEM as there is no way to access the sample area to place a detector to measure the change in laser power. Instead we used the camera from the pump beam pointing stabilization program as a virtual sample. The camera was calibrated with respect to the sample to obtain a scaling factor that relates the camera pixels to real space distance on the sample. The calibration was done by recording a sequence of damage spots on the Quantifoil® grid and determining their relative separation in real space using the well-known hole separation of 2 μm. The position of the beam on the camera was concurrently recorded which leads to a real space / pixel calibration table. For the DETEM this procedure produced a 2.5 μm/pixel ratio leading to FWHM values for the elliptical spot of $\sim$20 μm and $\sim$46 μm for the minor and major axes, respectively. With the major axis radius of $\sim$23 μm and the angle of 22 degrees between the laser and the sample, the focus size becomes $\sim 10 \times 9$ μm^2. The laser fluence on the sample is then calculated by dividing the pulse energy (average power just before TEM divided by the repetition rate) by $10 \times 23 \times \pi$ μm^2.

2.4.2 Photocathode/Electron Pulse Characterization

The characterization of the electron pulse properties is important to estimate the feasibility of experiments and tune the parameters according to the experiment's needs. Electron pulse properties of relevance are the number of electrons per pulse, the energy spread of the pulse, and the electron coherence. Temporal resolution is also an important parameter, which is determined for fs pump/probe mode using PINEM, covered in 2.3.2. The instrument variables that effect these parameters are the UV probe power and the Wehnelt bias. To reliably determine the number of electrons, the Gatan K2 detector was used in counting mode to ascertain the number of electrons as a function of UV probe power and Wehnelt bias, for both fs and ns probes. Additionally, the EEL spectra were collected for the ns probe to determine the energy spread of the electron probe pulse.

Nanosecond probe pulse characterization

For the ns probe, the electrons per pulse and the FWHM of the ZLP were investigated by systemically varying the power of the 266 nm UV probe beam and the bias of the Wehnelt, Fig. 2.14. The results are displayed in Fig. 2.14a and b. The effect of Wehnelt bias on the electrons per pulse is complex because the Wehnelt assembly acts not only as an electrostatic lens but it also decelerates the photoelectrons[79]. As seen in Fig. 2.14a, the observed trend is for the electron counts to decrease reaching a minimum around 360 V before increasing to a maximum at about 750 volts. This is due to the focusing of the Wehnelt assembly, as the effective focal length decreases as voltage increases[90]. The local minimum around 360 V may be due to a focal length that increases electron-electron interaction resulting in a radial expansion of the electron probe pulse. In this case, electrons in the probe pulse are cut off by fixed apertures in the H9500. The approximately linear trend for electrons per pulse as a function of UV probe power, Fig. 2.14b, is more intuitive, when considering the photoelectric effect. There is not a clear shift into the saturation regime when considering the electrons per pulse as a function of UV probe power graph,Fig. 2.14b, however it is likely these UV

powers are close or at the begining of this regime when considering the nonuniform energy distribution for the zero loss peaks in Fig. 2.14e&f at a zero bia for the Wehnelt. This saturation regime is where the electron pulse density becomes large enough that further photoelectron generation is suppressed due to space charge effects[79,90,91]. The number of electrons per pulse though is about 3 orders of magnitude lower than other time-resolved TEMs with nanosecond probes[79,90]. This lower generation is due to a number of differences between instrumental setups. The 3 orders of magnitude difference is likely due to the use of a tantalum disk cathode with a 7 ns UV pulse compared to the 50 μm guarded ring LaB_6 cathode and 1 ns UV pulse in the DETEM[91]. So, while the there are differences in results the observed trends for nanosecond electrons per pulse are congruent with literature[79,90,91].

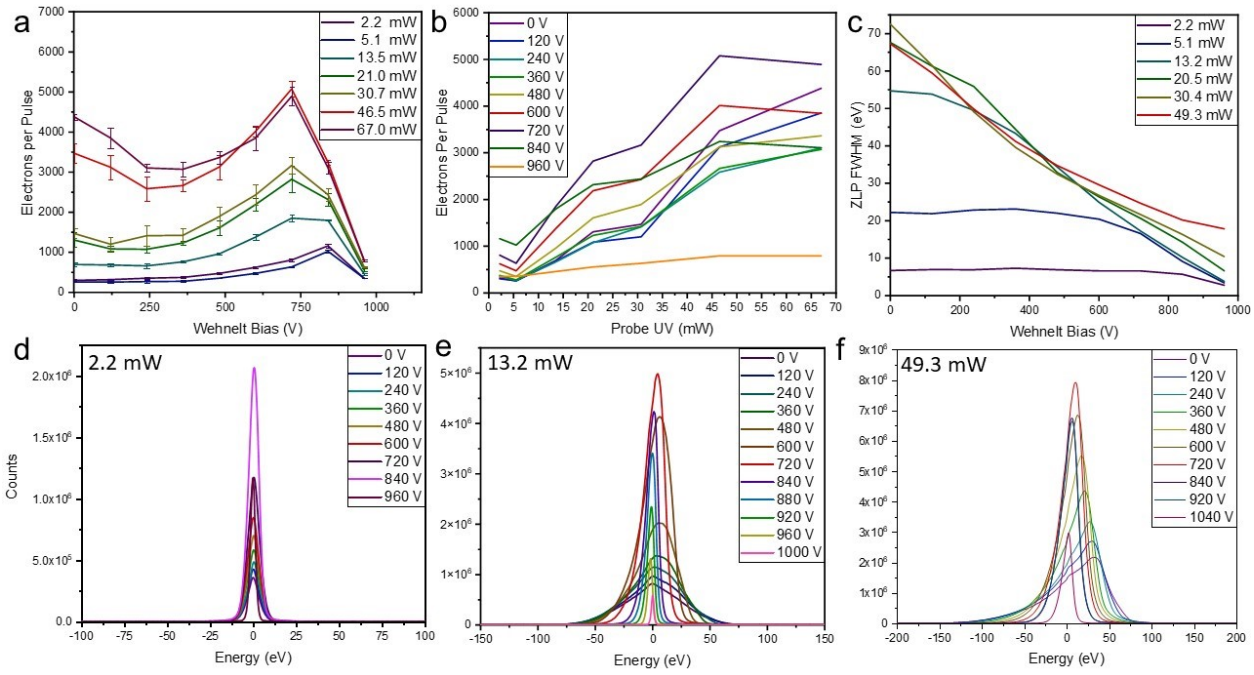

Figure 2.14: Characterization of ns electron probe parameters at 10 kHz. a) Electrons per pulse as a function of Wehnelt bias, revealing the complicated electrostatic lensing action of the Wehnelt assembly. A local maximum for electrons per pulse is observed around 720 V. b) Electrons per pulse as a function of probe UV power displaying a proportional linear relationship. c) The FWHM of the ZLP as a function of Wehnelt bias. The effect of Wehnelt bias is to minimize FWHM of the ZLP as bias voltage is increased. d-f) ZLP spectra at 2.2, 13.2, and 49.3 mW for the probe UV power, respectively, displaying the skewness at lower voltages for the 49.3 and 13.2 mW probe UV power due to deleterious electron-electron interactions within the electron probe pulse. At the lowest power (2.2 mW) and the highest Wehnelt bias (960 V), a FWHM of 2.78 eV was obtained.

The energy spread for the ns electron probe was also investigated by measuring the FWHM of the ZLP in the EEL spectrum, Fig. 2.14c. At higher probe powers a negative linear relationship between FWHM and bias is observed. This trend has been observed previously in the literature and it is understood to be an effect of the decreasing Rayleigh length of the electrostatic Wehnelt lens[79]. As the Wehnelt bias increases and Rayleigh length decreases the electron packet expands faster radially which decreases electron-electron interactions impacting the properties of the electron probe pulse, such as its energy spread. Additionally, the Wehnelt bias retards further photoelectron ejection which will also decrease the number of photoelectrons in the probe pulse. For lower UV probe powers (2.2 mW and 5.1 mW) the FWHM of the ZLP becomes almost independent of Wehnelt bias for these UV powers, attesting the reduced space charge effects in the electron bunches at these powers. The ZLP spectra for three different UV powers and as a function of Wehnelt bias are shown in Fig. 2.14 d-f. At 2.2 mW, Fig. 2.14d, the ZLP starts with and maintains a Gaussian shape, but for 13.2 and 49.3 mW (Fig. 2.14e and f) the ZLP peaks become skewed. The shape of the ZLP at these higher powers does become more Gaussian as the Wehnelt bias is increase. This is due to the complex nature of the Wehnelt which reduces electron-electron interactions as Rayleigh length decreases by expanding the electron beam, as well as increased cut of of lower energy electrons by apertures in the H9500[79,90,91]

Femtosecond probe pulse characterization

For the fs probe pulses only the electron counts and FWHM of the ZLP were collected, Fig. 2.15. As with the ns probe the total electron counts were determined using the K2 detector in counting mode but the electron energy loss data collected on the Ultrascan 1000 CCD. Interestingly, there appears to be two regimes for the fs probe that were not observed with the ns probe, Fig. 2.15a and b. At powers above 5 mW the trend appears to be logarithmic, with saturation levels being reached between 40 and 50 mW, Fig. 2.15a. At UV probe powers below 5 mW a linear trend is observed, Fig. 2.15b. The reason for these two distinct regimes

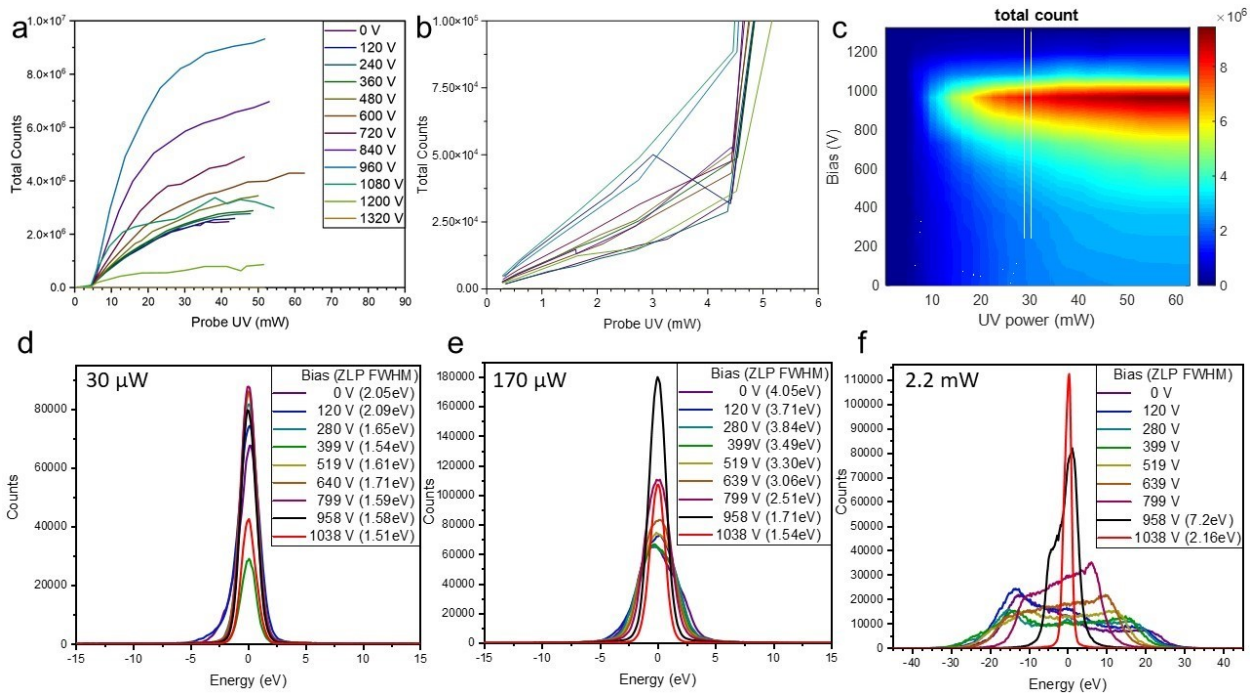

Figure 2.15: Characterization of fs electron probe parameters at 492 kHz. a) Total electron counts of the fs electron probe using the K2 detector as a function of probe UV power for various Wehnelt bias voltages. b) Total electron counts as a function of probe UV power zoomed into the region 0-6 mW. c) Interpolated heat map of total electron counts with Wehnelt bias for the y-axis and Probe UV power for the x-axis. There is a linear regime below ∼5 mW of UV power and a logarithmic regime above ∼5 mW. d-f) ZLP Spectra at 30 μW, 170 μW, and 2.2 mW for probe UV power, respectively. A Gaussian peak shape is maintained at the two lower probe UV power, with skewness appearing at approximately 0.5 mW and worsening with UV power. The 2.2 mW probe UV power demonstrates how electron-electron interaction deteriorate the energy resolution of the pulsed electron probe.

and the apparent power threshold around 4.5 mW is not entirely understood at present. The energy spread for the fs electron probe retains a Gaussian shape between 30 and 170 μW but by 540 μW energy broadening similar to that for the 49.3 mW ns probe data, Fig. 2.14f. At 2.2 mW, Fig. 2.15f, it only possible to obtain a Gaussian shape of the ZLP at high Wehnelt bias voltages. This indicates electron-electron interaction are significantly effecting the fs electron probe pulse. Except for the logarithmic regime in the fs electron probe data, our data matches that published similar instruments[92,85,79].

2.5 Conclusion

This chapter describes the development and implementation of the DETEM at UIUC which is based on a commercial Hitachi H9500 environmental TEM. The TEM modifications were entirely non-invasive, i.e. we made use of an existing port to guide the pump laser onto the sample and added a segment between the gun and the main column to guide the UV probe laser onto the cathode. The TEM retained the ability to produce high resolution images despite taking it off its vibrational dampening system. Switching between thermionic and photoelectric emission modes is relatively straightforward. Currently, there is one fs and one ns laser coupled to the TEM providing fs-pump/fs-probe and fs-pump/ns-probe data collection capabilities for the imaging, diffraction, and spectroscopy modalities of the TEM. Spatial and temporal overlap were reliably obtained and procedures were developed to stabilize the pointing of the laser beams and to determine the spot size on the sample. In ns probing mode, thousands of electrons per pulse can be obtained, with energy resolutions ranging from 2.6eV to 40+eV, depending on the Wehnelt bias. In fs mode, an energy resolution of $\sim$2 eV and temporal resolution of $\sim$1 ps (both FWHM) were obtained, as determined by the photoinduced near-field microscopy (PINEM) effect. Since its start of operation, the DETEM has been used to investigate the dynamics of three-dimensional electron gases in vacuum on the ps time scale (Chapter 3), for photoinduced phase transitions in molecular spin crossover and metal-oxide nanomaterials (Chapters 4 and 5), as well as other in situ TEM investigations of catalytic nanomaterials under light irradiation.

CHAPTER 3: TRANSIENT LENSING FROM A PHOTOEMITTED ELECTRON GAS

3.1 Introduction

The study of non-equilibrium dynamics of charge carriers, such as electrons, holes, or ions, is crucial in many scientific and engineering fields, including solar energy conversion, plasma physics, and the development of high-brightness electron and X-ray sources. Carrier motion often unfolds on ultrafast time scales and requires tools that can directly visualize the dynamics with appropriate spatial and temporal resolutions, i.e. Ångstroms–micrometers (Å–μm) and fs–ns (fs–ns), respectively. The DETEM at UIUC offers such capabilities in one table-top instrument.

Here we use the Illinois DETEM to visualize the evolution of a photoemitted 3-dimensional electron gas (3DEG) generated with a fs laser pulse from a copper surface in a static magnetic field[93]. This work provides a framework and lays the groundwork to elucidate the non-equilibrium dynamics of confined charge carriers, for example inside materials. Confined electron gases[94,95] are known to possess properties such as high carrier mobilities[96,97,98,99], Edelstein effect[100], Rashba splitting[101], flexoelectricity[102], quantum Hall effects[103,104,105,106], and superradiant damping[107,108]. It is important to understand and control these phenomena for technological improvements to be made in areas such as quantum computing and thermoelectric power for example[109,110,111,112,113]. Confined electron gases have been studied using various spectroscopic techniques such as pump-probe Kerr rotation, angle-resolved photo-electron spectroscopy, and frequency- and time-domain THz spectroscopy

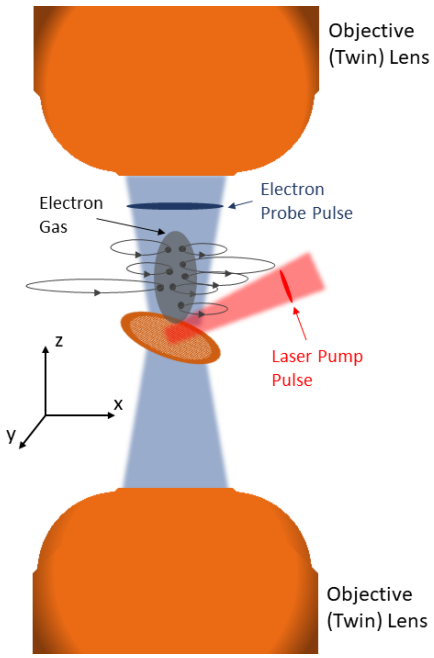

Figure 3.1: Generalized illustration of the electron gas ejected from a copper grid by a fs pump laser pulse that is probed by a subsequent electron probe pulse. The electron gas expands along the optical z-axis, while the electrons undergo cyclotron motion in the x, y-plane.

in materials and devices, such as 2D black phosphor and at heterointerfaces[114,115,116,117,118,119,120,121,122]. For electrons subjected to an external magnetic field, these techniques provide information about the cyclotron oscillations that the electrons undergo perpendicular to the magnetic field. The trajectory of the oscillating electrons are also called Larmor orbits. Within the framework of quantum mechanics, the energy of electrons undergoing cyclotron motion can be quantized into eigenstates called Landau levels. The transition between Landau levels are known as cyclotron resonance and the frequencies, line widths, decays have been studied to determine band structure, effective masses, carrier densities, mobilities and scattering times in semiconducting materials[107,119,123,124,120,121]. Quantum effects will arise when the eigenstate energies are significantly greater than the mean thermal energy, which means experiments are carried out at low temperatures and/or with high magnetic fields.

The work presented in this chapter on the dynamics of a 3DEG in a static magnetic field represents an important first step towards studying confined charge carriers within materials

using an ultrafast transmission electron microscope. For example, studying 2-dimensional electron gases at the heterointerfaces of SrTiO/LaAlO, AlGaAs/GaAs, and AlGaN/GaN systems[125,126,127]. The benefit of using an ultrafast electron microscope is that it provides fs to ps temporal resolution with nanometer to micrometer spatial resolution. Spectroscopic techniques can offer the temporal resolution but spatial information is lost. Similarly, conventional microscopy techniques offer spatial resolution at the loss of temporal resolution. Furthermore, the ability to image, with ps temporal resolution, the dynamics of photoemitted electrons is valuable to plasma community, as it is important that experimental work in tandem with computational findings[128,129,130,131,132,133,134,135,136]. This imaging capability is also highly desirable for research into high brightness sources for use in x-ray free-electron laser facilities as well as for ultrafast electron diffraction and microscope instruments[137,138,139 140,141,142,143,144,145,146,147].

The following sections will detail the methods and results on the dynamics of a photo-generated 3DEG as it undergoes cyclotron motion inside the electron microscope (Fig. 3.1). Additionally, the effects of the 3DEG on the probe electrons at different focus conditions of the microscope will be explored. Systematic variations in pump fluence and wavelength were also conducted. Lastly, for completeness, an analytical model and simulations carried out by Omid Zandi will be presented to unify the findings.

This chapter is in part based on the work published in reference [93]. O. Zandi, A.E. Sykes, and R.M. van der Veen designed the experiments. O. Zandi, A.E. Sykes, R.D. Cornelius and F.M. Alcorn performed the experiments. O. Zandi, A.E. Sykes, and R.D. Cornelius analyzed the data. O. Zandi and B. Zerbe modeled the data. O. Zandi, A.E. Sykes, B. Zerbe, P.M. Duxbury., B.W. Reed, and R.M. van der Veen interpreted the data and wrote the manuscript.

3.2 Methods

Using the DETEM described in Chapter 2, we conducted the experiments in the

low magnification (LM) mode of the instrument using the fs-pump/fs-probe scheme to collect images, which were then used to create real-time movies of the 3DEG dynamics. All experiments were conducted with the Pharos laser operating at 490 kHz. The Orpheus OPA was operated at pump wavelength of either 690 nm or 528 nm at powers ranging from 73-977 mW (5-74 mJ/cm^2). The probe laser, 256 nm, was operated at powers ranging from 6.5-9.7 mW provide a fluence on order of 14-25 nJ/cm^2 for the 50 μm diameter guarded ring LaB_6 cathode from Kimbal Physics. This is expected to generate hundreds of electrons and provides an electron probe pulse length on the order of $\sim$750 fs. The experiments used a 3000 mesh hexagonal copper foil (SPI catalog # 02903C-AB) supported by two bare copper gilder 1.5 mm aperture grids (Ted Pella catalog # GA1500). These grids with 4.6 μm holes and 3.8 μm wire widths provide a fill factor of 66% which is most optimal for photoelectron generation. For ablation studies a 200 mesh copper gilder grid (Ted Pella Product # G200) was used for ease of indexing location, and because the grid bars width was 35 μm allowing for the minor axis of the elliptical pump profile to lay directly on the grid. In all experiments, unless otherwise noted, the sample was tilted to 15 degrees towards the pump laser. Without sample tilt the pump laser impinges upon the sample at 22 degrees to the sample surface, thus the 15 degree tilt changes this angle to 37 degrees to minimize the elliptical pump profile.

A circular region of interest (ROI) method was used to process and analyze the collect data producing ROI difference traces. The ROI region was selected using the second peak, the image labeled 174 ps in Fig. 3.2, to inscribe a circular region of interest, an example in the bottom right panel in Fig. 3.2. The area inside the region of interest was summed with the summation value in the first image subtracted to create a difference ROI trace, see Fig. 3.3a or 3.5d for examples of difference ROI traces. Images were collected with a 1 s exposure time and normalized to the total counts in each image to account for fluctuation in probe intensities.

While conducting these experiments, the microscope was operated in non-standard

conditions due to the need for out-of-focus conditions. Conventionally, the lenses in an electron microscope have fixed, calibrated currents with factory settings depending on the operation mode and magnification selected. In the Hitachi H9500 there are two variable lenses that users can regularly change, namely the brightness (illumination area on the sample) and focus lenses. However, due to the out-of-focus conditions these experiments were conducted in, it became necessary to manually adjust other lenses in the projection system in order to produce the best quality image and magnification. Furthermore, the LM mode for the microscope operates at a fixed objective lens current, which controls the magnetic field in the sample area. It was thus necessary to manually adjust lenses after the objective lens to obtain desired image quality and magnification for altered objective lens currents.

3.3 Direct Visualization of Electron Cyclotron Oscillations

In this section the ps-resolved pump-probe scans that directly visualize the cyclotron oscillations will be presented and described. First, the pump-probe technique works by controlling the time delay between the pump and probe pulses. The pump pulse, a ∼225 fs laser pulse in this work, will excite the sample taking it out of equilibrium after which dynamics occur as the sample moves back to equilibrium. The probe pulse, here a ∼750 fs electron pulse, then interacts with the sample creating a snapshot of the sample with a known time delay with respect to the pump pulse. In this way the images in Fig. 3.2 containing about 500 thousand probe pulses were collected at a known time delay. Strikingly, the images in these experiments reveal localized distortions that occur periodically, which in Fig. 3.2 are magnifying barrel-type distortions with a period of ∼164 ps. A 3DEG is photogenerated from the sample grid by the pump laser pulse. The electrons in the gas contain a velocity component perpendicular to the magnetic field that lies parallel to the electron-optical (z) axis in the TEM and these electrons then undergo a circular motion, called cyclotron oscillation, driven by the Lorentz force, $F = q(v_\perp \otimes B)$. The cyclotron

motion can be described by equating the Lorentz force to the centripetal force, $F = \frac{mv^2}{r}$, which allows for the cyclotron frequency to be solved for, *i.e.* $f = \frac{1}{T} = \frac{v_\perp}{2\pi r} = \frac{qB}{2\pi m}$, where T, q, and m are the oscillation period, the electron charge, and electron mass, respectively. The distortions in the images seen in Fig. 3.2 are then due to the probe electrons' repulsive interaction with the 3DEG.

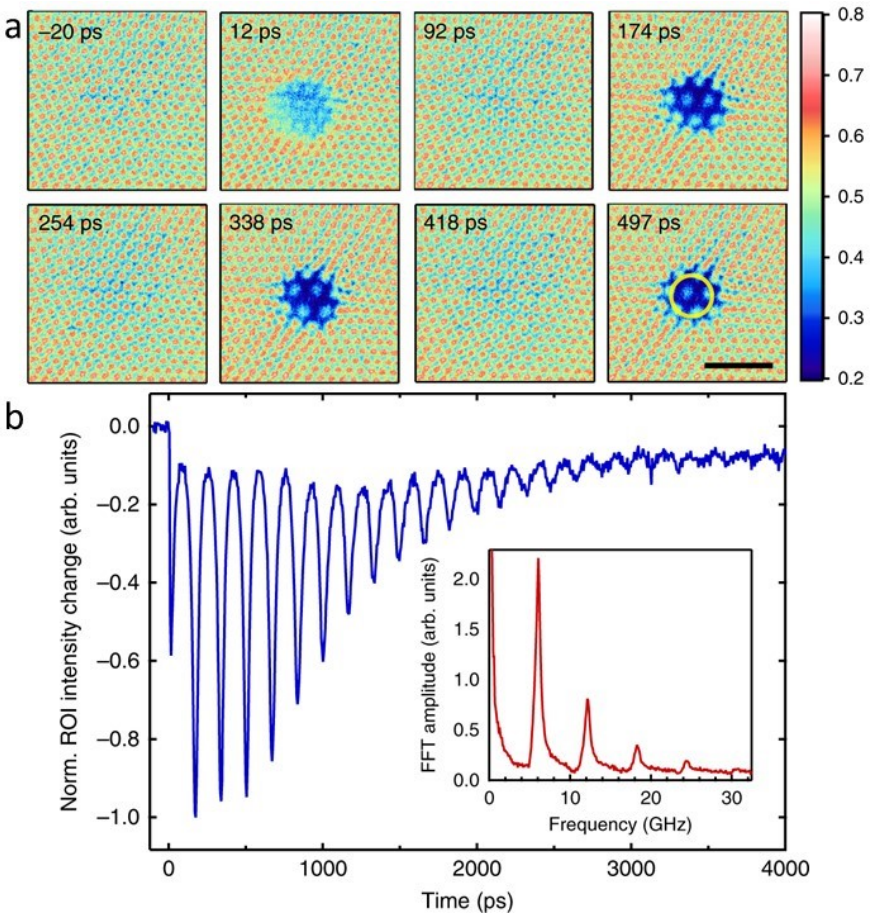

Figure 3.2: **a** Series of images extracted from a ps-resolved UEM movie (528 nm, 200 fs, 30 mJ/cm^2 laser excitation) with the objective lens (OL) and intermediate lens (IL) currents set to 0.7 and 0.65 A, respectively. The time delays correspond to the first few local maxima and minima for this scan. A typical region of interest (ROI) circle is indicated in the last frame. The scale bar for all images at the bottom right is 50 μm.**b** ROI difference intensity (relative to before time zero) as a function of time delay for data set and ROI in **a**. The ROI analysis highlights the long lifetime of the signal (4ns) and analysis of the inset FFT a 6.05 GHz frequency with higher harmonics due to peak shape.

Region of interest (ROI) analysis of the periodic image distortions at different magnetic field strength is shown in Fig. 3.3a. Three important observations can be taken from the ROI difference traces in Fig. 3.3a. The first is the striking difference in intensity

change between the first and second peak irrespective of magnetic field strength, which is explained with neumerical simulations to be presented below. There are no oscillations after the initial peak in the absence of a magnetic field, as expected. The second is the long life time of the signal of ∼4 ns, observed in Fig. 3.2b. Finally, the cyclotron frequency is linearly proportional to the magnetic field, $\frac{1}{T} \propto B$, as expected for the cyclotron period mentioned above. The latter observation is clearer in Fig. 3.3b where period (left, red) and calculated magnetic field (right, blue) form the ROI signal are plotted against the objective lens current (OLC). To understand the importance of this linear relation one must first be familiar with the magnetic filed of a solenoid lens, $B = \mu_\circ \frac{N}{L} I$ where $\mu_\circ, \frac{N}{L}$,and I are the magnetic permeability constant, turn density, and current, respectively. The linear dependence thus means that the observations truly reflect the cyclotron oscillations and that the 3DEG is subject to a field that can be approximated as uniform at early times approximately <1ns. The decay of the signal is a combination of factors, but is most easily understood by the free expansion of the gas along the electron-optical axis. As the 3DEG expands it will eventually exit the magnetic field but additionally this results in an increasing volume of the gas. An increasing volume means that the electric field of the 3DEG is subsequently decreasing by analysis of Gauss Law, $\bigtriangledown \cdot E = \frac{\rho}{\epsilon_\circ}$. Because the charge density, ρ, is decreasing with increasing volume the divergence of the electric field decreases, *i.e.* the electric field strength is decreasing and probe electrons will be repelled less by the 3DEG decreasing the signal of the distortions. Additionally, the magnetic field of the objective lens is approximately constant ±1 mm above and below the sample, but it starts to decrease beyond this region. This field gradient will result in the dephasing of the oscillations. The photogenerated 3DEG thus expands along the electron-optical axis while oscillating between a minimum and maximum radial size in the transverse direction (Fig. 3.1).

For thoroughness, the magnetic field calculation from the cyclotron frequencies were corroborated by measuring image rotation as a function of objective lens current and comparison to instrument data supplied by Hitachi High-Technologies. Image rotation, under

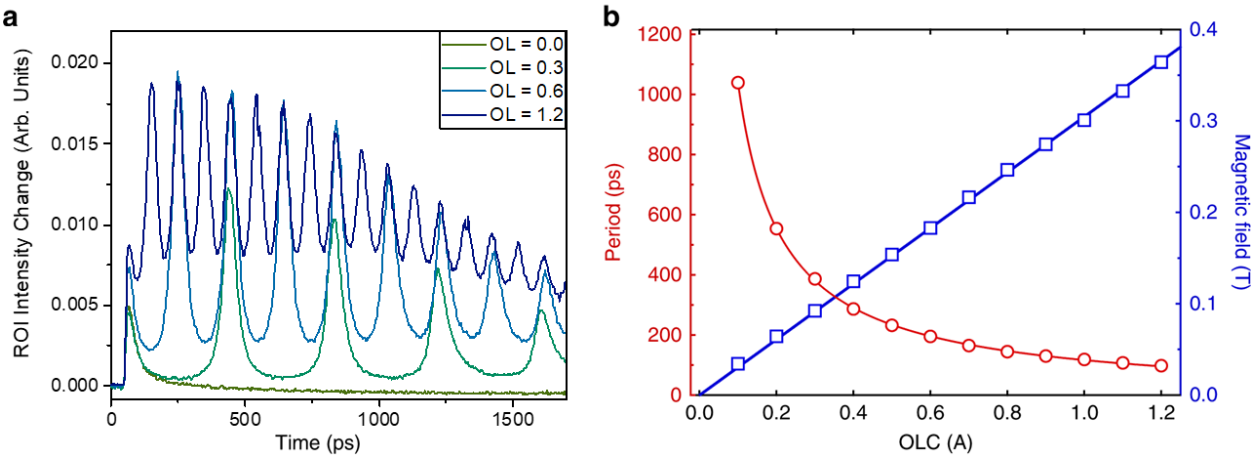

Figure 3.3: **a.** Series of ROI traces for various objective lens (OL) currents (in A) showing oscillations due to the 3DEG cyclotron motion. The intermediate lens (IL) current was set to 1.1 A. **b.** Cyclotron oscillation period (left, red axis), as a function of OL current (OLC). The magnetic field is obtained using the relation $\frac{1}{T} = \frac{qB}{2\pi m}$. and is plotted on the right axis. The solid lines represent fits.

the paraxial approximation, can be equated to the magnetic filed by $\theta' = \sqrt{\frac{e}{8m_r V}}B$, where m_r and V are the relativistic electron mass and acceleration voltage, respectively[148,149]. Thus taking images where only the objective lens is changed provide a means to measure the change in magnetic field as a function of objective lens current. This analysis though requires a fixed starting point as the equation will only provide the change in magnetic field and not the magnetic field strength. This requires that there is no residual magnetic field when the objective lens current is set to zero amperes. Fig. 3.4a plots the results of this analysis showing excellent agreement between the magnetic field calculations from the ROI and image rotation analysis.

Lastly, axial (z-axis) magnetic field data provided by Hitachi High-Tech (Fig. 3.4b) reveals that the magnetic field can be approximated as uniform ± 1 mm below and above the sample. Also, the magnetic field is linearly dependent to the objective lens current for the range of values used in these experiments (0-1 T, Fig. 3.4c). The uniformity is important because a non-uniform field will result in a dephasing of the cyclotron oscillations as the magnetic field varies. This dephasing is one cause for the decay in the ROI difference traces, as previously mentioned. Other causes are the loss of the number of electrons in the gas by re-absorption by the grid, velocity components in the x, y-plane large enough to escape the

magnetic field, and at longer times, collisions of electrons with the objective lens. In applying the cyclotron formula, $f = \frac{1}{T} = \frac{v_\perp}{2\pi r} = \frac{qB}{2\pi m}$, and using the free electron mass m, we assume that the electrons do not interact with each other (space charge effects are neglected) or that they are not affected by the positive image charges in the copper grid. Inclusion of such effects may lead to changes in the oscillation frequency which can be accounted for by using an effective mass (instead of the free mass) in the cyclotron formula. Current theoretical work by our co-workers investigates the parameter space where such space-charge and frequency shift effects may occur.

3.4 Dependence on Imaging Conditions

Here we detail the lensing effect of the 3DEG on the probe electrons at different focus conditions. As the probe electrons travel through the 3DEG the paths are deflected away from the optical axis due to negative charge of the 3DEG, thus acting as a diverging lens on the probe electrons. In order to observe the lensing effect of the 3DEG the microscope must be operated in conditions that are out of focus for the copper grid The reason is that in a focused real-space image, the post-sample lenses map the spatial positions (x, y) of electrons as they emerge from the back of the sample linearly onto the camera which suppresses information about the angles of the electron trajectories. Focusing on the copper

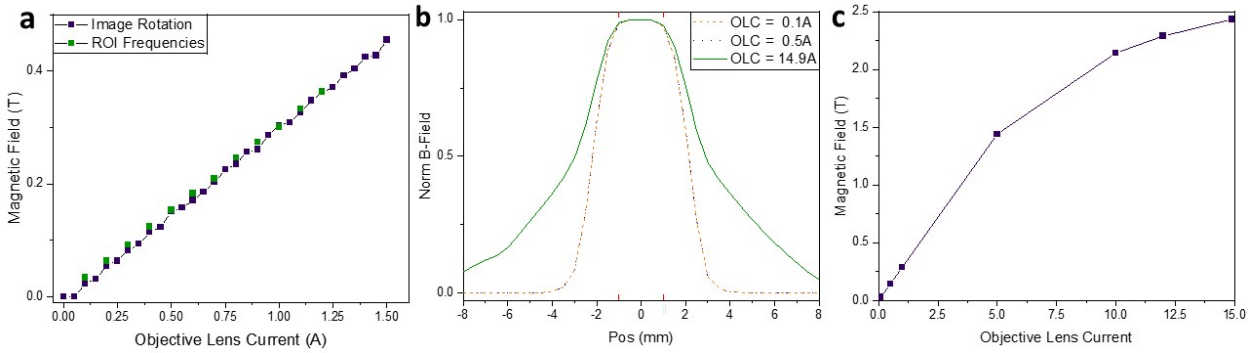

Figure 3.4: **a.** Magnetic field as a function of objective lens current (OLC) obtained from the image rotation measurements. **b.** Magnetic field as a function of position away from the sample plane (provided by Hitachi High-Tech). **c.** Magnetic field as a function of objective lens current at the sample position (provided by Hitachi High-Tech).

grid then produces an image of the copper grid with the lensing effect from the 3DEG unobserved. However, a defocused image results in a linear combination of the spatial and angular coordinates as the electrons emerge from the sample plane. To detect the space-charge lensing effect, we defocus the imaging system so that the resulting image is a linear combination of the spatial and angular coordinates of the electrons emerging from the back of the sample. Due to the deflection of the probe electrons by the transverse electric field of the electron gas, the electrons affected by the 3DEG have a post-sample crossover point that lies below the crossover point of the unaffected probe electrons ("below" indicates the direction along the propagation of the electrons). Thus by shifting the image plane nearer to the crossover plane of the objective lens, the lensing effect from the 3DEG can be observed (Fig. 3.5). It should be noted that in the low magnification mode of the Hitachi H9500 TEM, the objective lens current is conventionally kept constant and the first lens after the objective lens, called the first intermediate lens, acts as the focusing, or objective lens. The remaining lenses in the imaging system are then optimized for magnification and image quality and held constant while the intermediate lens focus was changed. In this way, by tuning the intermediate lens strength, it is possible to change the 3DEG lensing effect from barrel-type distortion (ILC = 0.65 A) to a pincushion-type distortion (ILC = 1.1 A) . This is schematically illustrated in Fig. 3.5a-c, where the 3DEG is depicted as a biconcave lens above the lower objective lens (OL) and for simplicity the four lenses in the imaging system are represented by an effective lens labeled IL.

Interestingly, the ROI difference trace for an intermediate lens strength of ∼0.95 A displays a double-peak feature that is different from the other traces. This is an effect of the time varying focal length of the 3DEG oscillating around the image plane, depicted in Fig. 3.6a-c. As the 3DEG contracts to a minimum radius the transverse electric field increases which produces a stronger diverging lens. By manipulating the intermediate lens current to set the image plane close to, but not at, the minimum focal length of the 3DEG the double-peak structure is produced. The to maxima observed in Fig. 3.5d for the 0.95

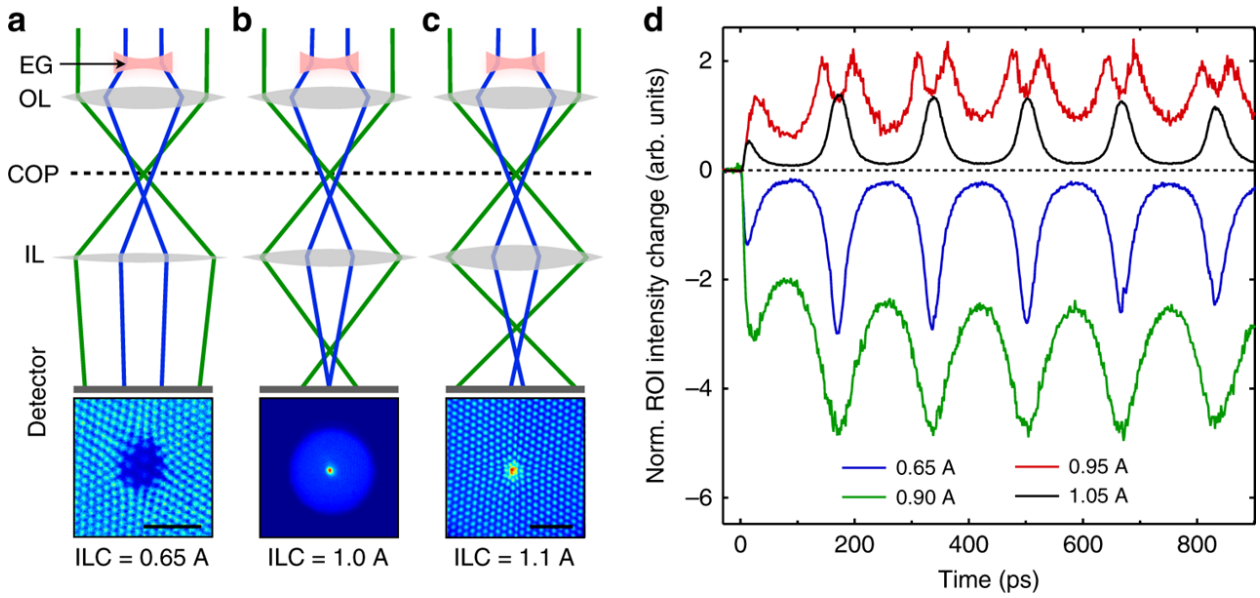

Figure 3.5: a-c. Image conditions at various intermediate lens currents (ILC): **a.** 0.65 A under focused image with barrel distortion, **b.** 0.95 A focused image with distortion due to electron gas, **c.** 1.1 A over focused image with pincushion distortion. The images correspond to the second peak seen in the ROI traces in **d**. Since the electron gas (EG, red) acts as a diverging lens, the probe electrons that pass through the gas have altered paths from unaffected probe electrons (green) that are then focused by the objective lens. COP = crossover plane. the scale bars are 50 μm (no scale bar in **b** since the grid is not visible). For simplicity the imaging system lenses is represented by an equivalent lens (IL) and the copper grid is not shown. Only the intermediate lens was changed for the data. **d.** ROI traces for various ILC settings (OL current at 0.7 A).

A ILC correspond to when the focal length of the 3DEG coincides with the image plane, as illustrated by Fig 3.6a & c. The 90°rotation observed in Fig. 3.6b & d, highlights the inversion that is know in optics to occur when the image plane pass through the focal point of a lens. Additionally, astigmatism of the 3DEG is observed when the crossover plane of the 3DEG is imaged. This astigmatism is due to the initial elliptical pump laser footprint on the sample due to the 37°angle between the copper grid surface and the optical path of the pump laser when the sample is tilted by 15°. Furthermore, this 15°tilt of the sample results in photoemitted electrons from the copper grid to have significant velocity component along the x-y plane, compared to an untilted sample. These two factors combined produces an elliptical 3DEG which has different focal lengths along the 3DEGs major and minor axes. The astigmatism of the 3DEG gas can be corrected by the microscopes stigmators at the cost of introducing astigmatism to the probe electrons unaffected by the 3DEG.

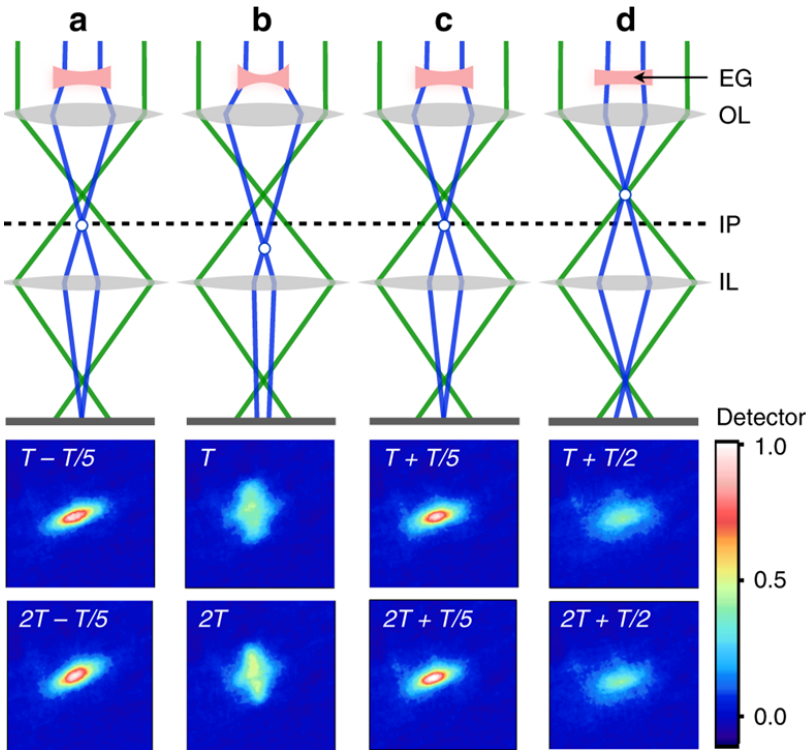

Figure 3.6: Schematic representing the time varying focal length of electron gas (EG) due to its cyclotron motion. The electron gas lens reaches its maximum strength in **b** and weakest in **d**, as seen by the crossover point (open circle) that moves below and above the image plane (IP). **a,c** represents the situation when the crossover point coincides with the IP of the intermediate lens, corresponding to local maxima in the ROI traces. The elliptical shape is due to the elliptical profile of the pump laser on the sample and the astigmatism of the electron-gas lens. OL = objective lens, T = cyclotron period.

3.5 Dependence on Sample Tilt

We investigated the dependence of the transient lensing dynamics on the relative angle between the Cu grid surface and the electron-optical axis (coinciding with the magnetic field vector). The initial velocity distribution of the electron gas peaks in the direction perpendicular to the Cu grid surface due to the photocreation process at ultrafast time scales[147,150,151,152]. The electron gas initially adopts a pancake shape aligned parallel to the Cu grid surface, with a lateral size of tens of μm and a thickness of only a fraction of a μm. Coulomb explosion during the first tens of ps thus leads to a profound expansion. The sample tilt thus adds a transverse velocity component relative to the magnetic field and therefore a larger Lorentz force compared to the situation where the velocity distribution peaks along the magnetic field direction (for no sample tilt). Fig. 3.7 shows the ROI traces

for three different sample tilts. The signal contrast (*i.e.* the difference in magnitude between the signal peak and trough), and therefore lensing strength, indeed increases as the sample tilt increases, in agreement with the increased Lorentz force in the transverse direction.

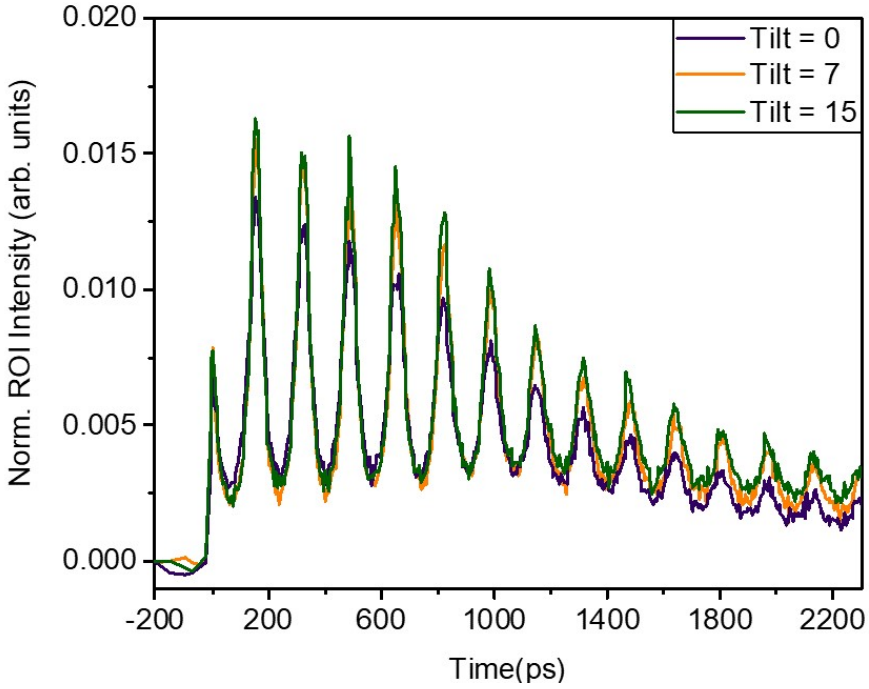

Figure 3.7: ROI traces as a function of sample tilt (angle in degrees between the sample surface and the electron-optical axis of the TEM).

3.6 Dependence on Laser Fluence

The laser pump fluence on the Cu grid can be used to tune the number of electrons and charge density in the electron cloud. We investigated the dependence of the ROI traces on laser pump power for experiments with a magnetic field (objective lens current set to 0.7 A) and without a magnetic field at the sample position (Fig. 3.8). The traces have been normalized to the signal magnitude of the first peak. Interestingly, in Fig. 3.8a, the lensing strength is highest for intermediate pump powers. This indicates that there are two counter-acting processes as the laser fluence is increased: (i) the increase in the absolute number of electrons in the cloud causing an increase in transverse electron field and therefore lensing strength; (ii) the enhancement of the Coulomb explosion[153,152] as the number of electrons in

the cloud increases. Fig. 3.8b shows that the decay of the first peak becomes faster as the number of electrons increases attesting an enhanced Coulomb repulsion within the cloud. The Coulomb explosion takes place in the first few/tens of ps s after photoexcitation when the electron bunch is still quite close to the grid. A large fraction of the electrons is thus re-absorbed by the Cu grid during this process leading to a decrease in lensing strength. The combination of these two effects leads to an optimum laser power for which the lensing strength is maximized (in this case ∼184 mW).

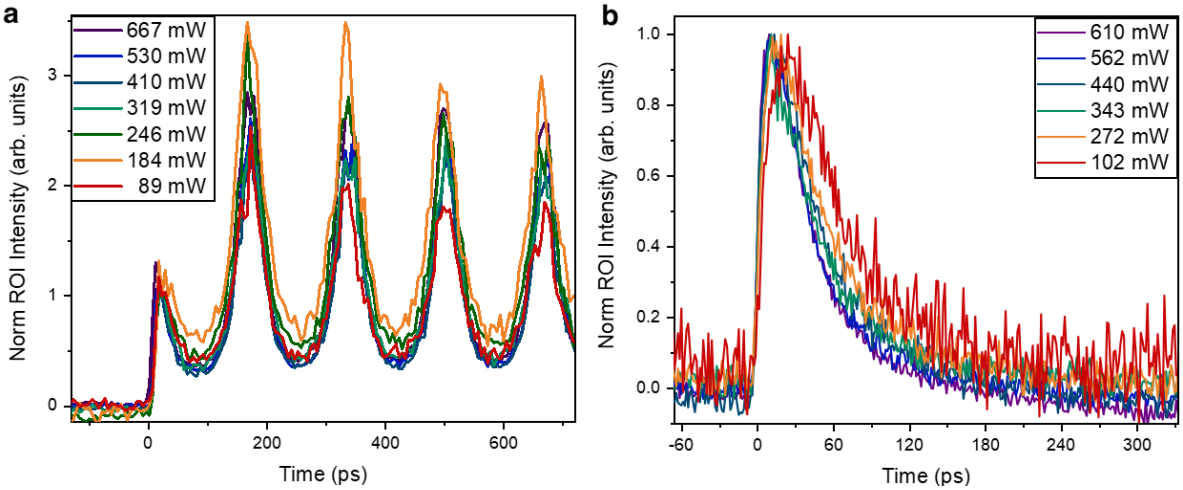

Figure 3.8: ROI traces as a function of laser power/fluence with, **a** (OLC = 0.7 A, and without, **b**, a magnetic field at the sample position.

3.7 Damage Tests

Damage measurements were performed to ensure the pump laser was operating within a regime that did not ablate the copper grid. Ablation of the copper grid could cause the creation of a neutral plasma and not an electron gas (so-called one-component plasma). This was done by exposing a region of the copper grid to the laser fluence that was used in a typical experiment and the assessing the damage by scanning electron microscopy (SEM). A 200 mesh grid was used due to its ease of indexing position compared to the 3000 mesh foil. Additionally, this smaller mesh grid has a bar width of 35 μm which, when oriented correctly in the TEM, allows for the minor axis of the pump laser to lay fully on the bar.

The SEM images, Fig. 3.9, of the grid show no damage from exposure to the pump laser (528 nm, 250 mW, 492 kHz) after ∼8 hours.

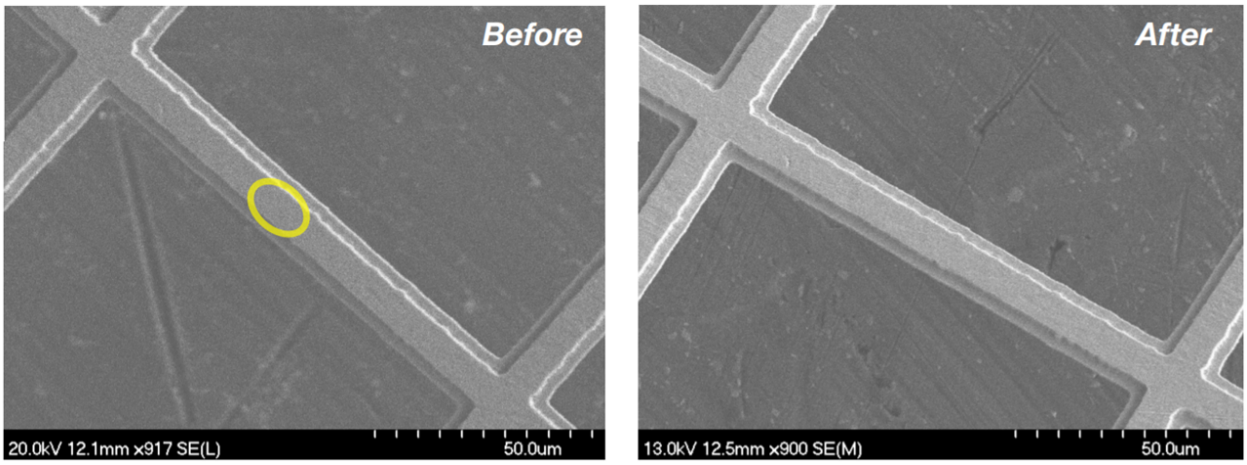

Figure 3.9: SEM images of a 200 mesh copper grid after exposure to the laser for ∼8 hours at 528 nm, 250 mW, 492 kHz. No signs of ablation were observed.

3.8 Analytical Model and Numerical Simulations

For completeness an analytical model and numerical simulations results will be briefly presented which describe and account for the trends seen in the experimental data. This is the work of Omid Zandi and the interested reader is directed to the our Nature Communications paper[93]. In the analytical model we assume no interactions between the electrons - the initial Coulomb explosion dynamics during the first tens of ps can therefore not be described with this model. To this extent numerical N-body simulations were conducted with an initially oblate, normally distributed electron gas. Together, the theory and simulations are able to semi-quantitatively explain the experimental features providing key insights into the dynamics of the photogenerated 3DEG.

The analytical model was derived using a cylindrical Gaussian charge distribution with transverse and axial (along z) standard deviations, σ_T and σ_z, respectively. Here, we do not take into account the small (15 degrees) tilt between the sample and the magnetic field direction. In the time regime >50 ps, after Coulomb explosion, we thus assume no force

acts along the electron-optical axis and the velocity profile should be more-or-less constant. This means that σ_z is expected to expand linearly. With these assumptions, the equations of motion for the Lorentz force, $F = q(v \otimes B)$, can be solved for the model charge distribution. This provides the following for the transverse radial standard deviation,

$$\sigma_{\mathrm{T}}(t) = \sqrt{2\left(\frac{\sigma_v}{\omega}\right)^2 (1 - \cos(\omega t)) + \sigma_r^2}, \tag{3.1}$$

where $\omega = \frac{eB}{2m_e}$ is the cyclotron angular frequency, σ_v is the transverse velocity spread, and σ_r is the minimum transverse radius of the electron gas. Note that for this equation the transverse radius oscillates between a minimum and maximum with the minimum occurring when $t = \frac{n2\pi}{\omega}$, where n is an positive integer. Then using Gauss law, $\bigtriangledown \cdot E = \frac{\rho}{\epsilon_\circ}$, where the charge density ρ is derived from the time-dependent radial standard deviations, the time varying focal length of the 3DEG is solved for, resulting in

$$f_{\mathrm{EG}}(t) = -\frac{2(2\pi)^{\frac{3}{2}} \epsilon_0 \gamma v_z^2 m_{\mathrm{e}}}{Ne^2} \sigma_{\mathrm{T}}^2, \tag{3.2}$$

where ϵ_0 is the vacuum permittivity, $\gamma = 1.6$ is the relativistic Lorentz factor, and $v_z = 2.3 \cdot 10^8$ m/s is the velocity of the 300 keV probing electrons, and N is the number of electrons in the 3DEG. This equation then requires the number of electrons in the 3DEG, the velocity spread of the 3DEG, and the minimum transverse radius to calculate the time varying focal length. Using the following form of the equation, $1/f_{\mathrm{EG}}(t) = Ae^{-t/\tau}/\sigma_{\mathrm{T}}^2(t)$, allows for fitting of the experimental data, with A containing the number of electrons in the 3DEG and other unknown parameters describing the 3DEG. The exponential phenomenologically describes the decay seen in the experiment. In combination with making assumptions about the post-sample lens system in the TEM, the minimum transverse size of the electron cloud, and considering that the electrons are emitted through a two-photon process that scales quadratically with photon intensity, we were able to get an order of magnitude estimate of the number of electrons in the cloud ($N \sim 10^5$), its transverse velocity spread ($\sigma_v =$

$4.91 \pm 0.01 \cdot 10^5$ m/s) and the focal length of the EG lens (oscillating between -0.5 and -5 m)[93].

As mentioned above, the analytical model does not account of the electron-electron interactions in the EG, which are expected to dominate the dynamics during the first tens of ps. Therefore, numerical simulations were conducted by solving the Lorentz Force, $F = q(E + v \otimes B)$ for the motion of each electron in an initially oblate distribution. Three simulations conditions were used in order to investigate the effect of the grid in the dynamics of the EG. These conditions were the 3DEG alone, the 3DEG with a grid present but without positive image charges, and with both the grid and image charge present. The presence of the grid and image charge in the grid are crucial to produce ROI difference traces similar to those seen in experiment and it explains why the first peak has a weaker lensing effect than the second peak in the ROI difference traces; at early timescales the 3DEG is thin along the optical axis and is effectively forming a plate capacitor with the positive image charge in the grid, resulting in a weak transverse electric field and therefore a weaker lensing effect. Furthermore, the simulations show that the 3DEG undergoes a rapid oblate-to-prolate shape change within ~80 ps. When the EG adopts a prolate, cigar-like shape at later times, the influence of the positive image charges is reduced and the lensing strength is increased.

3.9 Conclusions

Using our newly developed ultrafast electron microscope we investigated the ps-resolved dynamics of an electron gas that was created inside the TEM using short, intense laser pulses impinging on a Cu grid. The electron gas undergoes periodic breathing oscillations due to the static magnetic field from the objective lens and the Lorentz force acting in the transverse direction. These cyclotron oscillations lead to a pronounced lensing effect in the images of the Cu grid, the contrast of which can be tuned by changing the strength of lenses in the post-sample imaging system of the TEM. The gas undergoes a prompt Coulomb explosion during the first tens of ps, resulting in a pronounced oblate-to-prolate shape transformation

and a consequent increase in lensing strength. Analytical modeling in the absence of space-charge effects, and numerical N-body simulations, corroborate the interpretation of the data and provide a semi-quantitative estimate of the number of electrons in the cloud, its velocity spread, and the focal length of the electron-gas lens. These results pave the way for examining the dynamics of 2DEGs at the interface of, for example,GaAs/AlGaAs or other semiconducting materials[127].

CHAPTER 4: SPIN-STATE SWITICHING IN IRON-COBALT PRUSSIAN BLUE ANALOGUE NANOPARTICLES

4.1 Introduction

Prussian blue analogues (PBAs) are a class of porous polymer materials that have unique properties and applications, such as displaying spin-transitions, electrical conductance for battery electrode applications, biosensing and photomagnetism[154,155,156,157]. PBAs are bi-metallic polymer materials with cyanide bridging ligands between the metal atoms. In Fig. 4.1 the rubidium cobalt hexacyanoferrate (RbCoFe) unit cell is shown. The space group for most PBAs is $Pm\bar{3}m$, as seen in Fig. 4.1, with a unit cell vector on the order of 10$\pm$1Å, depending on the PBA atomic composition. The variable composition of the bi-metallic pairs (Co,Fe,Ni,Cr,Mn,V) and cation (K,Cs,Rb,Na) selection provides a wide array of unique properties[157]. Significant current research on PBAs is aimed at understanding and engineering photomagnets from PBA heterostructures[158,159,160,161]. Of specific interest are heterostructures of cobalt hexacyanoferrate (CoFe) and nickel hexacyanochromate (NiCr), which are photoactive and ferromagnetic, respectively[157,162].

Photomagnetism for CoFe/NiCr heterostructures works by modifying the magnetic properties of the NiCr layer via strain caused by the volume change in the CoFe lay from a photo induced spin transition. The spin transition observed in CoFe PBA materials is coupled to a charge transfer between the iron and cobalt atom, switching the cobalt atom to either a high or low spin state[164,165,166]. This was formally referred to as a charge transfer induced spin

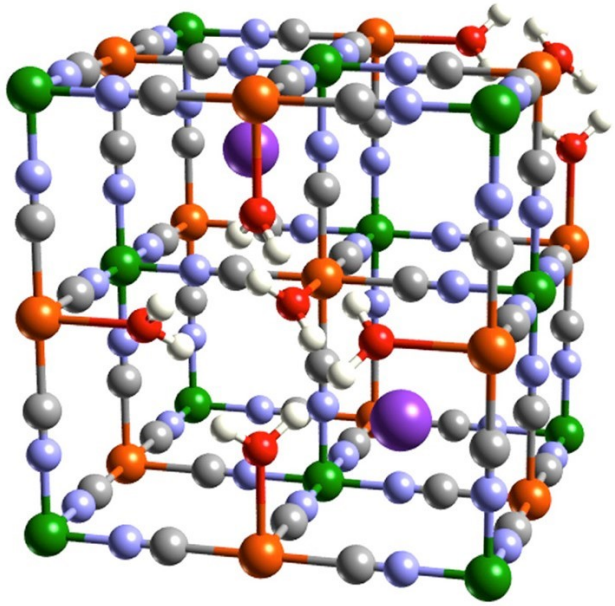

Figure 4.1: The crystal structure of a RbCo[Fe(CN)$_6$] (RbCoFe) Prussian blue analogue (PBA) with iron vacancies depicted. Rb, Co, Fe, N, and C atoms of the PBA are indicated in purple orange, green, gray, and light blue, respectively. The oxygen and hydrogen atoms from water molecules are indicated by red and white, respectively. Adapted with permission from [163]. Copyright 2018 American Chemical Society.

transition (CTIST) in the literature as the hypothesis was that the charge transfer between the iron and cobalt atoms in CoFe PBAs preceded and then induced the spin transition on the cobalt atom[167,168]. However, ultrafast X-ray and optical spectroscopies demonstrated that upon photoexcitation the low-spin to high-spin transition on the cobalt atom precedes the charge transfer between the iron and cobalt atoms[169]. The spin transition for CoFe PBAs is now referred to as charge transfer coupled spin transition (CTCST), however it is currently unknown if the photoexciatation mechanism pertains to the thermal process[170]. The volume change for CoFe is approximately a 10% between the high and low spin states which occurs at 250 K for RbCoFe[158,166,170]. Potassium nickel hexacyanochromate (KNiCr) PBAs are good candidates for preparing heterostructures with CoFe PBAs because the NiCr unit cell parameter is 10.385 Å which less than a 1% lattice mismatch fo the 10.3 Å unit cell parameter for CoFe in the low spin state[158,33]. The high spin unit cell parameter for CoFe is 9.6 Å which results in a large 8% lattice mismatch between the to PBA compounds resulting in strain that effects the magnetic properties of the NiCr PBA[158,159,171,33].

A recent publication by Miho Itoi *et. al.* demonstrated the ability of high resolution transmission electron microscopy (TEM) to provide spin state domain information with nanometer spatial resolution[166]. The research outlines an analysis procedure, when in combination with quality high resolution TEM images, provides detailed quantitative data on atomic column spacing in an image. However, this work only dealt with potassium cobalt hexacyanoferrate (KCoFe) PBA nanoparticles exploring the thermal CTCST process[166]. The DETEM at UIUC provides the experimental capability to explore how strain evolves in RbCoFe/KNiCr core/shell PBA particles in the low spin state after photoexcitation. There has already been powder X-ray diffraction work on these CoFe/NiCr core/shell particles looking at how both temperature and size of the core/shell constituents effect the photomagnetism of these particles via strain[158,159]. These ensemble experiments do not provide information on how the strain propagates through the core/shell particles as the photoexcited high spin CoFe core decays back to the low spin state, which occurs on the order of 10^3 seconds[158]. Additionally, time-resolved high-resolution TEM imaging would be able to elucidate the strain region conjectured to exist at the interface between CoFe and NiCr PBAs based on ensemble measurements[160]. The work presented in this chapter details steps taken to collect high resolution images of CoFe/NiCr core/shell particles at temperatures ranging between 125 and 165 K after photoexcitation to observe the evolution of strain within individual particles as the photoexcited high spin state decays back to the low spin state.

4.2 Materials and Methods

Prussian blue analogue core/shell nanoparticles were obtained in collaboration with Wanhong He from the group of Daniel Talham at the University of Florida. The RbCoFe/KNiCr core/shell nanoparticles were prepared using previously published procedures resulting in particle widths of 127±11 nanometers (nm), with the core precursors measuring 111±11 nm in width, with a chemical formula of $Rb_{0,16}Co[Fe(CN)_6]_{0,72}$ @ $(K_{0,37}Ni[Cr(CN)_6]_{0,79})_{0,18}$[158,159].

All TEM data collection used the DETEM instrument, described in Chapter 2, using the K2 detector in counting mode. Samples were prepared by bath sonication of the core/shell particles in an ethanol/water (30%/70%) mixture at a 1 mg to 10 mL ratio for 15 to 45 seconds depending on time needed to fully disperse particle. A pure carbon substrate on a 200 mesh copper grid was used for all work (Ted Pella Product # 01840). All electron dose rates were determined with the microscope in imaging mode. The Wehnelt bias was manually altered to obtain suitable dose rates while the microscope was set to spot size 3 and a magnification of 15k. The Wehnelt heating voltage was kept at 19 V for all experiments.

All diffraction data was azimuthally averaged in MATLAB with background correction done in Origin Pro using asymmetric least squares smoothing (ALS) to prepare a baseline for background subtraction. Diffraction peaks in the background subtracted data using the ALS baseline was fitted with a 1D Gaussian fit in MATLAB. High resolution image analysis was conducted in MATLAB using previously published procedures as an outline for data processing[166]. Images were first filtered in Fourier space using a spot mask on the fast Fourier transform (FFT) image. The FFT filtered image is segmented with a mask to remove the substrate and isolate the particle using the 'Image Segmenter' application in MATLAB on the original image. A minimum intensity threshold is set for the FFT filtered and segmented image to highlight atomic columns. The *imfindcircles()* MATLAB function is used to identify the atomic columns in the threshold image. The resulting circle positions obtained from the *imfindcircles()* MATLAB function are used to fit original image to a 2D elliptical Gaussian surface fit for accurate determination of atomic column positions. For each atomic column a radial distribution function is calculated using the euclidean distance formula against all other individual atomic column positions. The RDFs were filtered to include only viable distances of the Co-Fe or Ni-Cr bond used to then calculate the average bond length for each atomic column visualized in Fig. 4.3c and d. Drift analysis was conducted using a custom built MATLAB script using published elements of phase space cross-correlation[172,173]. This method works by finding the maximum value in a cross-correlation image that is the inverse

FFT of the product of the FFT of a image and complex conjugate FFT of a reference image. This is mathematically expressed as $CC = F^{-1}[F(u,v)^* G(u,v)]$, where $F(u,v)$ and $G(u,v)$ are the fast Fourier transforms of $f(x,y)$ and $g(x,y)$, respectively, and * is the complex conjugate. The maximum value represents the distance from image center that the two images have drifted with respect to each other. Image velocities were calculated using image acquisition time stamps provided by Gatan DigitalMicrograph® for each image collected.

4.3 Characterization of Thermoinic Damage Thresholds

Polymer compounds such as PBAs are easily damaged by the electron beam of a TEM[174,26,175 176,177,178]. Typically, for organic and polymer compounds ionization, also referred to as radiolysis, is the leading cause of electron beam damage inside an electron microscope[175,176,177]. Characterization of beam electron damage to organic or polymer samples is routinely done by measuring the decay in diffraction peak intensity or decay of a known peak or feature in the electron energy-loss spectra[175,177] as a function of accumulated dose. This analysis for organic and polymer samples can yield the quantitative measure referred to as characteristic dose, which is defined as the electron dose required to degrade the sample to 37% of the original intensity[175,26]. However, for the purposes of conducting pump/probe experiments in the DETEM at low electron dose rates, an electron dose rate that yields a 20% decrease or less in the 020 diffraction peak intensity is acceptable. The 020 diffraction planes represent the Co-Fe and Ni-Cr cyanide bridged bond distances, see Fig. 4.1, allowing this plane to correspond to the particles functionality, namely the photo-active CoFe core.

The electron beam damage analysis of the (020) diffraction peak, Fig. 4.2, provides insight into the appropriate electron dose rates for use with the CoFe/NiCr core/shell PBA nanoparticles. Unexpectedly, a particle contraction is observed as the (020) peak expands in reciprocal space with time, as clearly observed for the 0.577 and 0.438 $e^-/(\text{Å}^2 \cdot s)$ dose rates in Fig. 4.2a. Negative thermal expansion is not observed for these particles, ruling this out as an explanation of the observation[158,179,180]. This observation is interpreted as

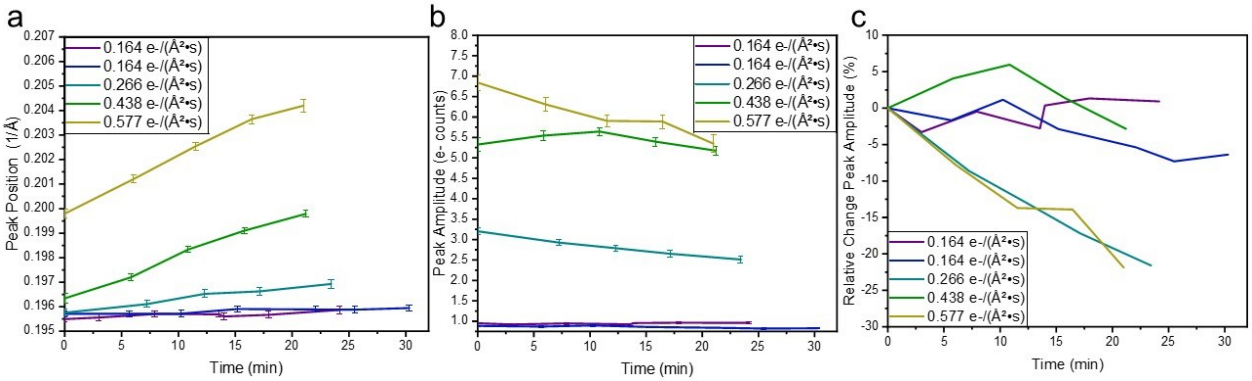

Figure 4.2: Electron beam damage analysis of the (020) diffraction peak for CoFe/NiCr core/shell PBA nanoparticles. a) Change of (020) peak position as a function of time for specified electron dose rates displaying particle contraction likely due to particle damage. b) (020) diffraction peak intensities as a function of time for specified electron dose rates. c) Relative percent change of the (020) diffraction peak intensities as a function of time displaying expected intensity decays as the particles degrade due to the electron beam causing a loss in crystallinity.

a degradation of the cyanide ligands bonding the metal atoms acting as scaffolding for the PBA particles. Loss of this scaffolding results in an inward collapse of the particle. However, the effect of this shifting peak position can be minimized as observed for the lowest electron dose rate of 0.164 $e^{-}/(\text{Å}^2 \cdot s)$ observed in Fig. 4.2a.

The trend for the (020) diffraction peak intensity does exhibit the expected response to electron dose rate. As described above degradation for polymer compounds in a TEM is best described by a characteristic dose, and is independent of electron dose rate. It would thus be expected to observe a slower decay in diffraction peak intensity for lower electron dose rates. This is indeed observed in Fig. 4.2b and c. One outlier however is the 0.438 $e^{-}/(\text{Å}^2 \cdot s)$ electron dose rate data set, as is best observed by the relative percent change displayed in Fig. 4.2c. There could be sample drifts introducing new particles into the selected area aperture or fluctuations in the electron current of the microscope. The 0.577 and 0.266 $e^{-}/(\text{Å}^2 \cdot s)$ dose rates indicate that there is a similar rate of decay when considering the relative percent change in peak intensity, Fig. 4.2c. If this trend is consistent for dose rates between these two values it would indicate other damage mechanisms are present besides ionization damage. This is because in polymer and organic compounds degradation is typically dependent on the total electron dose, not electron dose rate[174,175,177]. Additional data sets would be required

to substantiate this claim for electron dose rates in this range. The two $0.164 e^{-}/(\text{Å}^2 \cdot s)$ dose rate data sets provide convincing evidence that electron beam damage of the PBA nanoparticles can be effectively minimized for a 25 to 30 minute period considering both peak position and peak intensity, Fig. 4.2a and c, respectively.

4.4 High Resolution Imaging of CoFe/NiCr Core/Shell PBA Nanoparticles

High-resolution images were collected to determine the feasibility of resolving atomic columns with sub-nanometer resolution for low electron dose conditions on the K2 detector of the DETEM. Research has shown that high resolution TEM imaging of the PBA particles is effective for identifying low and high spin state domains and strain as a function of temperature[166]. The goal of this project is to extend this analysis to studies under light irradiation to investigate how the phase transition propagates in the particle. *Where does the high-spin phase nucleate? What is the role of crystal defects? And how do domain structure and strain differ between temperature-induced and light-induced spin state switching?* Research for CoFe/NiCr core/shell nanoparticles has shown that low-spin particles at temperatures of 125 to 145 K can be photoexcited into the high spin state and undergo slow decay back on the order of minutes back to low spin state[158]. Analysis providing information about atomic column spacing during this slow decay would provide valuable insight into the evolution of strain in the CoFe/NiCr core/shell PBA particles which is crucial for modifying the magnetic properties of the NiCr PBA shell. Experimental data of this sort would also provide insight into theoretical models used to describe spin transition phenomena[181,182,183,184]. The growth of the CoFe PBA particles results in the cube faces being of the {100} family of planes. As such, the 2D image of the 3D particles produces a lattice pattern corresponding to the 2D lattices used for common spin crossover theoretical models[185,186,158]. Also, for the CoFe/NiCr core/shell PBA particles this would provide valuable insight into the interfacial strain between the two materials that effect the magnetic properties of the NiCr PBA shell[160,159]. Towards this end, high resolution images with the standard single tilt sample

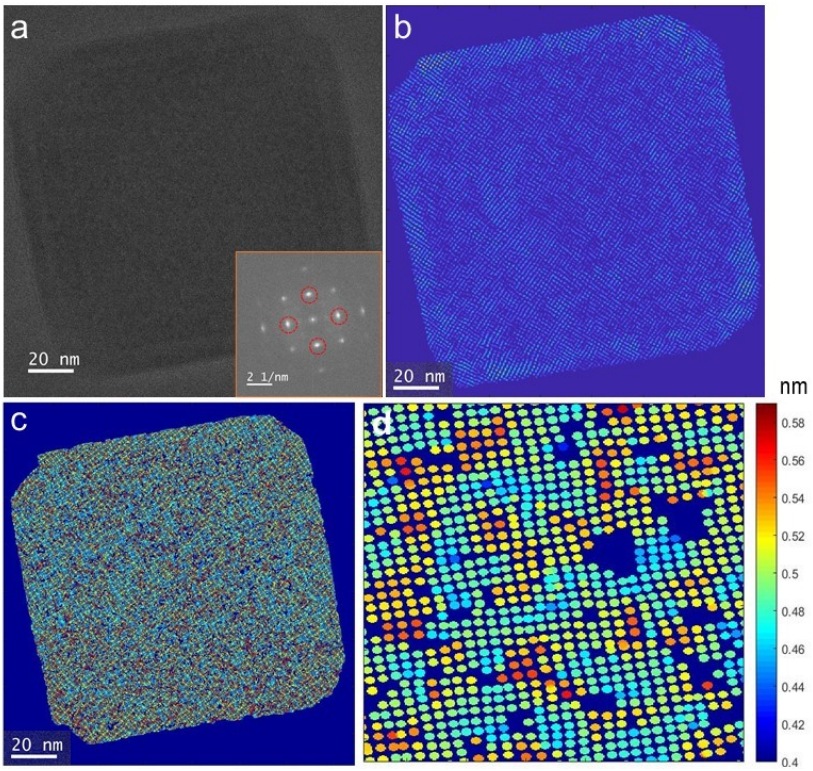

Figure 4.3: High resolution imaging and analysis of CoFe/NiCr core/shell PBA particles. a) High resolution image at an electron dose rate of 1.38 $e/(\text{Å}^2 \cdot s)$ on the K2 detector in counting mode. FFT insert on bottom right illustrates the image retains quality structural information for the image. The red circles highlight the FFT peaks that were spot masked producing the filtered image in b. b) FFT filtered, masked image illustrating the level of detail available at low dose imaging conditions on the K2 detector. c) Calculated image depicting atomic columns with color indicating the average distance to the columns 4 nearest neighbor positions. d) Zoomed in image of image c revealing the large amount of structural data available by analyzing the high resolution images of CoFe/NiCr core/shell particles at low dose conditions.

holder were taken on the K2 camera in counting mode for low electron dose rate conditions.

The image in Fig. 4.3a, was taken at an electron dose rate of 1.38 $e^-/(\text{Å}^2 \cdot s)$ with an exposure of 5 seconds. This is a much higher electron dose rate then used for characterizing the electron beam damage in the PBA particles, but was it necessary to achieve an 1.6 electrons per pixel for the 5 second exposure. Nevertheless, this low electron dose rate allowed for high quality images that are rich in structural data, evidenced by the inset FFT in Fig. 4.3a. Filtering the image in Fourier space by spot masking the 4 nearest neighbors produces, highlighted in red in FFT inset for Fig. 4.3a, results in quality filtered images, as displayed in Fig. 4.3b. Due to the low electron counts, the unmasked FFT filtered images produced structural elements outside of the particle when compared to the original

image. This was remedied by generating an image mask from the original image to eliminate any structure outside of the particle, producing the final FFT filtered image in Fig. 4.3b. Using the FFT filtered image the atomic columns are identified and fitted to a 2D elliptical Gaussian surface fit to accurately obtain the atomic column center positions. This allows the average bond distance to be calculated for each atomic column, with results plotted in Fig. 4.3c and d. The high level image, Fig. 4.3c, recreates the image well but the zoomed in image, Fig. 4.3d, reveals the extent of crystal defects and vacancies within the particle.

4.5 Temperature-Dependent Phase Transition Curves

With the goal of imaging CoFe PBA nanoparticles in the low-temperature phase, it was critical to first test that the low-temperature phase could be obtained. Decreasing and consequent increasing temperature scans wereconducted at a low electron dose rate of 0.164 $e^{-}/(\text{Å}^{2}\cdot s)$ and a temperature scan rate of 0.75 K/min. The (020), (311), and (222) diffraction peak positions for the decreasing temperature scan exhibit a clear reciprocal space expansion around 250 K corresponding to the CTCST transition of the CoFe core, observed in Fig. 4.4a, d, and e, respectively[158]. However, in the subsequent increasing temperature scans a reciprocal space contraction is observed at 150 K, best observed in the (222) diffraction peak data Fig. 4.4e. The resulting apparent hysteresis in the increasing and decreasing scans cannot be due to the CTCST phase transition, since the phase transition in the increasing branch should then be at higher temperature than the one in the decreasing branch. Instead, the likely cause for the apparent phase transition in the ascending branch is the deposition and sublimation of ice from the sample known to occur around 150 K. The amorphous ice ring, highlighted in Fig. 4.4f, occurs at the same position as the (022) diffraction peak position, which was therefore excluded from analysis. The ice in combination with the electron beam could cause damage to the CoFe/NiCr core/shell PBA particles. It has been shown that when frozen ionic liquids result in increased particle damage when exposed to the electron beam which suggest a similar damage mechanism could pertain to ice as well[166].

As a result, the increasing temperature scan should be disregarded, while considering the decreasing temperature scan valid down to 150 K.

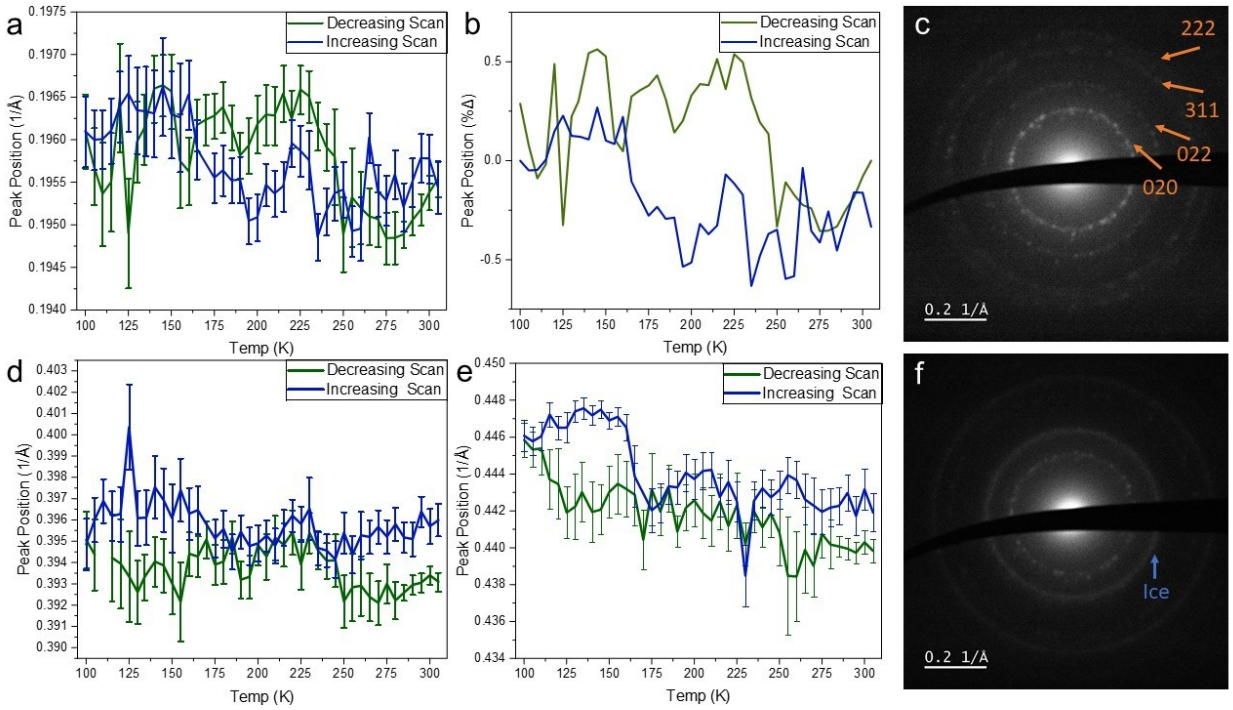

Figure 4.4: Temperature curve data for decreasing and subsequent increasing scans on CoFe/NiCr core/shell particles at a scan rate of 0.75 K/min. a) (020) diffraction peak position as a function of temperature for the decreasing (green) and then increasing (blue) temperature scans. b) Relative percent change for the (020) peak position as a function of temperature for the decreasing and subsequent increasing scan. c) Diffraction pattern at 200 K with diffraction rings highlighted in orange. d) (311) diffraction peak position as a function of time for the decreasing and increasing temperature scans. e) (222) diffraction peak positions as a function of time for the decreasing and increasing temperature scans. f) Diffraction pattern at 130 K for the increasing temperature scan displaying the presence of an amorphous diffraction ring due to the deposition of ice on the sample.

4.6 Drift Analysis for Using the Liquid Nitrogen Holder

While it was shown that high-resolution TEM imaging in the DETEM is possible with the standard Hitachi single tilt holder, it was not possible to obtain the same image quality with the Gatan liquid-nitrogen cooling holder at its base temperature of ∼80 K. This is due to significant lateral sample drift and vibrations along the y-axis of the sample, which resulted in the inability to replicate the image analysis shown in Fig. 4.3. While sample drift is not uncommon for TEM work, it is typically mitigated with time by waiting for the sample to

stabilize. Vibrations of the sample holder however can typically not be mitigated and result in a loss of resolution. Sample drift was assessed using phase-space cross-correlation and sample vibrations assessed by comparing image fast Fourier transforms (FFTs).

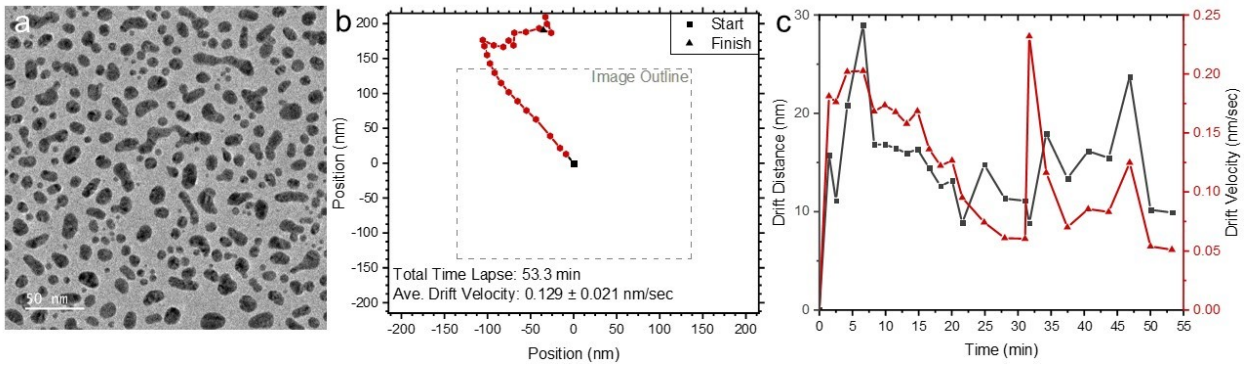

Figure 4.5: Drift Analysis of data set 4 for the Gatan Model 636 liquid nitrogen holder at room temperature with an empty liquid-nitrogen dewar. a) Imaged area on the gold nanoparticle sample used for drift analysis. b) Drift of the sample center, black square marker, over a 53.3 minute period with an average drift velocity of 0.129 nanometers ending at the black triangle marker. c) Drift distance (gray-left y-axis) and drift velocity (red-right y-axis) for each image taken over the 53.3 min period assessing sample drift for the Gatan liquid-nitrogen TEM holder.

An accurate and computationally inexpensive method for calculating sample drift in Fourier space, or phase space, was used[172,173]. Drift analysis was carried out as described in the Materials and Methods section on a gold sample with a reference image shown in Fig. 4.5a. In this manner the drift path can be plotted as done for data set 4 in table 4.1 in Fig. 4.5b. While Fig. 4.5 displays data set 4, the worst in terms of average drift velocity, this illustrates that over the course of an hour a particle originally in the center of the image would be well out of the imaging frame. When considering that a 5 second exposure was required for the high resolution TEM image in Fig. 4.3a, this amount of drift would not allow for image resolution to capture the atomic columns. Furthermore, it needs to be noted that this analysis was done with an empty liquid-nitrogen dewar (to avoid vibrations due to bubbling) and without electrical connections to the temperature controller, which is the holder's most stable state. It is possible that wait times in excess of an hour are needed, as the drift velocity appears to be decreasing over time as observed by the red trace in Fig. 4.5c. Thus, while not quantified for the experimental temperature scan condition, it is expected

that drift would be even worse than the data presented in table 4.1, making high-resolution imaging with sub-nanometer resolution while recording the phase transition as a function of temperature highly improbable.

In addition to the sample drift, it was observed that there was significant movement along the samples y-axis which was assessed to be vibrations. Movement and vibrations in the sample can be observed in real time by using the live FFT function in Gatan DigitalMicrograph®. This is best demonstrated by looking at the FFT images, Fig. 4.6c and d, for the standard gold sample in the standard single tilt holder and Gatan liquid-nitrogen holder in Fig. 4.6a and b, respectively. For the image of the gold standard sample in the single tilt holder, Fig. 4.6a, a qualitative inspection of the images FFT, Fig. 4.6c, shows a circular contrast transfer function as well as a diffraction like ring representing gold lattice spacing's. However, for image taken of the gold standard sample in the Gatan liquid-nitrogen holder, Fig. 4.6b, the FFT, Fig. 4.6d, shows a contrast transfer function that displays lobe like features. This is because when viewing the live FFT the contrast transfer function is fluctuating along the y-axis which is a sign of movement. The result of this when acquiring an image is the averaging of this effect which removes resolution along the y-axis. Additionally, the image in Fig. 4.6b was taken after the sample had been given an hour to stabilize. This observation of significant sample vibration in combination with the drift analysis discussed in the previous section renders acquiring high quality, high resolution images in the DETEM of the CoFe/NiCr core/shell particles with the Gatan liquid-nitrogen holder impossible.

Data Set	Drift Distance(nm)	Time Lapse (min)	Ave. Drift Velocity (nm/min)
1	11.4	12.8	0.79±0.89
2	66.1	30.2	2.33±1.34
3	225	75.1	2.98±1.60
4	361	53.3	7.73±3.23
5	239	70.7	4.67±1.98

Table 4.1: Drift analysis results for 5 data sets using a gold standard sample. The drift distance is calculated for the entire drift path. The time lapse is the time between the first and last image in the data set using the time stamp for the image taken in Gatan DigitalMirograph®. The average drift velocity is calculated based on all calculated drift velocities between each image.

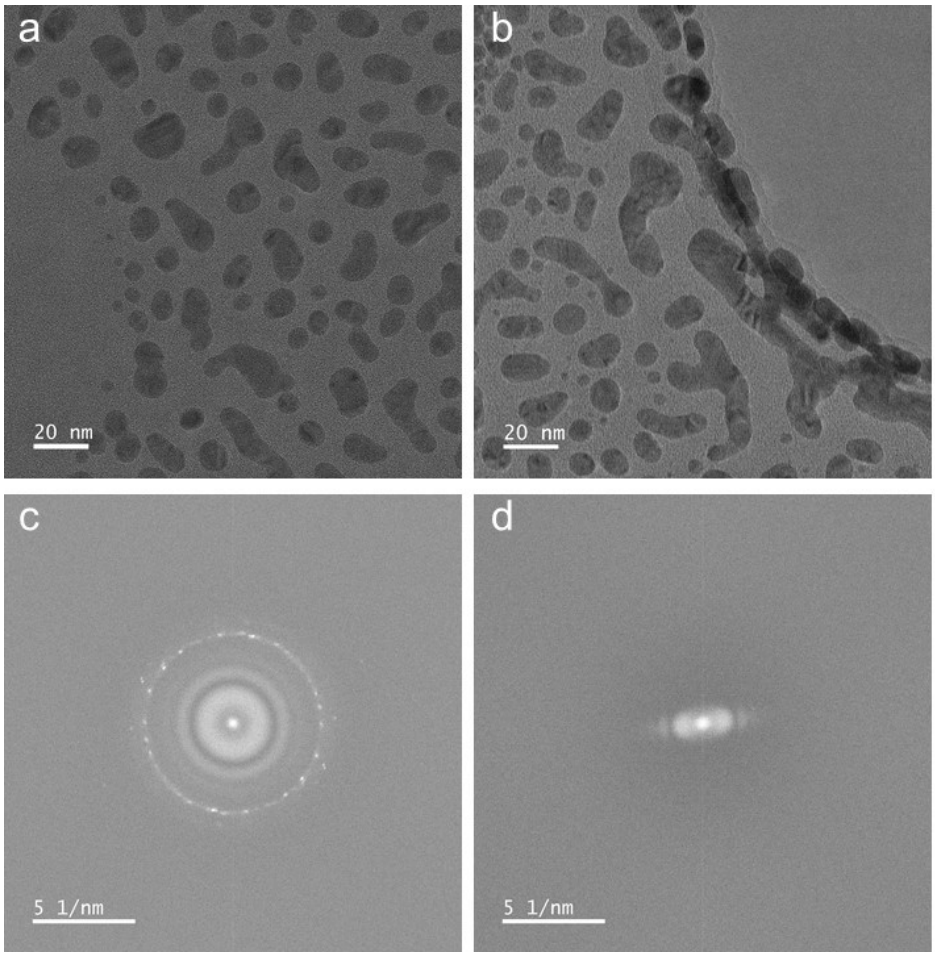

Figure 4.6: a and b) TEM images at the same magnification of gold nanoparticles in the standard Hitachi single tilt sample holder and the Gatan liquid-nitrogen sample holder, respectively. c and d) FFT patterns of the above images, respectively. Comparison of the two FFTs reveals a poor transform for the image taken in the Gatan liquid-nitrogen holder due to the vibrations of the Gatan liquid-nitrogen holder.

4.7 Conclusions

The work presented in this chapter represents the first steps towards the real-space imaging of light-induced changes in individual CoFe/NiCr core/shell PBA particles. Dose dependence studies revealed a dose rate that allows experiments up to ∼20 min before diffraction peak intensity has decayed by 20% at room temperature. High-resolution images of the particles were obtained that allowed a detailed analysis of low- and high-spin centers, strain, and defects. Temperature-dependent phase transition diffraction patterns were measured. While the high-to-low spin transition was observed around 250 K, the reverse low-to-high spin transition in the increasing temperature branch could not been seen due to the formation of

ice around 150 K. Finally, attempts to obtain high resolution images at low temperature, in the low-spin phase, failed due to technical issues such as drifts and vibrations of the liquid-nitrogen holder. Overall, the combination of sample damage and technical challenges posed by imaging individual nanoparticles at low temperature render the planned light-induced experiments particularly challenging.

CHAPTER 5: PHOTOINDUCED PHASE TRANSITIONS IN TRITITANIUM PENTOXIDE NANOPARTICLES

5.1 Introduction

Titanium oxides are a ubiquitous material in many areas of science, technology and medicine, ranging from research topics concerning green synthesis, memristive technology, gas sensing, supra-molecular chemistry, clinical dentistry, cancer theranostics, and photocatalytic degradation of organic pollutants[187,188,189,190,191,192,193,194,195,196,197,198,199,200,201,202,203,204,205,206,207]. Titanium suboxides, also referred to as Magneli phases, are titanium oxides with mixed titanium oxidation states first reported in the scientific literature in the 1950's and 60's[208,209,210]. These materials garner interests for novel properties such as metal-insulator transitions, metal-semiconductor transitions, and superconductivity seen in the Ti_3O_5 and Ti_4O_7 Magneli phases[211,212,213,214,215]. This chapter focuses on trititanium pentoxide, Ti_3O_5, and presents work towards studying the photoinduced phase transition between the β and λ phases in Ti_3O_5 nanoparticles using the Illinois DETEM.

Trititanium pentoxide, Ti_3O_5, is a unique material displaying polymorphism with five phases (α, β, λ, γ, and δ). The γ and δ phases of Ti_3O_5 are a high and low temperature pair with a phase transition at 240 K that is attained by reducing TiO_2-rutile particles[216,217]. These two phases are monoclinic structures that undergo an isostructural, metal-to-insulator phase transition from the $I2/c$ space group to the $P2/a$ space group[216,217,215,218]. The high temperature α phase and room temperature β phase of Ti_3O_5 display a metal-to-

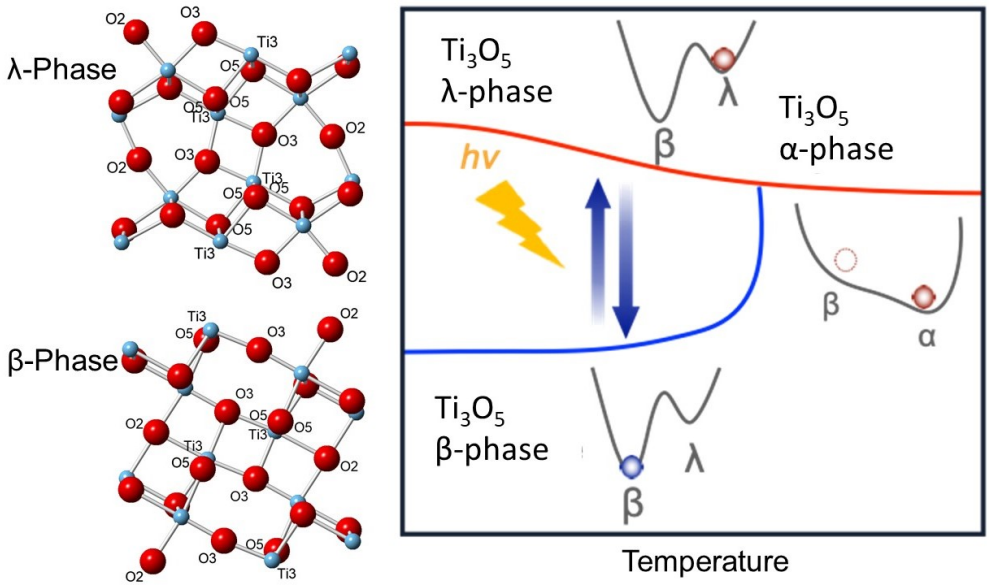

Figure 5.1: Illustration of the phase diagram depicting the high temperature α-phase, low temperature β-phase, and metastable λ-phase. Below the high temperature α-phase transition at 500 K, the reversible photoinduced phase transition between nanoscale β- and λ-phase particles is achieved.

semiconductor phase transition at 500 K[219,218], Fig. 5.1. The high temperature, metallic α phase is an orthorhombic crystal structure with the $Cmcm$ space group, and the low temperature, semiconductor β phase is a monoclinic crystal of $C2/m$ space group[218,219,215]. The fifth λ phase was first published in the literature in 2010 by Ohkoshi *et. al.* in *Nature Chemistry* demonstrating that this new metastable phase could be accessed by a photoinduced phase transition for nanoscale particles, illustrated in Fig. 5.1[219]. The λ phase, also a monoclinic crystal structure, $C2/m$, was shown to only exist for Ti_3O_5 nanoparticles (not in the bulk) and the β-to-λ phase transition displays a hysteresis between 450 and 500 K[219,220]. Importantly, the 2010 Ohkoshi *et. al.* paper established fluence thresholds at 532 nm for the persistent photoinduced phase transition at room temperature, *i.e.* a transition between the two phases with effectively infinitely long life times. For a persistent β-to-λ-phase transition a fluence between 270 mJ/cm^2 and 690 mJ/cm^2 was observed[219]. For fluences >690 mJ/cm^2, a persistent λ-to-β photoinduced phase transition was observed, and below 270 mJ/cm^2 no persistent change was observed with X-ray diffraction[219]. Static studies where conducted providing evidence that not only can the persistent β-to-λ-phase

change be reversibly triggered by light but also by pressure and electrical current[221]. These highlighted properties make β-phase Ti_3O_5 attractive for optical memory applications.

In order to understand the dynamics of the β-to-λ photoinduced phase transition, pump/probe experiments with optical and X-ray probes have been conducted[222,223,32]. These experiment were conducted below the reported 270 mJ/cm^2 fluence such that a transient (short-lived) and partial photoinduced phase transition was observed rather than a persistent and complete transition. Ultrafast diffuse reflectance spectroscopy, conducted by Asahara *et. al.*, revealed that for β-phase particles the λ phase can be transiently photoexcited below this threshold[222]. Additionally, this work hypothesized that the pump pulse generates λ-phase seed domains that will then grow and annihilate because the laser energy is insufficient to produce a complete phase transition of the sample. This work was followed by time resolved X-ray experiments conducted by Tasca *et. al.* illuminating that there is an observable structural component on similar time scales to that observed in the ultrafast diffuse reflectance data[223]. However, the temporal resolution for these X-ray data was on the order of 10 μs making the study blind to structural dynamics occurring on faster time scales that could elucidate how the phase transition propagates in the material. This was addressed by Mariette *et. al.* by conducting ultrafast diffraction experiment at X-ray free electron laser and synchrotron facilities capable of fs and ps temporal resolution, respectively[32]. These studies revealed that photoinduced structural changes occur within 5 ps with a linear increase in β-to-λ fraction to approximately 16 ps. This new insight led the authors to propose a strain wave pathway as responsible for inducing the β-to-λ transition upon photo-excitation. While these studies provide pivotal insights into the dynamics of the photoinduced phase transition, these experiments were conducted on pellet samples formed with a high pressure press. These ensemble studies however are blind to single particle dynamics and possible introduce inter-particle effects into the observed photoinduced phase transition dynamics. These ensemble experiments reveal that the sample only undergoes a partial photoinduced phase transition with many particle remaining unaffected.

Open questions and planned experiments

Based on the above background the following questions remain, which are the focus of this project: *Do single particles undergo a partial phase transition with both λ- and β-phases co-existing or do single nanoparticles switch fully while others do not switch at all? Does the photoinduced phase transition nucleate at the particle surface then propagate via the a strain wave throughout the particle? What is the role of grain boundaries?* Private discussions with Prof. Ohkoshi indicated that the fluence thresholds increase for a persistent photoinduced phase transition as particle size decreases. *Can we demonstrate/confirm this relationship between fluence and particle size at the single-particle level?* Additionally, *do dynamics for single particles at the nanoscale occur at similar time scales as for ensemble measurements?*

The Illinois DETEM offers unique capabilities to study photoinduced phase transitions at the single-nanoparticle level. In particular, it provides a means to investigate threshold fluences and transient dynamics as a function of particle size. To answer the above-posed questions, we plan the following experiments:

- Static TEM characterization of individual Ti_3O_5 nanoparticles, identification of their phase and indexing the diffraction pattern.
- Single-shot before/after experiments: the sample is irradiated with a single fs pump laser pulse with a well-defined energy that could, if sufficiently intense, induce a persistent transition between the λ- and β-phases. Images taken before and after the laser exposure are recorded and compared as a function of laser fluence and particle size.
- Time-resolved stroboscopic ns and fs diffraction experiments on nanoparticle ensembles. These experiments will be used to benchmark our work with previously published work on nanoparticle pellet samples[32].
- Time-resolved stroboscopic ns diffraction experiments at the single nanoparticle level. These will allow us to investigate variations in the switching efficiency as a function of

particle size, shape, and morphology. The changes in peak position and intensity of specific diffraction peaks will be compared to the theoretical change expected based on the know β- and λ-phase crystal structures. Again, the dependence of the dynamics on laser fluence and particle size will be studied. We will start with ns-resolved experiments to establish signal levels and life times, before we move to fs-resolved experiments.

- Depending on the success of the single-particle diffraction experiments, time-resolved bright- and dark-field imaging experiments will be performed. These would allow to directly visualize the propagation of the λ-phase and study the origin of the phase nucleation and the role of defects.

- The experiments can be extended by ultrafast convergent-beam or nanoprobe diffraction on individual nanoparticles to quantify the variations in strain as a function of time delay.

- Static and time-resolved EELS experiments at the O- and Ti-K-edge would enable insights into the concurrent dynamics of the electronic structure (density of states) across the semiconductor (β)-to-metal λ phase transition.

5.2 Materials and Methods

Four samples of Ti_3O_5 nanoparticles were provided by the groups of Hiroko Tokoro from the University of Tskuba and Shin-ichi Ohkoshi from the University of Tokyo. They were made using different synthesis procedures to achieve a variety of sizes and relative composition ratios between the β and λ phases. In Sample 1 (S1) the average particle size is $\sim$2 μm and are aggregates of precursor TiO_2-anatase particles with an approximate 25 nm diameter using the flake form synthesis previously reported[219]. In Sample 2 (S2) the average particle size is $\sim$5 μm and are aggregates of precursor TiO_2-rutile particles with a size of 200 nm using a synthesis previously reported[224]. In Sample 3 (S3), 30 nm Ti_3O_5 nanoparticles were synthesized in a SiO_2 matrix using an unpublished procedure for an ongoing project in the Tokoro/Ohkoshi group. In Sample 4 (S4), Ti_3O_5 nanoparticles with an average size of 200 nm

were prepared by ball-milling the S1 sample for >3 days producing a nearly 100% β-phase sample. The β:λ-phase ratios for these samples were determined using X-ray diffraction and the respective β:λ percent ratios are: 23:77 (S1), 88:12 (S2), 88:12 (S3), 100:0 (S4). TEM samples were prepared by bath sonication in a 70:30 H_2O:EtOH solution before drop casting 9 uL of the solution on the grid. Static measurements used a pure carbon substrate on a 200 mesh copper grid (Ted Pella Product # 01840). Single-shot experiments were conducted on few-layer hexagonal boron nitride (h-BN) substrates on a 2000 mesh gold grid fabricated using a previously reported procedure[225]. Time-resolved measurements utilized an ultrathin carbon film with a lacy carbon support on a 400 mesh copper grid (Ted Pella product # 01824). The pump-probe time resolved experiments were conducted at a repetition rate 4.9 kHz with a calculated pump fluence of 50 mJ/cm^2 at 740 nm and a UV probe power of 11 mW measured at 10 kHz at 266 nm.

Diffraction patterns were fitted in MATLAB® using a two dimensional elliptical Gaussian fit. Static and time-resolved data were processed and analyzed in MATLAB® and compared to previously published crystallographic data, shown in table 5.1[32,219]. The SingleCrystal® software was used to index single-particle diffraction patterns using the stereographic projection. In brief, stereographic projections are built placing the unit cell at the center of a sphere. The *hkl* vectors, which are normal to the lattice plane, are then depicted as points on the spehere's surface, and the *hkl* plane is depicted by a circle known as a great circle or trace of that *hkl* vector. A practical example is seen in Fig. 5.2f, where the stereographic projection is looking down the [192] zone axis. The blue, red, and green lines are the traces of the (1-14), (5-12), and (40-2) *hkl* reflections, respectively. This practical example illustrates that the intersections for the traces of *hkl* reflections is the zone axis of the diffraction pattern. Thus, by plotting the traces of identified *hkl* reflections and then orienting the diffraction pattern using the stereographic projection provides an effective procedure for indexing diffraction patterns.

Ti_3O_5 Phase	β Phase	λ Phase
Crystal System	Monoclinic	Monoclinic
Space Group	C 2/m	C 2/m
a(Å)	9.7568	9.8261
b(Å)	3.8008	3.7894
c(Å)	9.4389	9.9694
$\beta(^\circ)$	91.547	91.258
V (Å^3)	349.898	371.118

Table 5.1: Crystal structure data used for identifying the Ti_3O_5 nanoparticle phases[32]

5.3 Static Sample Characterization

Static TEM imaging and diffraction on samples S1-S4 was done to determine the optimal sample and to estimate the feasibility for time-resolved experiments. An optimal sample for time-resolved diffraction experiments is one with many well-defined single nanoparticles, with a known phase, and that are thin enough to transmit enough electrons and to be able to neglect multiple scattering. Promising particles were selected and their phase (β or λ) and relative orientation with respect to the probe electron beam (*i.e.* the zone axis) were determined using the stereographic projection feature in the SingleCrystal® software.

Sample S1

Representative bright-field images and a single-particle diffraction pattern for sample S1 are shown in Fig. 5.2. In Fig. 5.2a, distinct rod, triangular and spherical particle morphologies are observed. While the spherical and rod-shaped particles have a thickness of ∼100 nm which is ideal for time-resolved TEM, the triangular particles have dimensions of ∼200 nm (lateral and thickness). Indeed, only for the spherical and rod-shaped particles we were able to observe lattice fringes in high-resolution bright-field images, as shown in Fig. 5.2b for a spherical particle. Analysis of the corresponding fast Fourier transform (FFT), Fig. 5.2c, reveals that the β-phase (421) plane is present for this particle. The diffraction pattern in Fig. 5.2d, for a rod-shaped particle in the inset, can be indexed for the [1 9 2] zone axis of the λ phase. This pattern matches well the simulated diffraction pattern shown in Fig.

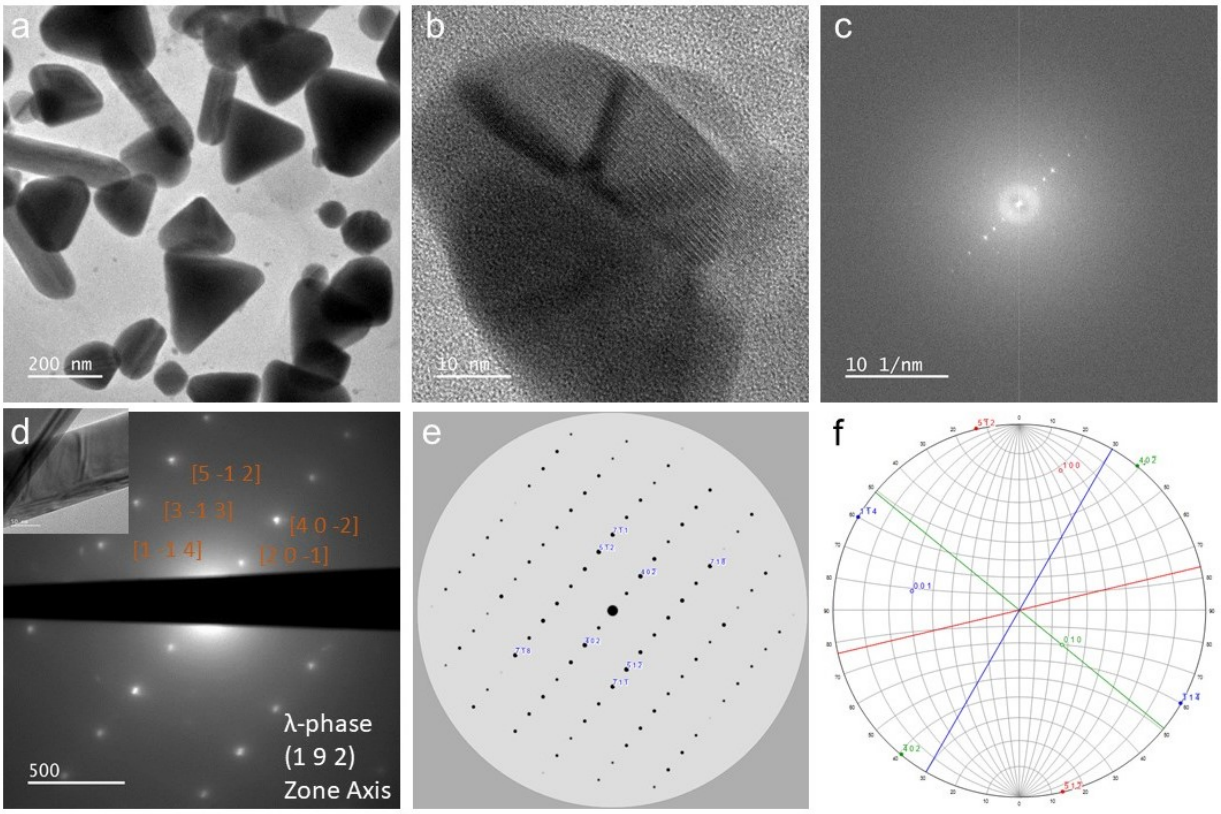

Figure 5.2: Static data for S1 particles. a) Low magnification TEM image highlighting the diverse particle morphologies in S1. b) High resolution images of a spherical particle with atomic resolution of lattice fringes. c) Fast Fourier transform (FFT) of spherical particle in b with analysis revealing β-phase spacing for the (421) reflection. d) Indexed diffraction pattern (corresponding particle in the inset image) for the [192] zone axis. e) Calculated diffraction pattern, oriented similarly to the experimental diffraction pattern in d. f) Stereographic projection of the [192] zone axis with the traces for the (1-14), (5-12), and (40-2) reflection plotted in blue, red, and green, respectively.

5.2e. The zone axis was identified by orienting the stereographic projection to look down the intersection of the (5 -1 2) and (4 0 -2) traces, shown in red and green respectively in Fig. 5.2f. Overall, the particles in S1 have good crystallinity and thickness. However, 77% of the material in S1 is in the λ phase which is unfavorable for single-particle experiments probing the transient photoinduced β-to-λ phase transition.

Sample S2

The morphologies for particles in S2 are best described as flake-like with representative particles shown in Fig. 5.3a and d. The thickness of these particles evinces electron

transparency, however high resolution imaging shown in Fig. 5.3b shows that the particles contain multiple crystalline domains. The low magnification images in Fig. 5.3a and d display features such as bending contours, thickness fringes, and specifically in Fig. 5.3d where visible faults that indicate the particles are composed of multiple crystalline domains. The low crystallinity of these particles is likely due to the TiO_2-rutile nanoparticle precursors fusing but not annealing to restructure as a single crystal. Additionally, the starting precursor particle size for the synthesis could affect this outcome as well. The analysis of the image FFT, Fig. 5.3c, for the high resolution image in 5.3b, reveals multiple crystal domains. This is evident due to the presence of six peaks in the FFT pattern with a spacing of 3.3049

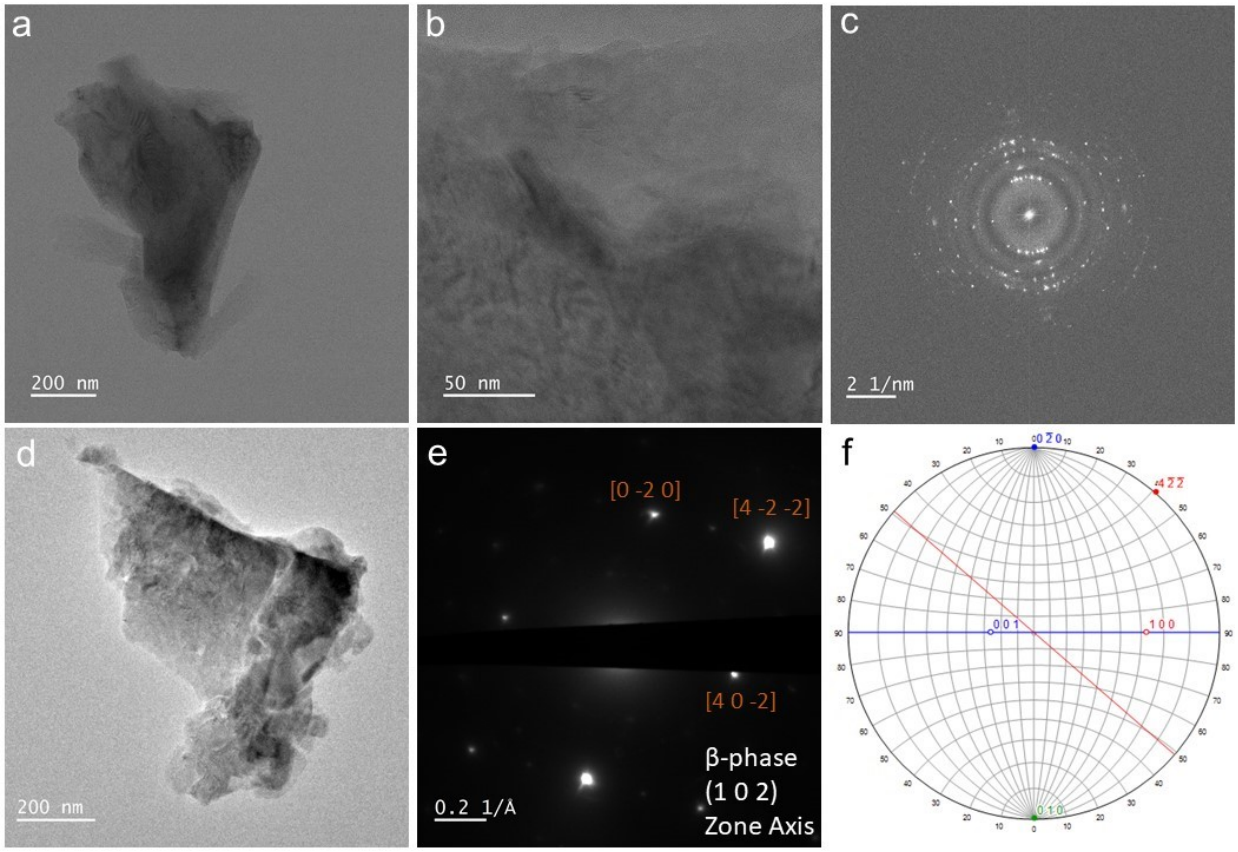

Figure 5.3: Static data for S2 particles. a and d) Images highlighting typical flake like particles observed in S2. b and c) High resolution image and accompanying FFT, respectively, for the flake particle in a, revealing atomic resolution of the lattice fringes best evidenced by the FFT. d and e) Image and diffraction pair with diffraction peaks for the β-phase [102] zone axis labeled. The diffraction pattern is taken from a smaller section of the particle to obtain a pattern that could be indexed. f) Stereographic projection of the [102] zone axis with the traces of the (0-20) and (4-2-2) reflections plotted in blue and red, respectively.

Å (0.30258 $Å^{-1}$) matching the β-phase (111) *hkl* plane, with the angles between these six peaks ranging from 6 to 20 degrees. The smallest possible angle between peaks of the (111) *hkl* family of planes is ∼58 degrees, indicating that these small angles represent multiple offset crystalline domains. The diffraction data in Fig. 5.3e, taken from a section of the particle in Fig. 5.3d, could be indexed for an orientation close to the β-phase [1 0 2] zone axis. However, this pattern represents only a section of the particle, as the whole particle diffraction pattern produced a pattern akin the FFT pattern in Fig. 5.3c. For time-resolved TEM experiments the low level of crystallinity would severely complicate the single-particle data analysis and interpretation making this sample unfavorable, despite containing a large fraction of β-phase particles with desirable thicknesses.

Sample S3

Sample S3 was synthesized with the goal of obtaining smaller/thinner particles that are better for time-resolved TEM experiments. However, in order to produce nanoparticles that do not fuse or anneal during the reduction of TiO_2 precursors it was necessary to encase the particles in an amorphous SiO_2 matrix. This produces high-quality particles with an average size of 30 nm. Low magnification images reveal various obloid shaped particles as seen in Fig. 5.4a and d. The contrast between the Ti_3O_5 nanoparticles and the SiO_2 matrix is poor at this magnification making it necessary to use an objective aperture, as in Fig. 5.4a, or operate slightly out of focus to increase contrast. In Fig. 5.4d the bright Fresnel fringe around the SiO_2 matrix indicates an overfocused condition. High resolution imaging of the particles reveal highly crystalline particles as observed in Fig. 5.4b. Analysis of the corresponding FFT in Fig. 5.4c reveals spacings matching the (001) and (202) *hkl* planes for the β phase. A consequence of the SiO_2 matrix is a significant scattering background that is apparent in the ensemble diffraction pattern, Fig. 5.4e, and the subsequent azimuthal averaging of that diffraction pattern, Fig. 5.4f. This amorphous background and the fact that SiO_2 absorbs in the visible/UV adds complications for ultrafast TEM studies on this

sample.

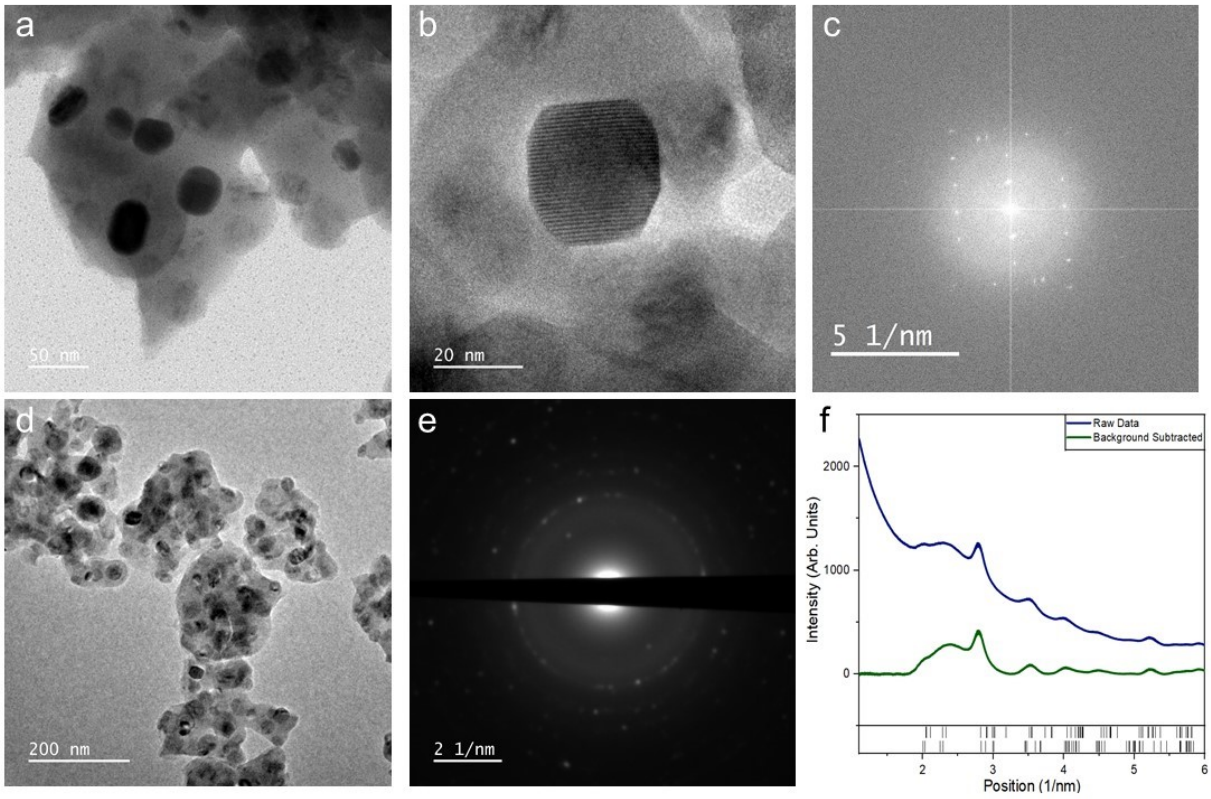

Figure 5.4: Static data for S3 particles. a and d) Low magnification images of S3 particles revealing the spherical shape of the particles encased in a SiO_2 matrix. b and c) High resolution image and accompanying FFT revealing the highly crystalline nature of S3 particles, with analysis of the FFT indicating the particle is in the β phase. e and f) Ensemble diffraction pattern and azimuthal average of the pattern with stick profile for the β (top) and λ (bottom) plotted below.

Sample S4

The particles in sample S4 were synthesized using the same procedure as for sample S1, but in order to increase the fraction of β-phase particles, the sample was subsequently ball-milled for more than 3 days, as higher pressures have been shown to favor the β-phase[226,221]. Different particle morphologies are obtained as seen in Fig. 5.5 a-d. While the particles are large they are electron transparent as best evinced by the image in Fig. 5.5d, where the holes in the lacey carbon substrate can be seen through the particle. Additionally, the particle in Fig. 5.5d, yields a single particle diffraction pattern in Fig. 5.5e and identified to be the β-phase [141] zone axis with selected peaks labeled. The calculated diffraction pattern,

Fig. 5.5f, from the SingleCrystal® software, with the experimental region highlighted by a purple dashed line. With its almost 100% β-phase composition and the ability to obtain high-quality single-particle diffraction patters, this sample thus provides an ideal material for time-resolved TEM experiments. All experiments described in the following were performed on this sample.

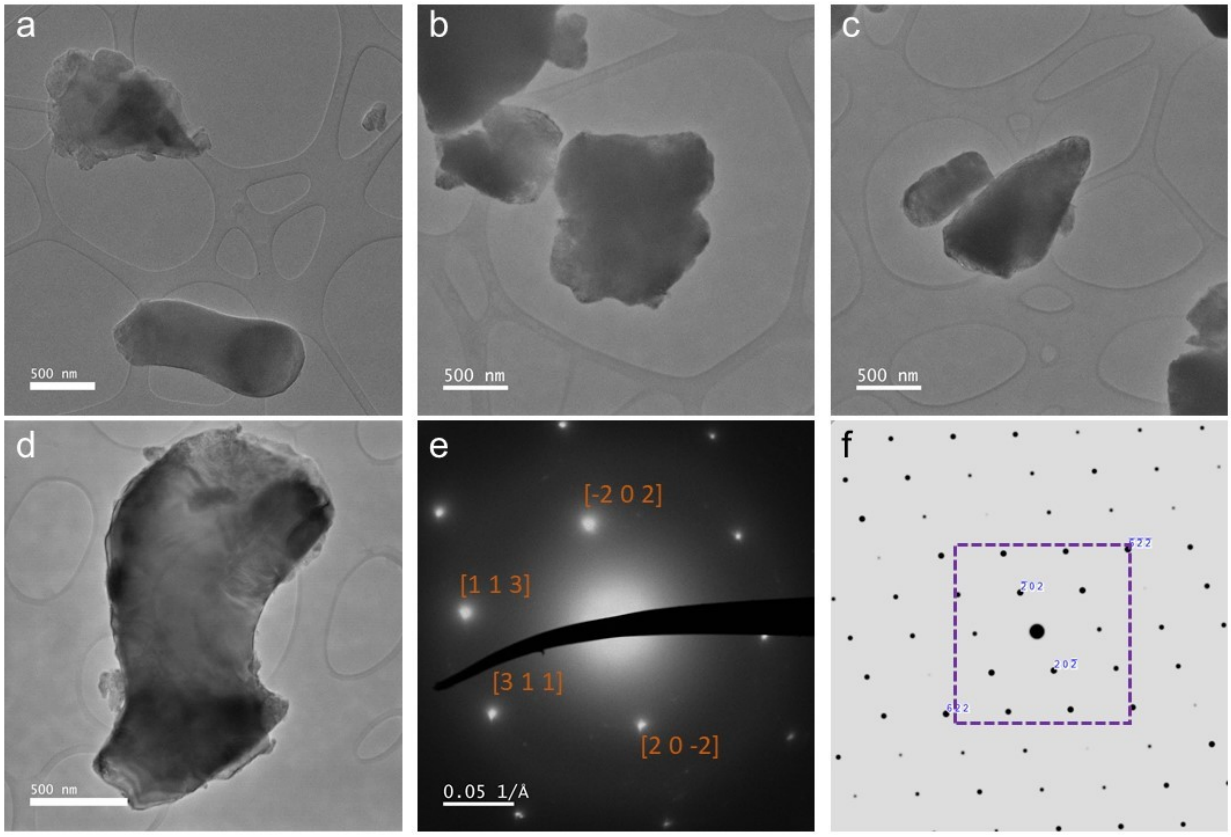

Figure 5.5: Static TEM data for S4 particles. a-c) Images of typical particles in S4. d and e) Image and accompanying diffraction pattern with labeled peaks for the β-phase [141] zone axis. f) Calculated [141] zone axis with purple region of interest highlighting the approximate region of the diffraction pattern in e.

5.4 Femtosecond Single-Shot Experiments

With the goal of achieving a persistent β-to-λ photoinduced phase transition at the single-nanoparticle level inside the TEM, we exposed suitable particles to single shots of ~250 fs, 740 nm laser pulses and compared the images and diffraction patterns before and after the exposure. The 740 nm light, with a photon energy of ~1.68 eV which is well over the 0.14

eV band gap of the semiconductor β-phase, will excite valance band electron and initiate the photoinduced phase transition. The maximum achievable fluence in these experiments was 77 mJ/cm^2 due to instrument restrictions. At such high laser fluences, the TEM substrate film and grid may heat up and break during the experiment, which was observed for SiN and SiO TEM substrates. To improve this, we employed hexagonal boron nitride (h-BN) substrates. h-BN has a large bandgap ~4 eV (309 nm) material and therefore it does not absorb visible/IR light[227]. Its lower electrical conductivity, however, can cause charging effects in the TEM.

The diffraction patterns taken before and after the single fs laser pulse (740 nm, 77 mJ/cm^2) are shown in Figs. 5.6a and b, respectively. The particle is oriented along the

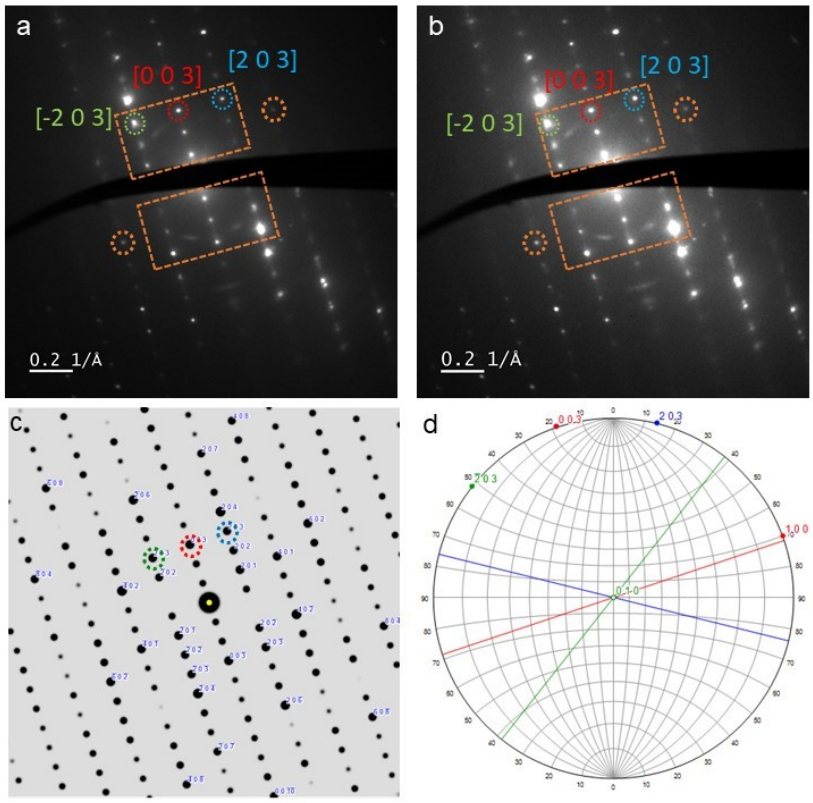

Figure 5.6: a) and b) Diffraction patterns before and after a single fs laser pulse at 740 nm with a fluence of 77 mJ/cm^2, respectively. These patterns are taken on the [010] zone axis with the (-203), (003), and (203) *hkl* reflections highlighted in green, red, and blue, respectively. The orange boxes and circles highlight reflections that were fitted for identifying the zone axis and for analyzing results of the single-shot experiment. c) and d) Calculated single crystal diffraction pattern and stereographic projection for the beta phase [010] zone axis with the (-203),(003), and (203) *hkl* reflections highlighted in green, red, and blue, respectively.

β-phase [010] zone axis analyzed by fitting the diffraction peaks highlighted within the orange region of interest boxes. The *hkl* reflection spacings were obtained by calculating the euclidean distance between Friedel pairs and dividing by a factor of two. The calculated diffraction pattern for the [010] zone axis is shown in Fig. 5.6c, matchs the experimental data. Absolute errors between the experimental and calculated data are typically below one percent with only the (001) reflection having an error of -1.37% between the fitted and calculated reflection spacing, shown in the calculated spacing column of Table 5.2. The percent change in lattice spacing for the before and after diffraction patterns evidence at best a +0.42% change for the (201) reflection (fourth column of table 5.2), but a percent change of -1.89% is expected for a full β-to-λ photoinduced phase transition for this reflection. The average change in peak separation is +0.14% for all reflections. While heat from the laser pulse has been dissipated by the time that the diffraction pattern was recorded (second/minutes after the laser shot), the increase in peak separation (*i.e.* a contraction in the real-space lattice) may be caused by a slight annealing of the material as a result of the laser excitation and consequent heating. Slight variations in the particle's orientation may be responsible for the changes in peak amplitude (fifth column of Table 5.2). In any case, the expected and observed changes in peak separation do not match and we conclude that we did not induce the persistent β-to-λ-phase transition in this experiment. This is probably due to the laser fluence being too low. In a previous study on Ti_3O_5 pellets with micron-sized particles a fluence of 270 mJ/cm^2 at 532 nm was necessary to induce the persistent β-to-λ photoinduced phase transition. Clearly, we show here that 77 mJ/cm^2 is not sufficient to induce such a transition in individual β-phase nanoparticles with $\sim$100-500 nm diameter.

5.5 Stroboscopic Ns-Resolved Diffraction Experiments

Since inducing the persistent phase transition using single laser shots was not possible, we turned to stroboscopic experiments in which the λ-phase is induced transiently and only fractionally on the bulk scale. We started with ns-resolved experiments since this allowed us

hkl Reflection	Exp. Spacing $Å^{-1}$	Calc. Spacing (%Err to Fit) $Å^{-1}$	%Δ Spacing (Expected)	%Δ Peak Amplitude
203	0.38007±4.3e-05	0.38296 (-0.75)	0.04 (-4.15)	-6.39 and -1.22
003	0.31558±2.8e-05	0.31795 (-0.74)	0.05 (-5.33)	-7.12 and -14.02
$\bar{2}03$	0.37336±2.0e-05	0.37366 (-0.08)	0.03 (-3.75)	13.91 and 2.96
202	0.29611±6.4e-05	0.29887 (-0.92)	0.03 (-3.31)	-5.50 and 1.09
002	0.21062±3.7e-05	0.21197 (-0.64)	0.31 (-5.34)	14.48 and -14.67
$\bar{2}02$	0.29166±6.8e-05	0.29092 (0.25)	0.10 (-2.83)	-4.20 and 22.92
001	0.10453±6.4e-05	0.10598 (-1.37)	0.19 (-5.33)	-1.43 and 5.45
201	0.23304±1.8e-04	0.23336 (-0.14)	0.42 (-1.89)	-3.05 and -10.76
$40\bar{2}$	0.46085±6.6e-05	0.45655 (0.94)	0.10 (-1.44)	16.85 and -1.38

Table 5.2: First column: Fitted reflections from Fig. 5.6a and b. Second column: experimental spacings from Fig. 5.6a and b. Third column: calculated spacings with percent error to the experimental ones in parenthesis. Fourth column: percent change in reflection changes after a single fs laser pulse (expected percent change for full β-to-λ transition in parenthesis). Fifth column: percent change in fitted peak amplitude of the Friedel pair peaks after a single fs laser pulse.

to work at lower repetition rates (5-100 kHz) as opposed to fs pump-probe experiments that must be carried out at much higher repetition rates (100-500 kHz) to obtain sufficient S/N. Low repetition rates are important in order to allow the sample to relax back to the ground state between subsequent pump pulses.

In the first data set (DS1), the (110) and (220) *hkl* reflections for the β phase are clearly identified as shown in the diffraction pattern, Fig. 5.7a. Additionally, the $(3\bar{1}\bar{5})$ and $(\bar{4}05)$ reflections were identified, which orients this diffraction pattern to the [1.18 1.$\bar{1}$8 0.94] zone axis. These reflections were fitted, but the fittings were unreliable as these peaks were lost during the course of the experiment. The diffraction patterns in Fig. 5.7 d-f highlight in blue peaks lost during the experiment, and the peaks in red appeared. This is indicative of the particle rotating on the substrate, and a ∼0.5 degrees rotation can result in changing the Bragg condition such that no diffraction is seen anymore. Additionally, the peak that appeared is not a reflection for the β-phase [1.18 1.$\bar{1}$8 0.94] zone axis further indicating that in addition to thermal effects there is spatial drift/rotation in the experiment. The (110) and (220) Friedel pairs however remain during the experiment and are well fitted, with the (220) peak shown as an example in Fig. 5.7c. The time-resolved scan of peak position in reciprocal space versus time delay is shown in Fig. 5.7b. A momentum space

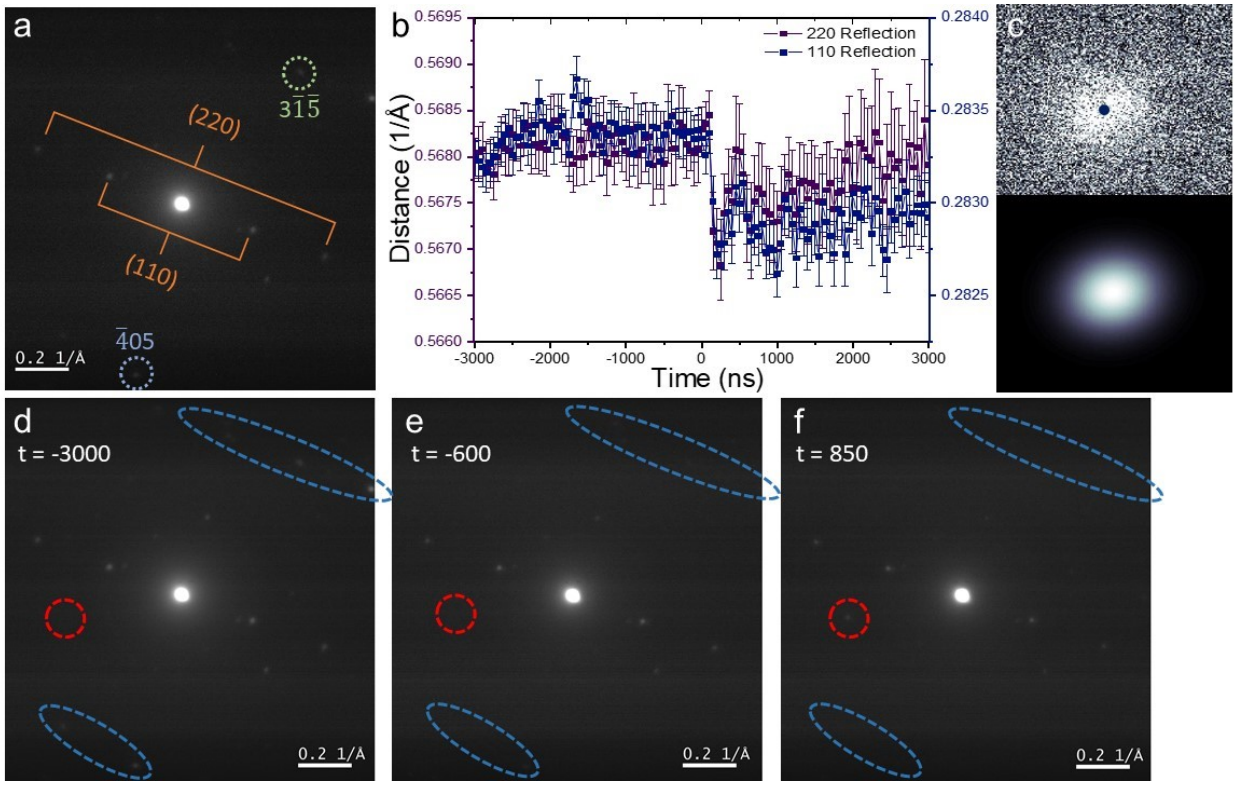

Figure 5.7: Data Set 1 (DS1): a) Diffraction pattern highlighting the (110) and (220) Friedel pairs (in orange) that were fitted. b) Time traces for the (110) Friedel pair, right axis, and (220) Friedel pair, left axis, showing a reciprocal-space contraction. c) Experimental and fitted (220) peak on the top and bottom, respectively. The plotted point on the top experimental data represents the center point from fitting. The error for the fitted point is too small to be visualized at this scale. d-e) Diffraction patterns at -3000, -600, and 850 ns highlighting diffraction peaks that are gained (red) and lost (blue) during time scans.

contraction of ∼0.15% for both (110) and (220) reflections is observed promptly at time zero, with a slight decay over the time scale of a few μs. Notably, a momentum-space *expansion* (*i.e.* real-space contraction) of ∼0.17% is expected for the (110) reflection based on the calculated momentum transfer values for the β and λ phases (0.28238 Å^{-1} and 0.28285 Å^{-1}, respectively). We conclude that the transient changes we see in the diffraction pattern are not due to the phase transition. As discussed below, they may be assigned to a transient heating effect resulting from laser excitation of the particles and the substrate.

For the second data set (DS2), Fig. 5.8, it was not possible to index the diffraction pattern and determine the phase and zone axis unambiguously. However, there was one peak that did show a clear photoinduced response. As in the first data set, diffraction peaks were lost or diminished in intensity such that they could not be fitted against the background signal

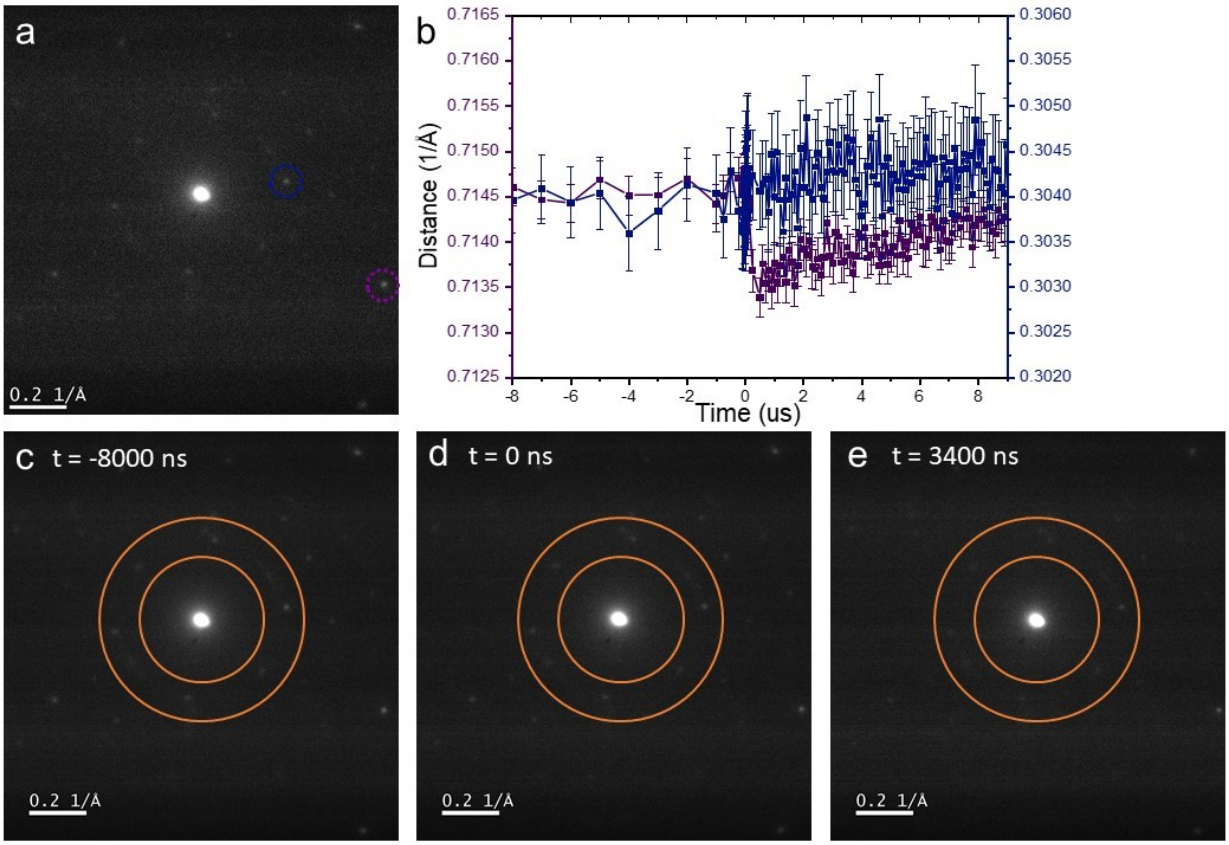

Figure 5.8: Data Set 2 (DS2): a) Diffraction pattern highlighting the plotted peaks in the time trace in b) (matched colors in both panels). c-e) Diffraction patterns at -8000, 0, 3400 ns showing peaks between the rings that have lost intensity hindering the fitting analysis.

over the course of the experiment. This is best depicted by the diffraction spots highlighted between the orange rings in Fig. 5.8 c-e. Of the four peaks that retained a suitable signal to noise ratio such that the time traces could be considered viable, only one peak produced a photoinduced signal. The observed loss of signal could be due to particle movement as the particle or substrate thermally equilibrates. Additionally, experimental drifts, such as spatial sample drift or probe laser overlap drift on the photocathode could also explain these losses in peak intensities. The peak with a photoresponse, plotted in purple in Fig. 5.8b, displays a $\sim$0.15% momentum space contraction and is plotted with a peak that did not produce a photoresponse. This contraction is also similar in magnitude to the momentum space contraction observed for the first data set. This peak, however, is unidentified with a *hkl* spacing of $0.7145 \pm 0.0005 \text{Å}^{-1}$ which does not match any β or λ-phase reflections. The

inability to match the peak demonstrates a calibration error for this data set. However, comparing this peak to the closest possible reflections reveals that the smallest expected change is ∼1.7%. While this is the only peak in the data set (of four peaks total), the similar percentage contraction as in DS1 indicates that they have the same origin.

The combined analysis for these two time-resolved data sets points to the fact that the photoinduced signals are photothermal in nature. However, it is possible that a β to λ photoinduced phase transition occurred and decayed faster than observable for the temporal resolution of the nanosecond probe. A delayed and long lived thermal response was observed in previous ultrafast diffraction experiments[32]. This is plausible as the temperature change for DS1 is on the order of ∼85K. This increase is not unlikely given the small band gap for the β phase, 0.14 eV[219]. Furthermore, qualitatively the signal is observed to be decaying on the order of tens of microseconds, with initial fittings corroborating this observations. This would allow for increasing the repetition rate to 10kHz providing better signal to noise.

5.6 Conclusions and Next Steps

While the single-particle photoinduced phase transition in Ti_3O_5 nanoparticles was not observed, the work in this chapter lays the groundwork for future experiments in this project. We showed that with proper calibration the single-particle diffraction patterns can be unambiguously indexed and the phase can be identified as being β- or λ-phase, an important prerequisite for quantitative time-resolved electron diffraction studies. The single-shot and stroboscopic pump/probe experiments demonstrated laser-induced changes to the diffraction pattern, such as peak shifts and intensity loss, however, the observed changes do not correspond to expected changes for a β-to-λ-phase photoinduced phase transition. The diffraction peak positions *increased* for the single-shot experiments, albeit only by a small percentage. However, the stroboscopic experiments revealed a ∼-0.15% *decrease* for diffraction peak positions and a decay time of several μs. The consistent decrease in diffraction peak position indicates a transient thermal expansion of the lattice and a ∼85 K

temperature jump upon photoexcitation (relative to room temperature). The laser fluence employed in these experiments is comparable to the fluences used for diffuse reflectance spectroscopy that first observed the transition[223,222] and time-resolved XRD experiments in which β-to-λ phase change efficiencies of up to 30% were observed[32]. *Why, then, do we not see the transition in our experiments?* There may be several reasons for these discrepancies: (a) The laser fluence threshold to induce the phase transition inherently depends on the environment of the sample. Single nanoparticles on a substrate in vacuum pose a very different environment than, for example, particles pressed in a pellet. Surface effects and differences in heat conductivity may play a role. (b) The number of particles we studied is too sparse. The single-particle time-resolved diffraction experiments in the DETEM are time consuming and sample drifts and damage prohibit very long exposures. (c) The life time of the photoinduced λ-phase may have been too short to be resolved in a ns-resolved experiment and/or the signal from the phase transition is overwhelmed by the changes in peak spacing due to heating (thermal expansion).

To investigate these discrepancies and better understand the origin of the laser induced dynamics at the single-particle level, we propose the following experiments: (1) Acquire more statistics by analyzing many more individual particles at different relative orientations and with different sizes. So far, most diffraction peaks studied were of the ($hk0$) family. However, the changes in the c-axis are expected to be largest ($\sim$6%[32]). Particles with more suitable orientation need to be identified prior to starting a time-resolved experiment. (2) The particle coverage and dispersion on transparent h-BN substrates need to be improved. Not all studied particles demonstrated laser-induced diffraction signals, which rises the question of the role of the environment for each nanoparticle. *Does the position of a particle on the substrate relative to the substrate edges or frame play a role? Do interparticle interactions play a role for densely packed particles?* (3) Acquire better statistics by integrating longer and scan out to longer time delay to see the entire signal decay back to zero. The possibility to perform experiments at higher repetition rate should be explored. (4) Experiments so far have been

done using fs laser excitation pulses. The question arises whether the dynamics depends on the laser pulse length. Experiments with ns laser pulses need to be performed that could lead to larger (thermal and/or electronic) phase transition conversion efficiencies that potentially exceed the changes due to thermal expansion. (5) Temperature-dependent static studies could help in calibrating the expected changes in lattice spacing upon heating. (6) Ns- and fs-resolved diffraction on particle ensemble are expected to be more straightforward than single-particle studies. They can help benchmarking our conditions with previously reported studies.

CHAPTER 6: CONCLUSIONS AND FUTURE OUTLOOK

In this dissertation we presented the development and characterization of a unique dynamic environmental transmission electron microscope (DETEM) capable of capturing snapshots of evolving nanostructures and soft materials undergoing temperature-, gas-, voltage-, or light-induced chemical transformations on time scales ranging from femtoseconds-milliseconds. We have demonstrated the successful use of the new instrument by a comprehensive study of the picosecond-resolved dynamics of a three-dimensional electron gas in vacuum subject to a static magnetic field. These experiments inspire a plethora of future studies in the fields of two-dimensional electron gases, plasma physics, and the development of bright electron and X-ray sources. Furthermore, we demonstrated the ability to collect high-resolution images using a direct-electron detection camera and operate the DETEM at low dose rates that are necessary to image sensitive materials such as the Prussian blue analogue materials presented herein. Improvements in the stability of the sample holders are necessary to enable single-nanoparticle high-resolution imaging under light irradiation as a function of temperature. Finally, single-nanoparticle electron diffraction studies of trititanium pentoxide (Ti_3O_5) revealed a reciprocal-space contraction upon photoexcitation on the nanosecond time scale indicating the dominating role of thermal expansion of the crystal lattice as a result of sample and substrate heating. While an electronic photoinduced β-to-λ phase transition was not evidenced in these studies, our work represents an important step towards future pump-probe studies, which will be continued in collaboration with the groups of Florian Banhart and Maciej Lorenc in France. In summary, the newly developed ultrafast

”chemiscope" has already showed exciting results and is now poised to enable discoveries in heterogeneous (photo)catalysis, polymer physics, nanoparticle self-assembly, electrochemical charge transport, biofunctional interfaces, and ultrafast materials switching, to name a few.

REFERENCES

(1) Knoll, M.; Ruska, E. *Zeitschrift Physik* **1932**, *78*, 318–339.

(2) Rose, H. H. *Science and Technology of Advanced Materials* **2008**, *9*, 014107.

(3) Tanaka, N. *Science and Technology of Advanced Materials* **2008**, *9*, 014111.

(4) Levin, B. D. A. *Journal of Physics: Materials* **2021**, *4*, 042005.

(5) Koifman, N.; Talmon, Y. *Pharmaceutics* **2021**, *13*.

(6) Wu, F.; Yao, N. *Nano Energy* **2015**, *13*, 735–756.

(7) Wu, F.; Yao, N. *Nano Energy* **2015**, *11*, 196–210.

(8) Lian, J.; Wang, L. M.; Sun, K.; Ewing, R. C. *Microsc Res Tech* **2009**, *72*, 165–81.

(9) Chee, S. W.; Lunkenbein, T.; Schlogl, R.; Cuenya, B. R. *J Phys Condens Matter* **2021**, *33*, 153001.

(10) Van der Wal, L. I.; Turner, S. J.; Zečević, J. *Catalysis Science and Technology* **2021**, *11*, 3634–3658.

(11) Borrajo-Pelaez, R.; Hedström, P. *Critical Reviews in Solid State and Materials Sciences* **2017**, *43*, 455–474.

(12) Ye, F.; Xu, M.; Dai, S.; Tieu, P.; Ren, X.; Pan, X. *Catalysts* **2020**, *10*, 779.

(13) Vahidi, H.; Syed, K.; Guo, H.; Wang, X.; Wardini, J. L.; Martinez, J.; Bowman, W. J. *Crystals* **2021**, *11*, 878.

(14) Velamoor, S.; Mitchell, A.; Bostina, M.; Harland, D. *Exp Dermatol* **2021**, DOI: `10.1111/exd.14439`.

(15) Bullock, H. A.; Goldsmith, C. S.; Miller, S. E. *Kidney Int* **2021**, *99*, 824–827.

(16) Kuijper, M.; van Hoften, G.; Janssen, B.; Geurink, R.; De Carlo, S.; Vos, M.; van Duinen, G.; van Haeringen, B.; Storms, M. *J Struct Biol* **2015**, *192*, 179–87.

(17) Song, J.; Allen, C. S.; Gao, S.; Huang, C.; Sawada, H.; Pan, X.; Warner, J.; Wang, P.; Kirkland, A. I. *Sci Rep* **2019**, *9*, 3919.

(18) Takaba, K.; Maki-Yonekura, S.; Inoue, S.; Hasegawa, T.; Yonekura, K. *Front Mol Biosci* **2020**, *7*, 612226.

(19) Williams, D.; Carter, C., *Transmission Electron Microscopy: A Textbook for Materials Science*; Springer: Boston, MA, 2009.

(20) Zuo, J. M.; Spence, J. C., *Advanced Transmission Electron Microscopy: Imaging and Diffraction in Nanoscience*; Springer: New York, NY, 2017.

(21) Fultz, B.; Howe, J. M., *Transmission Electron Microscopy and Diffractometry of Materials*, 4 **edition**; Graduate Texts in Physics; Springer-Verlag: 2013.

(22) Egerton, R., *Electron Energy-Loss Spectroscopy in the Electron Microscope*; Springer: Boston, MA, 2011.

(23) Davisson, C. J.; Germer, L. H. *Proc Natl Acad Sci U S A* **1928**, *14*, 317–22.

(24) Korir, D. K.; Gwalani, B.; Joseph, A.; Kamras, B.; Arvapally, R. K.; Omary, M. A.; Marpu, S. B. *Nanomaterials (Basel)* **2019**, *9*, DOI: 10.3390/nano9040596.

(25) Janecek, M.; Kral, R., *Modern Electron Microscopy in Physical and Life Sciences*; IntechOpen: 2016.

(26) Egerton, R. F.; Li, P.; Malac, M. *Micron* **2004**, *35*, 399–409.

(27) Cailleau, H.; Luty, T.; Koshihara, S.; Servol, M.; Lorenc, M.; Buron-Le Cointe, M.; Collet, E. *Acta Physica Polonica A* **2012**, *121*, 297–306.

(28) Wegkamp, D.; Stähler, J. *Progress in Surface Science* **2015**, *90*, 464–502.

(29) Yonemitsu, K.; Nasu, K. *Physics Reports* **2008**, *465*, 1–60.

(30) Yonemitsu, K. *Crystals* **2012**, *2*, 56–77.

(31) Ishihara, S. *Journal of the Physical Society of Japan* **2019**, *88*, 072001.

(32) Mariette, C.; Lorenc, M.; Cailleau, H.; Collet, E.; Guerin, L.; Volte, A.; Trzop, E.; Bertoni, R.; Dong, X.; Lepine, B.; Hernandez, O.; Janod, E.; Cario, L.; Ta Phuoc, V.; Ohkoshi, S.; Tokoro, H.; Patthey, L.; Babic, A.; Usov, I.; Ozerov, D.; Sala, L.; Ebner, S.; Bohler, P.; Keller, A.; Oggenfuss, A.; Zmofing, T.; Redford, S.; Vetter, S.; Follath, R.; Juranic, P.; Schreiber, A.; Beaud, P.; Esposito, V.; Deng, Y.; Ingold, G.; Chergui, M.; Mancini, G. F.; Mankowsky, R.; Svetina, C.; Zerdane, S.; Mozzanica, A.; Bosak, A.; Wulff, M.; Levantino, M.; Lemke, H.; Cammarata, M. *Nat Commun* **2021**, *12*, 1239.

(33) Gros, C. R.; Peprah, M. K.; Felts, A. C.; Brinzari, T. V.; Risset, O. N.; Cain, J. M.; Ferreira, C. F.; Meisel, M. W.; Talham, D. R. *Dalton Trans* **2016**, *45*, 16624–16634.

(34) Azzolina, G.; Tokoro, H.; Imoto, K.; Yoshikiyo, M.; Ohkoshi, S. I.; Collet, E. *Angew Chem Int Ed Engl* **2021**, DOI: 10.1002/anie.202106959.

(35) Barlow, K.; Johansson, J. O. *Phys Chem Chem Phys* **2021**, *23*, 8118–8131.

(36) Zimara, J.; Stevens, H.; Oswald, R.; Demeshko, S.; Dechert, S.; Mata, R. A.; Meyer, F.; Schwarzer, D. *Inorg Chem* **2021**, *60*, 449–459.

(37) Londo, S.; Biswas, S.; Husek, J.; Pinchuk, I. V.; Newburger, M. J.; Boyadzhiev, A.; Trout, A. H.; McComb, D. W.; Kawakami, R.; Baker, L. R. *The Journal of Physical Chemistry C* **2020**, *124*, 11368–11375.

(38) Bostanjoglo, O.; Liedtke, R. *Physica Status Solidi (a)* **1980**, *60*, 451–455.

(39) Bostanjoglo, O.; Hoffmann, G. *physica status solidi (a)* **1982**, *73*, 95–105.

(40) Bostanjoglo, O.; Heinricht, F. *Scanning* **1986**, *8*, 146–148.

(41) Bostanjoglo, O.; Heinricht, F. *Journal of Physics E: Scientific Instruments* **1987**, *20*, 1491–1493.

(42) Bostanjoglo, O.; Tornow, R. P.; Tornow, W. *Ultramicroscopy* **1987**, *21*, 367–372.

(43) Bostanjoglo, O.; Heinricht, F. *Review of Scientific Instruments* **1990**, *61*, 1223–1229.

(44) Bostanjoglo, O.; Rosin, T. *Optica Acta: International Journal of Optics* **1977**, *24*, 657–664.

(45) LaGrange, T.; Campbell, G. H.; Reed, B. W.; Taheri, M.; Pesavento, J. B.; Kim, J. S.; Browning, N. D. *Ultramicroscopy* **2008**, *108*, 1441–9.

(46) LaGrange, T.; Reed, B. W.; Masiel, D. J. *MRS Bulletin* **2015**, *40*, 22–28.

(47) Lagrange, T.; Campbell, G.; Turchi, P.; King, W. *Acta Materialia* **2007**, *55*, 5211–5224.

(48) Kim, J. S.; Lagrange, T.; Reed, B. W.; Taheri, M. L.; Armstrong, M. R.; King, W. E.; Browning, N. D.; Campbell, G. H. *Science* **2008**, *321*, 1472–5.

(49) LaGrange, T.; Reed, B. W.; Santala, M. K.; McKeown, J. T.; Kulovits, A.; Wiezorek, J. M.; Nikolova, L.; Rosei, F.; Siwick, B. J.; Campbell, G. H. *Micron* **2012**, *43*, 1108–20.

(50) LaGrange, T.; Armstrong, M. R.; Boyden, K.; Brown, C. G.; Campbell, G. H.; Colvin, J. D.; DeHope, W. J.; Frank, A. M.; Gibson, D. J.; Hartemann, F. V.; Kim, J. S.; King, W. E.; Pyke, B. J.; Reed, B. W.; Shirk, M. D.; Shuttlesworth, R. M.; Stuart, B. C.; Torralva, B. R.; Browning, N. D. *Applied Physics Letters* **2006**, *89*, 044105.

(51) Masiel, D. J.; Reed, B. W.; Lagrange, T. B.; Campbell, G. H.; Guo, T.; Browning, N. D. *Chemphyschem* **2010**, *11*, 2088–90.

(52) Lobastov, V. A.; Srinivasan, R.; Zewail, A. H. *Proc Natl Acad Sci U S A* **2005**, *102*, 7069–73.

(53) Baskin, J. S.; Zewail, A. H. *Journal of Chemical Education* **2001**, *78*, 737.

(54) Barwick, B.; Flannigan, D. J.; Zewail, A. H. *Nature* **2009**, *462*, 902–6.

(55) Grinolds, M. S.; Lobastov, V. A.; Weissenrieder, J.; Zewail, A. H. *Proc Natl Acad Sci U S A* **2006**, *103*, 18427–31.

(56) Park, H. S.; Baskin, J. S.; Kwon, O. H.; Zewail, A. H. *Nano Lett* **2007**, *7*, 2545–51.

(57) Carbone, F.; Barwick, B.; Kwon, O.-H.; Park, H. S.; Spencer Baskin, J.; Zewail, A. H. *Chemical Physics Letters* **2009**, *468*, 107–111.

(58) Carbone, F.; Kwon, O. H.; Zewail, A. H. *Science* **2009**, *325*, 181–4.

(59) Yurtsever, A.; Zewail, A. H. *Science* **2009**, *326*, 708–12.

(60) Park, H. S.; Baskin, J. S.; Zewail, A. H. *Nano Lett* **2010**, *10*, 3796–803.

(61) Van der Veen, R. M.; Penfold, T. J.; Zewail, A. H. *Struct Dyn* **2015**, *2*, 024302.

(62) Barwick, B.; Zewail, A. H. *ACS Photonics* **2015**, *2*, 1391–1402.

(63) Yurtsever, A.; Schaefer, S.; Zewail, A. H. *Nano Lett* **2012**, *12*, 3772–7.

(64) Van der Veen, R. M.; Kwon, O. H.; Tissot, A.; Hauser, A.; Zewail, A. H. *Nat Chem* **2013**, *5*, 395–402.

(65) Plemmons, D. A.; Tae Park, S.; Zewail, A. H.; Flannigan, D. J. *Ultramicroscopy* **2014**, *146*, 97–102.

(66) Picher, M.; Bucker, K.; LaGrange, T.; Banhart, F. *Ultramicroscopy* **2018**, *188*, 41–47.

(67) Zewail, A. H. *Annu Rev Phys Chem* **2006**, *57*, 65–103.

(68) Lee, Y. M.; Kim, Y. J.; Kim, Y. J.; Kwon, O. H. *Struct Dyn* **2017**, *4*, 044023.

(69) Storeck, G.; Vogelgesang, S.; Sivis, M.; Schafer, S.; Ropers, C. *Struct Dyn* **2017**, *4*, 044024.

(70) Wilson, N. R.; Pandey, P. A.; Beanland, R.; Young, R. J.; Kinloch, I. A.; Gong, L.; Liu, Z.; Suenaga, K.; Rourke, J. P.; York, S. J.; Sloan, J. *ACS Nano* **2009**, *3*, 2547–56.

(71) Robertson, A. W.; Montanari, B.; He, K.; Allen, C. S.; Wu, Y. A.; Harrison, N. M.; Kirkland, A. I.; Warner, J. H. *ACS Nano* **2013**, *7*, 4495–502.

(72) Robertson, A. W.; Montanari, B.; He, K.; Kim, J.; Allen, C. S.; Wu, Y. A.; Olivier, J.; Neethling, J.; Harrison, N.; Kirkland, A. I.; Warner, J. H. *Nano Lett* **2013**, *13*, 1468–75.

(73) He, Z.; He, K.; Robertson, A. W.; Kirkland, A. I.; Kim, D.; Ihm, J.; Yoon, E.; Lee, G. D.; Warner, J. H. *Nano Lett* **2014**, *14*, 3766–72.

(74) Bae, C.; Lee, J.; Yao, L.; Park, S.; Lee, Y.; Lee, J.; Chen, Q.; Kim, J. *Nano Research* **2020**, *14*, 66–73.

(75) Liu, C.; Ou, Z.; Guo, F.; Luo, B.; Chen, W.; Qi, L.; Chen, Q. *J Am Chem Soc* **2020**, *142*, 11669–11673.

(76) Kim, A.; Zhou, S.; Yao, L.; Ni, S.; Luo, B.; Sing, C. E.; Chen, Q. *J Am Chem Soc* **2019**, *141*, 11796–11800.

(77) Ou, Z.; Yao, L.; An, H.; Shen, B.; Chen, Q. *Nat Commun* **2020**, *11*, 4555.

(78) Cornelius, R. D. Dynamic environmental transmission electron microscopy of spin crossover materials, Thesis, 2020.

(79) Ji, S.; Piazza, L.; Cao, G.; Park, S. T.; Reed, B. W.; Masiel, D. J.; Weissenrieder, J. *Struct Dyn* **2017**, *4*, 054303.

(80) Plemmons, D. A.; Flannigan, D. J. *Chemical Physics Letters* **2017**, *683*, 186–192.

(81) Gage, T.; Liu, H.; Arslan, I.; Schaller, R. D. *Microscopy and Microanalysis* **2020**, *26*, 434–436.

(82) Barwick, B.; Flannigan, D. J.; Zewail, A. H. *Nature* **2009**, *462*, 902–6.

(83) Park, S. T.; Lin, M.; Zewail, A. H. *New Journal of Physics* **2010**, *12*, 123028.

(84) Park, S. T.; Zewail, A. H. *J Phys Chem A* **2012**, *116*, 11128–33.

(85) Plemmons, D. A.; Tae Park, S.; Zewail, A. H.; Flannigan, D. J. *Ultramicroscopy* **2014**, *146*, 97–102.

(86) Yurtsever, A.; Zewail, A. H. *Science* **2009**, *326*, 708–12.

(87) Feist, A.; Rubiano da Silva, N.; Liang, W.; Ropers, C.; Schafer, S. *Struct Dyn* **2018**, *5*, 014302.

(88) Yurtsever, A.; Zewail, A. H. *Proceedings of the National Academy of Sciences* **2011**, *108*, 3152–3156.

(89) Flannigan, D. J.; Cremons, D. R.; Valley, D. T. *Journal of Materials Research* **2016**, *32*, 239–247.

(90) Bucker, K.; Picher, M.; Cregut, O.; LaGrange, T.; Reed, B. W.; Park, S. T.; Masiel, D. J.; Banhart, F. *Ultramicroscopy* **2016**, *171*, 8–18.

(91) Picher, M.; Bucker, K.; LaGrange, T.; Banhart, F. *Ultramicroscopy* **2018**, *188*, 41–47.

(92) Piazza, L.; Masiel, D. J.; LaGrange, T.; Reed, B. W.; Barwick, B.; Carbone, F. *Chemical Physics* **2013**, *423*, 79–84.

(93) Zandi, O.; Sykes, A. E.; Cornelius, R. D.; Alcorn, F. M.; Zerbe, B. S.; Duxbury, P. M.; Reed, B. W.; van der Veen, R. M. *Nat Commun* **2020**, *11*, 3001.

(94) Ando, T.; Fowler, A. B.; Stern, F. *Reviews of Modern Physics* **1982**, *54*, 437–672.

(95) Devreese, J. T.; Peeters, F. M., *The Physics of the Two-Dimensional Electron Gas*; Springer US: Boston, MA, 1987.

(96) Vaz, D. C.; Noel, P.; Johansson, A.; Gobel, B.; Bruno, F. Y.; Singh, G.; McKeown-Walker, S.; Trier, F.; Vicente-Arche, L. M.; Sander, A.; Valencia, S.; Bruneel, P.; Vivek, M.; Gabay, M.; Bergeal, N.; Baumberger, F.; Okuno, H.; Barthelemy, A.; Fert, A.; Vila, L.; Mertig, I.; Attane, J. P.; Bibes, M. *Nat Mater* **2019**, *18*, 1187–1193.

(97) Nifa, I.; Leroux, C.; Torres, A.; Charles, M.; Blachier, D.; Reimbold, G.; Ghibaudo, G.; Bano, E. *Microelectronic Engineering* **2017**, *178*, 128–131.

(98) Nifa, I.; Leroux, C.; Torres, A.; Charles, M.; Reimbold, G.; Ghibaudo, G.; Bano, E. *Microelectronic Engineering* **2019**, *215*, 110976.

(99) Ohtomo, A.; Hwang, H. Y. *Nature* **2004**, *427*, 423–6.

(100) Song, Q.; Zhang, H.; Su, T.; Yuan, W.; Chen, Y.; Xing, W.; Shi, J.; Sun, J.; Han, W. *Sci Adv* **2017**, *3*, e1602312.

(101) Zhang, C.; Sun, Z.; Lin, Y.; Guan, L.; Tao, J. *Phys Chem Chem Phys* **2020**, *22*, 11409–11416.

(102) Zhang, F.; Lv, P.; Zhang, Y.; Huang, S.; Wong, C. M.; Yau, H. M.; Chen, X.; Wen, Z.; Jiang, X.; Zeng, C.; Hong, J.; Dai, J. Y. *Phys Rev Lett* **2019**, *122*, 257601.

(103) Kumar, A.; Csathy, G. A.; Manfra, M. J.; Pfeiffer, L. N.; West, K. W. *Phys Rev Lett* **2010**, *105*, 246808.

(104) Jiang, Z.; Henriksen, E. A.; Tung, L. C.; Wang, Y. J.; Schwartz, M. E.; Han, M. Y.; Kim, P.; Stormer, H. L. *Phys Rev Lett* **2007**, *98*, 197403.

(105) Shingla, V.; Kleinbaum, E.; Kumar, A.; Pfeiffer, L. N.; West, K. W.; Csáthy, G. A. *Physical Review B* **2018**, *97*.

(106) Schreiber, K. A.; Csáthy, G. A. *Annual Review of Condensed Matter Physics* **2020**, *11*, 17–35.

(107) Zhang, Q.; Arikawa, T.; Kato, E.; Reno, J. L.; Pan, W.; Watson, J. D.; Manfra, M. J.; Zudov, M. A.; Tokman, M.; Erukhimova, M.; Belyanin, A.; Kono, J. *Phys Rev Lett* **2014**, *113*, 047601.

(108) Gospodarič, J.; Dziom, V.; Shuvaev, A.; Dobretsova, A. A.; Mikhailov, N. N.; Kvon, Z. D.; Pimenov, A. *Physical Review B* **2019**, *99*.

(109) Ma, J. C.; Deng, K.; Zheng, L.; Wu, S. F.; Liu, Z.; Zhou, S. Y.; Sun, D. *2d Materials* **2019**, *6*, 032001.

(110) Pandey, A.; Nikam, A. N.; Fernandes, G.; Kulkarni, S.; Padya, B. S.; Prassl, R.; Das, S.; Joseph, A.; Deshmukh, P. K.; Patil, P. O.; Mutalik, S. *Nanomaterials (Basel)* **2020**, *11*.

(111) He, J.; Liu, Y.; Funahashi, R. *Journal of Materials Research* **2011**, *26*, 1762–1772.

(112) Devoret, M. H.; Schoelkopf, R. J. *Science* **2013**, *339*, 1169–74.

(113) Casparis, L.; Connolly, M. R.; Kjaergaard, M.; Pearson, N. J.; Kringhoj, A.; Larsen, T. W.; Kuemmeth, F.; Wang, T.; Thomas, C.; Gronin, S.; Gardner, G. C.; Manfra, M. J.; Marcus, C. M.; Petersson, K. D. *Nat Nanotechnol* **2018**, *13*, 915–919.

(114) Moser, S.; Jovic, V.; Koch, R.; Moreschini, L.; Oh, J. S.; Jozwiak, C.; Bostwick, A.; Rotenberg, E. *Journal of Electron Spectroscopy and Related Phenomena* **2018**, *225*, 16–22.

(115) Liu, X.; Zhang, J.; Zhang, Z.; Lin, X.; Yu, Y.; Xing, X.; Jin, Z.; Cheng, Z.; Ma, G. *Applied Physics Letters* **2017**, *111*, 152906.

(116) Barnett, J.; Rose, M.-A.; Ulrich, G.; Lewin, M.; Kästner, B.; Hoehl, A.; Dittmann, R.; Gunkel, F.; Taubner, T. *Advanced Functional Materials* **2020**, *30*, 2004767.

(117) Pashnev, D.; Korotyeyev, V. V.; Jorudas, J.; Kaplas, T.; Janonis, V.; Urbanowicz, A.; Kašalynas, I. *Applied Physics Letters* **2020**, *117*, 162101.

(118) Zhukov, E. A.; Yakovlev, D. R.; Bayer, M.; Glazov, M. M.; Ivchenko, E. L.; Karczewski, G.; Wojtowicz, T.; Kossut, J. *Physical Review B* **2007**, *76*.

(119) Wang, X.; Hilton, D. J.; Reno, J. L.; Mittleman, D. M.; Kono, J. *Opt Express* **2010**, *18*, 12354–61.

(120) Kotthaus, J. P.; Abstreiter, G.; Koch, J. F.; Ranvaud, R. *Physical Review Letters* **1975**, *34*, 151–154.

(121) Schlesinger, Z.; Allen, S. J.; Hwang, J. C. M.; Platzman, P. M.; Tzoar, N. *Physical Review B* **1984**, *30*, 435–437.

(122) Maag, T.; Bayer, A.; Baierl, S.; Hohenleutner, M.; Korn, T.; Schüller, C.; Schuh, D.; Bougeard, D.; Lange, C.; Huber, R.; Mootz, M.; Sipe, J. E.; Koch, S. W.; Kira, M. *Nature Physics* **2015**, *12*, 119–123.

(123) Shockley, W. *Physical Review* **1953**, *90*, 491–491.

(124) Dresselhaus, G.; Kip, A. F.; Kittel, C. *Physical Review* **1955**, *98*, 368–384.

(125) Szyszka, A.; Wośko, M.; Paszkiewicz, B.; Paszkiewicz, R. *Materials Science in Semiconductor Processing* **2019**, *94*, 57–63.

(126) Cantoni, C.; Gazquez, J.; Miletto Granozio, F.; Oxley, M. P.; Varela, M.; Lupini, A. R.; Pennycook, S. J.; Aruta, C.; di Uccio, U. S.; Perna, P.; Maccariello, D. *Adv Mater* **2012**, *24*, 3952–7.

(127) Suzuki, D.; Oda, S.; Kawano, Y. *Applied Physics Letters* **2013**, *102*, 122102.

(128) Zhu, P. F.; Zhang, Z. C.; Chen, L.; Li, R. Z.; Li, J. J.; Wang, X.; Cao, J. M.; Sheng, Z. M.; Zhang, J. *Rev Sci Instrum* **2010**, *81*, 103505.

(129) White, A. J.; Ticknor, C.; Meyer, E. R.; Kress, J. D.; Collins, L. A. *Phys Rev E* **2019**, *100*, 033213.

(130) Kluge, T.; Rödel, M.; Metzkes-Ng, J.; Pelka, A.; Garcia, A. L.; Prencipe, I.; Rehwald, M.; Nakatsutsumi, M.; McBride, E. E.; Schönherr, T.; Garten, M.; Hartley, N. J.; Zacharias, M.; Grenzer, J.; Erbe, A.; Georgiev, Y. M.; Galtier, E.; Nam, I.; Lee, H. J.; Glenzer, S.; Bussmann, M.; Gutt, C.; Zeil, K.; Rödel, C.; Hübner, U.; Schramm, U.; Cowan, T. E. *Physical Review X* **2018**, *8*.

(131) Zhu, P. F.; Zhang, Z. C.; Chen, L.; Li, R. Z.; Li, J. J.; Wang, X.; Cao, J. M.; Sheng, Z. M.; Zhang, J. *Rev Sci Instrum* **2010**, *81*, 103505.

(132) Chen, L.; Li, R.; Chen, J.; Zhu, P.; Liu, F.; Cao, J.; Sheng, Z.; Zhang, J. *Proc Natl Acad Sci U S A* **2015**, *112*, 14479–83.

(133) Collins, L. A.; Bickham, S. R.; Kress, J. D.; Mazevet, S.; Lenosky, T. J.; Troullier, N. J.; Windl, W. *Physical Review B* **2001**, *63*.

(134) Diaw, A.; Barros, K.; Haack, J.; Junghans, C.; Keenan, B.; Li, Y. W.; Livescu, D.; Lubbers, N.; McKerns, M.; Pavel, R. S.; Rosenberger, D.; Sagert, I.; Germann, T. C. *Phys Rev E* **2020**, *102*, 023310.

(135) Starrett, C. E.; Shaffer, N. *Phys Rev E* **2020**, *102*, 043211.

(136) Collins, L.; Kwon, I. I.; Kress, J.; Troullier, N.; Lynch, D. *Phys Rev E Stat Phys Plasmas Fluids Relat Interdiscip Topics* **1995**, *52*, 6202–6219.

(137) Williams, J.; Zhou, F.; Sun, T.; Tao, Z.; Chang, K.; Makino, K.; Berz, M.; Duxbury, P. M.; Ruan, C. Y. *Struct Dyn* **2017**, *4*, 044035.

(138) Portman, J.; Zhang, H.; Makino, K.; Berz, M.; Duxbury, P. **in**.

(139) Pasmans, P. L. E. M.; van Vugt, D. C.; van Lieshout, J. P.; Brussaard, G. J. H.; Luiten, O. J. *Physical Review Accelerators and Beams* **2016**, *19*.

(140) Engelen, W. J.; van der Heijden, M. A.; Bakker, D. J.; Vredenbregt, E. J.; Luiten, O. J. *Nat Commun* **2013**, *4*, 1693.

(141) Andre, T.; Andriyash, I. A.; Loulergue, A.; Labat, M.; Roussel, E.; Ghaith, A.; Khojoyan, M.; Thaury, C.; Valleau, M.; Briquez, F.; Marteau, F.; Tavakoli, K.; N'Gotta, P.; Dietrich, Y.; Lambert, G.; Malka, V.; Benabderrahmane, C.; Veteran, J.; Chapuis, L.; El Ajjouri, T.; Sebdaoui, M.; Hubert, N.; Marcouille, O.; Berteaud, P.; Leclercq, N.; El Ajjouri, M.; Rommeluere, P.; Bouvet, F.; Duval, J.; Kitegi, C.; Blache, F.; Mahieu, B.; Corde, S.; Gautier, J.; Ta Phuoc, K.; Goddet, J. P.; Lestrade, A.; Herbeaux, C.; Evain, C.; Szwaj, C.; Bielawski, S.; Tafzi, A.; Rousseau, P.; Smartsev, S.; Polack, F.; Dennetiere, D.; Bourassin-Bouchet, C.; De Oliveira, C.; Couprie, M. E. *Nat Commun* **2018**, *9*, 1334.

(142) Lorusso, A.; Perrone, A.; Gontad, F. *Nuclear Instruments and Methods in Physics Research Section A: Accelerators, Spectrometers, Detectors and Associated Equipment* **2019**, *942*, 162429.

(143) Bandurkin, I. V.; Oparina, Y. S.; Osharin, I. V.; Savilov, A. V. *Physics of Plasmas* **2019**, *26*, 113105.

(144) Musumeci, P.; Moody, J. T.; England, R. J.; Rosenzweig, J. B.; Tran, T. *Phys Rev Lett* **2008**, *100*, 244801.

(145) Musumeci, P.; Cultrera, L.; Ferrario, M.; Filippetto, D.; Gatti, G.; Gutierrez, M. S.; Moody, J. T.; Moore, N.; Rosenzweig, J. B.; Scoby, C. M.; Travish, G.; Vicario, C. *Phys Rev Lett* **2010**, *104*, 084801.

(146) Carbone, F.; Musumeci, P.; Luiten, O. J.; Hebert, C. *Chemical Physics* **2012**, *392*, 1–9.

(147) Zerbe, B. S.; Xiang, X.; Ruan, C. Y.; Lund, S. M.; Duxbury, P. M. *Physical Review Accelerators and Beams* **2018**, *21*.

(148) Zuo, J. M.; Spence, J. C. H., *Advanced transmission electron microscopy : imaging and diffraction in nanoscience*; Springer: New York, NY, 2017.

(149) Williams, D. B.; Carter, C. B., *Transmission electron microscopy : a textbook for materials science*, 2nd ed.; Springer: New York, 2009.

(150) Portman, J.; Zhang, H.; Makino, K.; Ruan, C. Y.; Berz, M.; Duxbury, P. M. *Journal of Applied Physics* **2014**, *116*, 174302.

(151) Luiten, O. J.; van der Geer, S. B.; de Loos, M. J.; Kiewiet, F. B.; van der Wiel, M. J. *Phys Rev Lett* **2004**, *93*, 094802.

(152) Kovalev, V. F.; Popov, K. I.; Bychenkov, V. Y.; Rozmus, W. *Physics of Plasmas* **2007**, *14*, 053103.

(153) Grech, M.; Nuter, R.; Mikaberidze, A.; Di Cintio, P.; Gremillet, L.; Lefebvre, E.; Saalmann, U.; Rost, J. M.; Skupin, S. *Phys Rev E Stat Nonlin Soft Matter Phys* **2011**, *84*, 056404.

(154) Singh, B.; Indra, A. *Materials Today Energy* **2020**, *16*, 100404.

(155) Qiu, S.; Xu, Y.; Wu, X.; Ji, X. *Electrochemical Energy Reviews* **2021**.

(156) Zhou, N.; Yang, L.; Hu, B.; Song, Y.; He, L.; Chen, W.; Zhang, Z.; Liu, Z.; Lu, S. *Anal Chem* **2018**, *90*, 13624–13631.

(157) Huang, Y.; Ren, S. *Applied Materials Today* **2021**, *22*, 100886.

(158) Felts, A. C.; Slimani, A.; Cain, J. M.; Andrus, M. J.; Ahir, A. R.; Abboud, K. A.; Meisel, M. W.; Boukheddaden, K.; Talham, D. R. *Journal of the American Chemical Society* **2018**, *140*, 5814–5824.

(159) Felts, A. C.; Andrus, M. J.; Knowles, E. S.; Quintero, P. A.; Ahir, A. R.; Risset, O. N.; Li, C. H.; Maurin, I.; Halder, G. J.; Abboud, K. A.; Meisel, M. W.; Talham, D. R. *The Journal of Physical Chemistry C* **2016**, *120*, 5420–5429.

(160) Cain, J. M.; Felts, A. C.; Meisel, M. W.; Talham, D. R. *Chemistry of Materials* **2020**, *33*, 246–255.

(161) Cain, J. M.; He, W.; Maurin, I.; Meisel, M. W.; Talham, D. R. *Journal of Applied Physics* **2021**, *129*, 160903.

(162) Escax, V.; Bleuzen, A.; Cartier Dit Moulin, C.; Villiam, F.; Goujon, A.; Varret, F.; Verdaguer, M. *J Am Chem Soc* **2001**, *123*, 12536–43.

(163) Jafri, S. F.; Arrio, M. A.; Bordage, A.; Moulin, R.; Juhin, A.; Cartier Dit Moulin, C.; Otero, E.; Ohresser, P.; Bleuzen, A.; Sainctavit, P. *Inorg Chem* **2018**, *57*, 7610–7619.

(164) Bleuzen, A.; Escax, V.; Ferrier, A.; Villain, F.; Verdaguer, M.; Münsch, P.; Itié, J.-P. *Angewandte Chemie* **2004**, *116*, 3814–3817.

(165) Escax, V.; Champion, G.; Arrio, M. A.; Zacchigna, M.; Cartier Dit Moulin, C.; Bleuzen, A. *Angew Chem Int Ed Engl* **2005**, *44*, 4798–801.

(166) Itoi, M.; Jike, T.; Nishio-Hamane, D.; Udagawa, S.; Tsuda, T.; Kuwabata, S.; Boukheddaden, K.; Andrus, M. J.; Talham, D. R. *Journal of the American Chemical Society* **2015**, *137*, 14686–93.

(167) Shimamoto, N.; Ohkoshi, S.; Sato, O.; Hashimoto, K. *Inorg Chem* **2002**, *41*, 678–84.

(168) Park, J. H.; Frye, F.; Anderson, N. E.; Pajerowski, D. M.; Huh, Y. D.; Talham, D. R.; Meisel, M. W. *Journal of Magnetism and Magnetic Materials* **2007**, *310*, 1458–1459.

(169) Cammarata, M.; Zerdane, S.; Balducci, L.; Azzolina, G.; Mazerat, S.; Exertier, C.; Trabuco, M.; Levantino, M.; Alonso-Mori, R.; Glownia, J. M.; Song, S.; Catala, L.; Mallah, T.; Matar, S. F.; Collet, E. *Nat Chem* **2021**, *13*, 10–14.

(170) He, W.; Cain, J. M.; Meisel, M. W.; Talham, D. R. *Journal of Materials Chemistry C* **2021**, *9*, 10830–10840.

(171) Gros, C. R.; Peprah, M. K.; Hosterman, B. D.; Brinzari, T. V.; Quintero, P. A.; Sendova, M.; Meisel, M. W.; Talham, D. R. *J Am Chem Soc* **2014**, *136*, 9846–9.

(172) Sugar, J. D.; Cummings, A. W.; Jacobs, B. W.; Robinson, D. B. *Microscopy Today* **2014**, *22*, 40–47.

(173) Tong, X.; Ye, Z.; Xu, Y.; Gao, S.; Xie, H.; Du, Q.; Liu, S.; Xu, X.; Liu, S.; Luan, K.; Stilla, U. *IEEE Journal of Selected Topics in Applied Earth Observations and Remote Sensing* **2019**, *12*, 4062–4081.

(174) Egerton, R. F. *Ultramicroscopy* **2013**, *127*, 100–8.

(175) Leijten, Z.; Keizer, A. D. A.; de With, G.; Friedrich, H. *The Journal of Physical Chemistry C* **2017**, *121*, 10552–10561.

(176) Isaacson, M. *Ultramicroscopy* **1979**, *4*, 193–199.

(177) Egerton, R. F.; Lazar, S.; Libera, M. *Micron* **2012**, *43*, 2–7.

(178) Egerton, R. F. *Microsc Res Tech* **2012**, *75*, 1550–6.

(179) Adak, S.; Daemen, L. L.; Hartl, M.; Williams, D.; Summerhill, J.; Nakotte, H. *Journal of Solid State Chemistry* **2011**, *184*, 2854–2861.

(180) Matsuda, T.; Kim, J. E.; Ohoyama, K.; Moritomo, Y. *Physical Review B* **2009**, *79*.

(181) Miyashita, S.; Konishi, Y.; Nishino, M.; Tokoro, H.; Rikvold, P. A. *Physical Review B* **2008**, *77*.

(182) Enachescu, C.; Stoleriu, L.; Stancu, A.; Hauser, A. *Phys Rev Lett* **2009**, *102*, 257204.

(183) Oubouchou, H.; Slimani, A.; Boukheddaden, K. *Physical Review B* **2013**, *87*.

(184) Slimani, A.; Boukheddaden, K.; Varret, F.; Oubouchou, H.; Nishino, M.; Miyashita, S. *Physical Review B* **2013**, *87*.

(185) Ndiaye, M.; Singh, Y.; Fourati, H.; Sy, M.; Lo, B.; Boukheddaden, K. *Journal of Applied Physics* **2021**, *129*, 153901.

(186) Oubouchou, H.; Singh, Y.; Boukheddaden, K. *Physical Review B* **2018**, *98*.

(187) Wang, X.; Zhong, X.; Cheng, L. *Coordination Chemistry Reviews* **2021**, *430*, 213662.

(188) Lagopati, N.; Evangelou, K.; Falaras, P.; Tsilibary, E. C.; Vasileiou, P. V. S.; Havaki, S.; Angelopoulou, A.; Pavlatou, E. A.; Gorgoulis, V. G. *Pharmacol Ther* **2021**, *222*, 107795.

(189) Paumo, H. K.; Dalhatou, S.; Katata-Seru, L. M.; Kamdem, B. P.; Tijani, J. O.; Vishwanathan, V.; Kane, A.; Bahadur, I. *Journal of Molecular Liquids* **2021**, *331*, 115458.

(190) Nunes Simonetti, E. A.; Cardoso de Oliveira, T.; Enrico do Carmo Machado, Á.; Coutinho Silva, A. A.; Silva dos Santos, A.; de Simone Cividanes, L. *Ceramics International* **2021**, 17844–17876.

(191) Medina-Reyes, E. I.; Rodriguez-Ibarra, C.; Deciga-Alcaraz, A.; Diaz-Urbina, D.; Chirino, Y. I.; Pedraza-Chaverri, J. *Food Chem Toxicol* **2020**, *146*, 111814.

(192) Govardhana Reddy, P. V.; Rajendra Prasad Reddy, B.; Venkata Krishna Reddy, M.; Raghava Reddy, K.; Shetti, N. P.; Saleh, T. A.; Aminabhavi, T. M. *J Environ Manage* **2021**, *279*, 111603.

(193) Ahamed, A.; Liang, L.; Lee, M. Y.; Bobacka, J.; Lisak, G. *J Hazard Mater* **2021**, *404*, 124107.

(194) Baranowska-Wojcik, E. *Biol Trace Elem Res* **2021**, DOI: 10.1007/s12011-021-02578-5.

(195) Yang, K.; Dai, Y.; Huang, B. *Catalysts* **2020**, *10*, 972.

(196) Liu, C.; Wang, Y. *Chemistry* **2021**, *27*, 4270–4282.

(197) Illarionov, G. A.; Morozova, S. M.; Chrishtop, V. V.; Einarsrud, M. A.; Morozov, M. I. *Front Chem* **2020**, *8*, 724.

(198) Li, K.; Teng, C.; Wang, S.; Min, Q. *Front Chem* **2021**, *9*, 637501.

(199) Spirescu, V. A.; Chircov, C.; Grumezescu, A. M.; Vasile, B. S.; Andronescu, E. *Int J Mol Sci* **2021**, *22*.

(200) Kaur, N.; Singh, M.; Moumen, A.; Duina, G.; Comini, E. *Materials (Basel)* **2020**, *13*.

(201) Goncalves, R. A.; Toledo, R. P.; Joshi, N.; Berengue, O. M. *Molecules* **2021**, *26*.

(202) Lubojanski, A.; Dobrzynski, M.; Nowak, N.; Rewak-Soroczynska, J.; Sztyler, K.; Zakrzewski, W.; Dobrzynski, W.; Szymonowicz, M.; Rybak, Z.; Wiglusz, K.; Wiglusz, R. J. *Nanomaterials (Basel)* **2021**, *11*.

(203) Campos, D. A.; Schaumann, G. E.; Philippe, A. *Crit Rev Anal Chem* **2020**, 1–21.

(204) Gobi, R.; Ravichandiran, P.; Babu, R. S.; Yoo, D. J. *Polymers (Basel)* **2021**, *13*.

(205) Kayani, A. B. A.; Kuriakose, S.; Monshipouri, M.; Khalid, F. A.; Walia, S.; Sriram, S.; Bhaskaran, M. *Small* **2021**, e2100621.

(206) Su, Z.; Liu, J.; Li, M.; Zhu, Y.; Qian, S.; Weng, M.; Zheng, J.; Zhong, Y.; Pan, F.; Zhang, S. *Electrochemical Energy Reviews* **2020**, *3*, 286–343.

(207) Zhang, M.-M.; Chen, J.-Y.; Li, H.; Wang, C.-R. *Rare Metals* **2020**, *40*, 249–271.

(208) Andersson, S.; Collén, B.; Kuylenstierna, U.; Magnéli, A.; Magnéli, A.; Pestmalis, H.; Åsbrink, S. *Acta Chemica Scandinavica* **1957**, *11*, 1641–1652.

(209) Åsbrink, S.; Magnéli, A. *Acta Crystallographica* **1959**, *12*, 575–581.

(210) Iwasaki, H.; Bright, N. F. H.; Rowland, J. F. *Journal of the Less Common Metals* **1969**, *17*, 99–110.

(211) Rao, C. N. R.; Ramdas, S.; Loehman, R. E.; Honig, J. M. *Journal of Solid State Chemistry* **1971**, *3*, 83–88.

(212) Keys, L. K.; Mulay, L. N. *Applied Physics Letters* **1966**, *9*, 248–250.

(213) Watanabe, M.; Ueno, W.; Hayashi, T. *Journal of Luminescence* **2007**, *122-123*, 393–395.

(214) Nie, X.-C.; Song, H.-Y.; Zhang, X.; Liu, S.-B.; Li, F.; Yue, L.; Meng, J.-Q.; Duan, Y.-X.; Zhao, L.; Liu, H.-Y. *Applied Physics Express* **2018**, *11*, 095802.

(215) Yoshimatsu, K.; Sakata, O.; Ohtomo, A. *Sci Rep* **2017**, *7*, 12544.

(216) Tanaka, K.; Nasu, T.; Miyamoto, Y.; Ozaki, N.; Tanaka, S.; Nagata, T.; Hakoe, F.; Yoshikiyo, M.; Nakagawa, K.; Umeta, Y.; Imoto, K.; Tokoro, H.; Namai, A.; Ohkoshi, S.-i. *Crystal Growth and Design* **2014**, *15*, 653–657.

(217) Hong, S. H.; Åsbrink, S. *Acta Crystallographica Section B Structural Crystallography and Crystal Chemistry* **1982**, *38*, 2570–2576.

(218) Hong, S.-H.; Hesse, R.; Jennische, P.; Wahlberg, A.; Bastiansen, O.; Braathen, G.; Fernholt, L.; Gundersen, G.; Nielsen, C. J.; Cyvin, B. N.; Cyvin, S. J. *Acta Chemica Scandinavica* **1982**, *36a*, 207–217.

(219) Ohkoshi, S.; Tsunobuchi, Y.; Matsuda, T.; Hashimoto, K.; Namai, A.; Hakoe, F.; Tokoro, H. *Nat Chem* **2010**, *2*, 539–45.

(220) Makiura, R.; Takabayashi, Y.; Fitch, A. N.; Tokoro, H.; Ohkoshi, S.; Prassides, K. *Chem Asian J* **2011**, *6*, 1886–90.

(221) Tokoro, H.; Yoshikiyo, M.; Imoto, K.; Namai, A.; Nasu, T.; Nakagawa, K.; Ozaki, N.; Hakoe, F.; Tanaka, K.; Chiba, K.; Makiura, R.; Prassides, K.; Ohkoshi, S. *Nat Commun* **2015**, *6*, 7037.

(222) Asahara, A.; Watanabe, H.; Tokoro, H.; Ohkoshi, S.-i.; Suemoto, T. *Physical Review B* **2014**, *90*.

(223) Tasca, K. R.; Esposito, V.; Lantz, G.; Beaud, P.; Kubli, M.; Savoini, M.; Giles, C.; Johnson, S. L. *Chemphyschem* **2017**, *18*, 1385–1392.

(224) Ohkoshi, S. I.; Tokoro, H.; Nakagawa, K.; Yoshikiyo, M.; Jia, F.; Namai, A. *Sci Rep* **2019**, *9*, 13203.

(225) Schiffmann, A.; Knez, D.; Lackner, F.; Lasserus, M.; Messner, R.; Schnedlitz, M.; Kothleitner, G.; Hofer, F.; Ernst, W. E. *Journal of Applied Physics* **2019**, *125*, 023104.

(226) Wu, Y.; Zhang, Q.; Wu, X.; Qin, S.; Liu, J. *Journal of Solid State Chemistry* **2012**, *192*, 356–359.

(227) Liu, L.; Feng, Y. P.; Shen, Z. X. *Physical Review B* **2003**, *68*.